Skolkovo Institute of Science and Technology

ADDITIVES FOR IMPROVING THE INTRINSIC STABILITY OF HYBRID PEROVSKITE SOLAR CELLS

Doctoral Thesis

BY

MAYURIBALA MANGRULKAR

DOCTORAL PROGRAM IN MATERIALS SCIENCE AND ENGINEERING

Supervisor

Prof. Keith J. Stevenson

Moscow – 2021

I hereby declare that the work presented in this thesis was carried out by myself at Skolkovo Institute of Science and Technology, Moscow, except where due acknowledgement is made and has not been submitted for any other degree.

Candidate- Mayuribala Mangrulkar

Supervisor – Prof. Keith J. Stevenson

Abstract

Hybrid lead halide-based perovskite solar cells have caught the attention of the scientific community all across the globe. This is because research associated with perovskite solar cells showed a dramatic improvement in efficiency compared to conventional solar cells built with Silicon. Additionally, benefits such as solution processing and ease of manufacturing make it a potential candidate to replace conventional photovoltaics materials. However, poor stability issues have been a significant drawback. The poor stability of the perovskite layer often disintegrates perovskite into either PbI_2, metallic lead, or some volatile species, creating defects at the surface, grain boundaries and causing permanent damage to the perovskite structure. Hence, this work aims to investigate additives for improving the stability of hybrid organic-inorganic perovskite solar cells based on methylammonium lead iodide-based active layer. Thus, this thesis is dedicated to investigating additives that can improve the intrinsic photostability of $MAPbI_3$. To achieve the aim, additives were mixed into the perovskite precursor, first screened by a thin-film photostability test, and then investigated in the complete solar cell devices to further examine their operational stability under illumination. For this thesis, three of the best additives showing stabilization effects were studied in detail. Their mechanism of improving stability and influence on morphology, optoelectronics property were examined in conjunction with the operational stability of additive-containing solar cells. The highest operational stability of solar cells achieved in this work was 4400 h (which is ~80% of the initial stage) due to N_2H_5I (hydrazinium iodide/HAI) incorporation in $MAPbI_3$ film, followed by 1500 h (which is more than 95% of the initial stage) due to N-Methyl-2-pyrrolidone (NMP) cosolvent present with excess PbI_2 (lead iodide) in $MAPbI_3$.

Thesis related publication

1. **Mayuribala Mangrulkar**, Aleksandra G. Boldyreva, Svetlana A. Lipovskikh, Pavel A.Troshin, Keith J. Stevenson. "Influence of hydrazinium iodide on the intrinsic photostability of $MAPbI_3$ thin films and solar cells". Journal of Materials Research, 2021, doi.org/10.1557/s43578-021-00158-w

2. **Mayuribala Mangrulkar**, Sergey Yu. Luchkin, Aleksandra G. Boldyreva, Pavel A. Troshin and Keith J. Stevenson. "Influence of pyridine-based ligands on photostability of $MAPbI_3$ thin films". Mendeleev Communications, 2021, 31, 3, 319-322. doi.org/10.1016/j.mencom.2021.04.013

3. **Mayuribala Mangrulkar**, Sergey Luchkin, Azat Akbulatov, Ivan Zhukov, Ernst Kurmaev, Pavel A. Troshin and Keith J Stevenson. "Rationalizing the effect of overstoichiometric PbI_2 on the stability of perovskite solar cells in the context of precursor solution formulation". Synthetic Metals, 2021, 278, 116823. doi.org/10.1016/j.synthmet.2021.116823

4. **Mayuribala Mangrulkar** and Keith J. Stevenson. "The progress of additive engineering for $CH_3NH_3PbI_3$ photo-active layer in the context of perovskite solar cells". Crystals, 2021, 11, 814. https://doi.org/10.3390/cryst11070814

Author's Contribution

Publication 1. "Influence of hydrazinium iodide on the intrinsic photostability of $MAPbI_3$ thin films and solar cells". The author is mainly responsible for this work. The author prepared samples, executed experiments (UV-Vis, XRD, FTIR, Device performance, and device aging tests). Further, the author finalized the results and wrote the manuscript.

Publication 2. "Influence of pyridine-based ligands on photostability of $MAPbI_3$ thin films". The author is mainly responsible for this work. The author prepared samples, executed experiments (UV-Vis, XRD, FTIR, Device performance-related measurements). Further, the author finalized the results and wrote the manuscript.

Publication 3. "Rationalizing the effect of overstoichiometric PbI_2 on the stability of perovskite solar cells in the context of precursor solution formulation". The author is mainly responsible for this work. The author prepared samples, executed experiments (UV-Vis, XRD, Device performance, and device stability measurements). Further, the author finalized the results and wrote the manuscript.

Publication 4. "The progress of additive engineering for $CH_3NH_3PbI_3$ photo-active layer in the context of perovskite solar cells". The author is mainly responsible for this work. The author performed and analysed the literature review. Further, the author wrote the manuscript.

Other Publications

1. Olga R. Yamilova, Andrei V. Danilov, **Mayuribala Mangrulkar**, Yuri S. Fedotov, Sergey Yu. Luchkin, Sergey D. Babenko, Sergey I. Bredikhin, Sergey M. Aldoshin, Keith J.Stevenson, and Pavel A. Troshin. "Reduction of methylammonium cations as a major electrochemical degradation pathway in $MAPbI_3$ perovskite solar cells". J. Phys. Chem. Lett. 2020, 11, 1, 221–228. doi.org/10.1021/acs.jpclett.9b03161

2. **Mayuribala Mangrulkar**, Aleksandra G. Boldyreva, Sergey Yu. Luchkin, Pavel A.Troshin and Keith J. Stevenson. Influence of acid additives on the intrinsic photostability of $MAPbI_3$ thin film. (Submitted)

Conferences

1. **Mayuribala Mangrulkar**, Pavel A Troshin and Keith J Stevenson. "Impact of PbI_2 additive on the performance and stability of methylammonium lead iodide in thin films and solar cells". 3rd Annual MIT-Skoltech Conference – "Collaborative Solutions for Next Generation Education, Science and Technology", Skolkovo Institute of Science and Technology, Moscow, Russia, 2018, Oct 15-16. (Poster session)
2. Tatiana Dubinina, Sergey Tsarev, Sergey Yu Luchkin, **Mayuribala Mangrulkar**, Ernst Z. Kurmaev, Keith J. Stevenson, Pavel A. Troshin. "Passivation of zinc oxide electron transport layer by [6,6] -phenyl-c61-butyric acid for highly efficient perovskite solar cells". 3rd Annual MIT-Skoltech Conference – "Collaborative Solutions for Next Generation Education, Science and Technology", Skolkovo Institute of Science and Technology, Moscow, Russia, 2018, Oct 15-16. (Poster session)
3. **Mayuribala Mangrulkar**, Pavel A. Troshin and Keith J. Stevenson. "Impact of over stoichiometric PbI_2 on photovoltaic performance and photostability of $MAPbI_3$ perovskite films". HOPE-PV 2019 1st "International School on Hybrid, Organic and Perovskite Photovoltaics", Moscow, Russia, 2019, Oct 21-23. (Poster session)
4. **Mayuribala Mangrulkar**, Pavel A. Troshin and Keith J. Stevenson. "Impact of over stoichiometric PbI_2 on photovoltaic performance and photostability of $MAPbI_3$ perovskite films". "Contemporary Stability Challenges in Hybrid Perovskite Photovoltaics", held online, 2020 Apr 16. (Poster session)
5. **Mayuribala Mangrulkar**, Pavel A. Troshin and Keith J. Stevenson. "Additive approach to enhance intrinsic photo & thermal controlled stability of $MAPbI_3$ thin films". 2nd "Moscow Autumn Perovskite Photovoltaic International Conference" (MAPPIC-2020), held online, 2020 Oct 26-28. (Poster session)

Acknowledgements

I am thankful to the Skolkovo Institute of Science and Technology for providing the research facilities required to conduct the experiments at the Centre of Energy Science and Technologies (CEST) and Advanced Imaging Core Facility (AICF), and our collaborators from the Institute for Problems of Chemical Physics of RAS (IPCP RAS), Chernogolovka, Moscow, Russia, Institute of Physics and Technology, Ural Federal University (UrFU), Yekaterinburg, Russia, M. N. Mikheev Institute of Metal Physics of Ural Branch of Russian Academy of Sciences (IMP UB RAS), Yekaterinburg, Russia.

I am blessed to have Prof. Keith J. Stevenson as my supervisor and would like to express special gratitude to Prof. Keith J. Stevenson for his supervision, support and guidance. Without Prof. Keith J. Stevenson's support, this dissertation would not have been possible. Further, I would like to thank Prof. Pavel A. Troshin for his support for the work done during this PhD project. I am thankful to Prof. Andriy Zhugayevich and Prof. Alexei Buchachenko for being on the doctoral committee and evaluating my progress.

In addition, I would like to express my thanks to all the labmates and colleagues for their assistance. Regular discussions with them helped me to frame and execute my research plans. Further, I would like to extend my thankfulness to Dr. Sergey Tsarev for training me to fabricate solar cells, Dr. Azat. F. Akbulatov to teach me how to use additives.

I want to acknowledge and express my gratitude towards colleagues who performed some of the presented experiments in this thesis. AFM imaging and in-situ photo-degradation measurements were carried out by Dr. Sergey Yu Luchkin (CEST, Skoltech). EDX measurements were done by Dr. Azat. F. Akbulatov (IPCP RAS). PL and Power dependent PL measurements were performed by Dr. Alexandra G. Boldyreva (CEST, Skoltech). SEM and EDX measurements were carried by Dr. Svetlana A. Lipovskikh (AICF, Skoltech).

XPS results were acquired by Prof. Ivan Zhidkov (UrFU) and Prof. Ernst Kurmaev (IMP UB RAS).

Finally, I would like to express my heartfelt appreciation to my friends and parents for their unwavering support throughout my life. Especially, my mother who supported me in pursuing my dreams of higher education and always motivated me to step forward in the direction of achievement. Without her backing, I would not have been able to reach this milestone in my life.

Table of Contents

List of Symbols, Abbreviations

Ag – Silver

Al – Aluminium

AM 1.5G – Air Mass 1.5 Global

a-Si – Amorphous Silicon

BHJ – Bulk Heterojunction

CdTe – Cadmium Telluride

CIGS - Copper Indium Gallium Selenide

CSSCs – Crystalline Silicon Solar Cells

c-Si – Crystalline Silicon

DMF – Dimethylformamide

DMSO – Dimethylsulfoxide

DSSCs – Dye-Sensitized Solar Cells

EDX – Energy-Dispersive X-ray

EQE – External Quantum Efficiency

ETL – Electron Transport Layer

ETM – Electron Transport Material

FA – Formamidinium

FAI – Formamidinium Iodide

FF – Fill Factor (%)

FWHM – Full Width at Half Maximum

GaAs – Gallium Arsenide

HOMO – Highest Occupied Molecular Orbital

HTL – Hole Transport Layer

HTM – Hole Transport Material

ITO – Indium Tin Oxide

J_{SC} – Short Circuit Current Density

LBIC – Light beam induced current

LiTFSI - Lithium bis(trifluoromethylsulfonyl)imide

MA – Methylammonium

MAI – Methylammonium Iodide

$MAPbI_3$ - Methylammonium Lead Iodide

MoO_x – Molybdenum oxide

N_2 - Nitrogen

NiO_x – Nickel Oxide

NMP- N-Methyl-2-pyrrolidone

NREL – National Renewable Energy Laboratory

PbI_2 – Lead Iodide

PCBA - Phenyl-C61-butyric acid

$PC_{61}BM$ - Phenyl-C61-butyric acid methyl ester

$PC_{71}BM$ - Phenyl-C71-butyric acid methyl ester

PCE – Power Conversion Efficiency

PEDOT:PSS – Poly(3,4-ethylenedioxythiophene) polystyrene sulfonate

PL – Photoluminescence

PSCs – Perovskite Solar Cells

p-Si - Polycrystalline Silicon

PTAA – Poly[bis(4-phenyl)(2,4,6-trimethylphenyl)amine]

PTA - Poly[bis(4-phenyl)(4 -trimethylphenyl)amine]

PV – Photovoltaic

OPVs – Organic Photovoltaics

QDs – Quantum Dots

SEM – Scanning Electron Microscopy

Spiro-OMeTAD – 2,2',7,7'-Tetrakis[N,N-di(4-methoxyphenyl)amino]-9,9' Spirobifluorene

TF - Tolerance Factor

ToF-SIMS - Time of Flight Secondary Ion Mass Spectrometry

V_2O_5 - Vanadium Oxide

V_{OC} – Open Circuit Voltage

XPS – X-ray Photoelectron Spectroscopy

XRD – X-ray Diffraction

List of Figures

List of Tables

1. Introduction & Background

1.1 Why "solar"?

The traditional source of energy includes oil, coal and gas. However, these conventional energy resources are limited on earth. Due to the limitation of availability, it is impossible to rely on conventional energy resources to satisfy the increased demand for consumption. A study done by the US energy department has predicted that by 2050 the demand in energy requirement will sour to double compared to what was observed in the last decade (Figure 1) [1]. The approximate consumption of energy for the entire world population is around 16 TW per year [2]. Clearly, with this speed, the human race will soon run out of conventional energy sources like fossil fuel.

On the contrary, solar energy is abundantly available in nature, so solar energy is considered an alternative renewable energy resource [3]. To add on, greenhouse gas emissions can also be minimized by utilizing solar energy, resulting in lower pollution. Thus, solar energy provides clean and green energy. If the low cost of manufacturing is achieved, then solar energy can replace conventional energy resources [4].

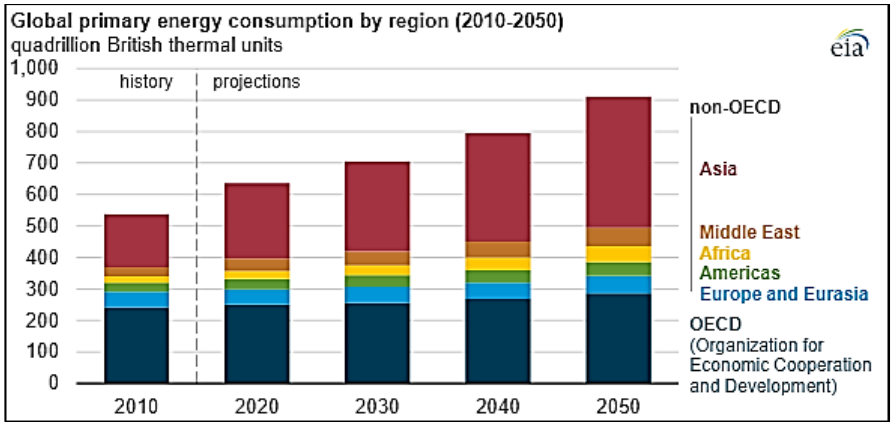

Figure 1 Expected energy consumption [1]

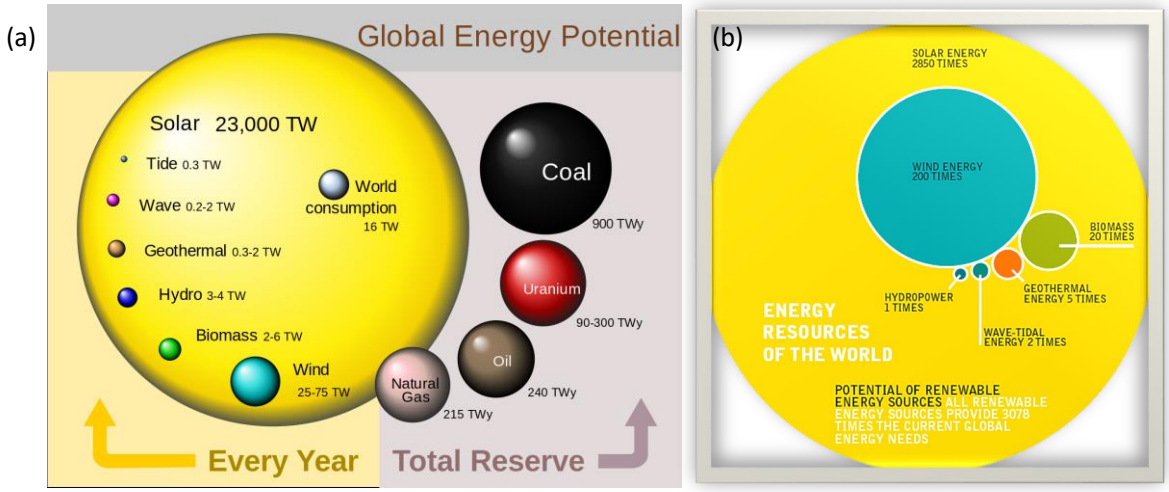

Figure 2 (a)global energy potential (b) availability of energy resources.[2]

1.2 Origin and history of solar cells

Solar cells convert sunlight into electrical energy. A solar cell is a great tool to utilize solar energy. The milestones in the development of photovoltaic technology are dated back to the 18th century. The very first photovoltaic effect was demonstrated by Edmond Becquerel in 1839. Later in 1883, the first solar cell using Selenium wafer was demonstrated by Charles Fritts. Although the efficiency of that solar cell was very low, around ~1%, the solar cell concept was demonstrated well. However, commercial solar cells were first developed by Bell labs in 1954. They used Silicon to produce solar cells, which gave efficiency around 4-5% [5]. Unfortunately, those solar cells were not a very successful commercial product due to the high cost. Therefore, their application became limited to powering satellites and some other space applications. Since then, researchers have been attempting to develop a low-cost solution for PV technology. These resulted in three generations of solar cells (Figure 3) [6]. The first-generation solar cells are mainly comprised of Silicon wafers. The development of Silicon-based solar cells led to very high efficiency, but a significant disadvantage was the very high cost, as discussed. The second-generation

solar cell offered low cost but with compromise in the efficiency. Hence the third generation was developed with the aim that it can be cost-effective as well as efficient, which is still in the research and development phase. The hybrid organic/inorganic perovskite solar cells are an advanced concept in the third generation, followed by dye-sensitized solar cells (DSSC) and organic solar cells [7].

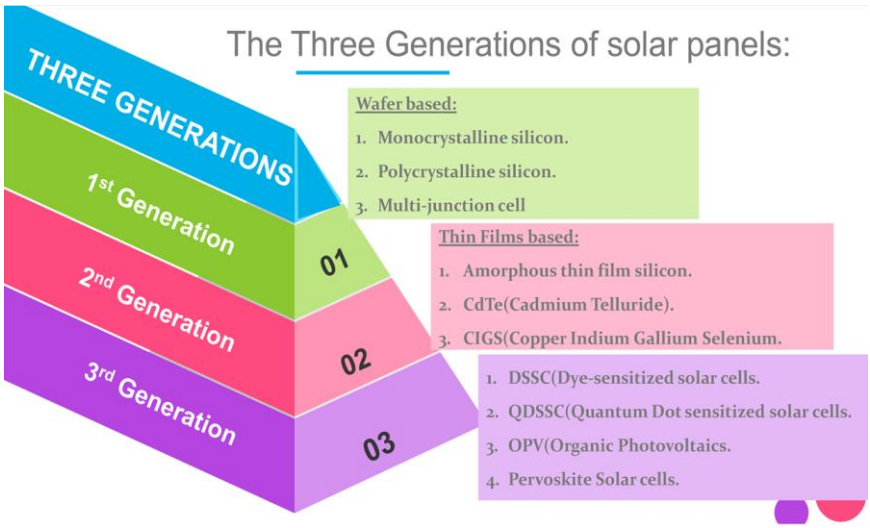

Figure 3: Evolution of photovoltaic technology. [6]

1.3 "Perovskite" solar cells

"Perovskite" is the name of the mineral $CaTiO_3$ discovered in the Ural Mountains of Russia and named after Russian mineralogist Lev Perovski. Nevertheless, this term is being used for all compounds with the general formula ABX_3 with the same crystal structure as $CaTiO_3$ or derived from this structure. Perovskite materials consist of two cations. The cation A is 12 fold coordinated by the anions X and the cation B 6-fold where X can either be oxygen or a halide. In terms of perovskite solar cells, A site can be $MA^+/[CH_3NH_3]^+$, $FA^+/[H_2NCHNH_2]^+$, Rb^+, Cs^+, B site can be Pb^{2+}, Sn^{2+}, Ge^{2+} and X site can be halogens I^-

, Cl^-, Br^-. The choices of the cation and anion rely on the Goldschmidt tolerance factor (t), which predicts a stable crystal structure of perovskite. According to the Goldschmidt tolerance factor, the relationship between the ionic radius of the A-site cation (r_A), B-site cation (r_B) and X-site anion (r_x) is given as shown in equation 1

$$t = (r_A + r_B)/\sqrt{2}\,(r_A + r_B) \quad (1)$$

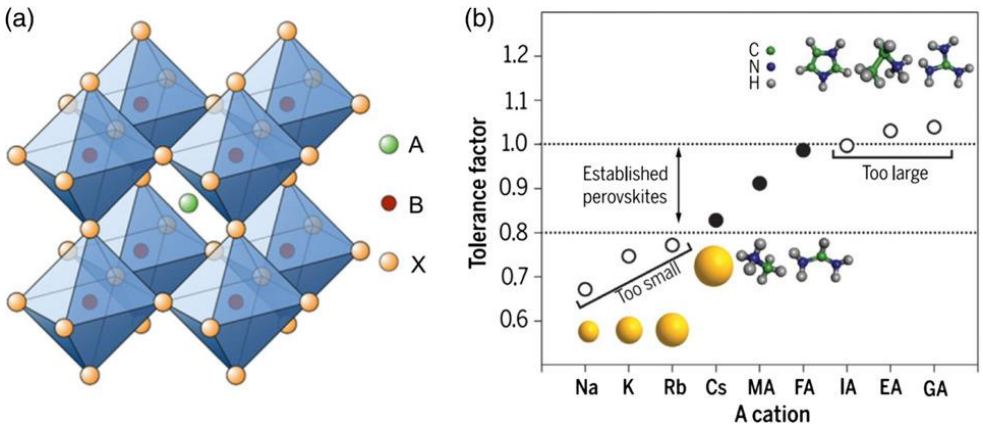

Figure 4 (a) crystal structure of perovskite materials, (b) suitable "A-site" cations for perovskite solar cells.[8]

For many different inorganic or hybrid perovskite light-absorbing layers suitable for photovoltaic application, the tolerance factor lies between 0.8 to 1. Specifically, for methylammonium lead iodide ($MAPbI_3$), the tolerance factor is ~ 0.95. This is why $MAPbI_3$ is the most prominently studied hybrid organic-inorganic perovskite among perovskite solar cells [5,9] and also the main perovskite material for this thesis.

1.4 Advantages of Perovskite solar cells

1.4.1 Excellent optical and electronic properties

The light-absorbing perovskite materials offer many significant advantages. One of them is excellent optoelectronic properties that make them suitable for photovoltaic application. Perovskites are direct bandgap semiconductors that are ambipolar in nature. Perovskite light absorber materials have suitable bandgap (~1.5 eV), decent charge carrier motilities of 2-66 $cm^2\ V^{-1}\ s^{-1}$, long diffusion lengths of charge carriers >1 μm, and low exciton binding energy: 2–50 meV, which helps to achieve better charge transport properties. Also, due to its high absorption coefficients, perovskite light absorber materials can be used in the low light region. Further, the low density of trap states, non-radiative recombination, and high quantum yield make it an exciting candidate for PV technologies [10,11]. A comparison of the photoelectrical properties of perovskite material with other PV technology is shown in Figures 5a and 5b. Further, the improvement in external radiative efficiency allows measuring the improvement in non-radiative losses quantitatively (Figure 5c), providing the benefit of additional gain in V_{oc} and fill factor [12,13].

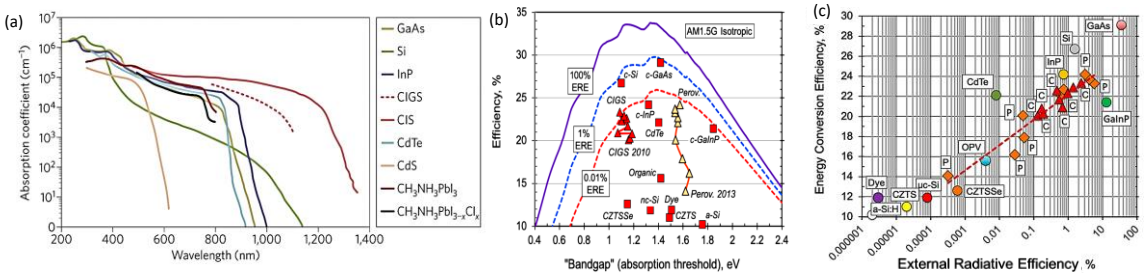

Figure 5 Comparison of PSC with different PV technology (a) absorption coefficients, (b) efficiency vs bandgap (c) external radiative efficiency (P and C stand for Perovskite and CIGS technologies respectively) [9,14].

1.4.2. High open-circuit voltage (V_{oc}) and power conversion efficiency (PCE)

Another vital advantage of the perovskite absorber layer is a high open-circuit voltage produced under the full solar spectrum. Open circuit voltage represents the maximum possible voltage across a solar cell under the sunlight when no current is flowing. As depicted in figure 6a, higher V_{oc} results in higher power conversion efficiencies [15]. In practical terms, this V_{oc} depends on effective bandgap potential loss ($E_g/q - V_{oc}$). Due to lower recombination rates of charge carriers in perovskite, effective bandgap potential loss is very low, as shown in Figure 6b. Thus, perovskite materials have a low loss of potential that further helps attain a higher power conversion efficicncy (PCE) [9,16]. As a result, perovskite solar cells have reached a very high efficiency beyond 25.2 %, comparable to commercially available Si PV technology (Figure 6c) [17].

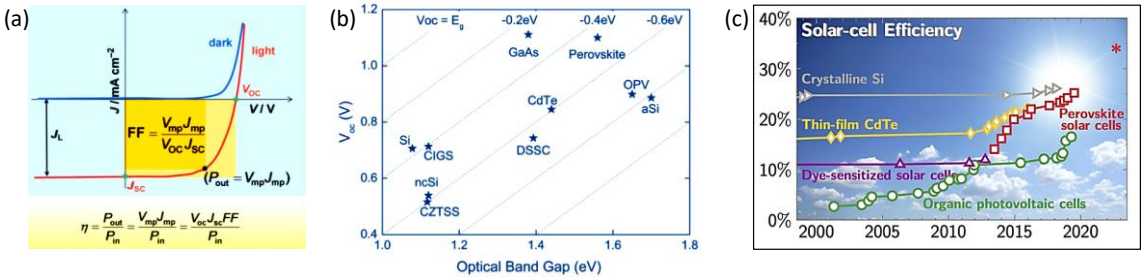

Figure 6 (a) Dependence of PCE on IV parameters [15]. (b) Open-circuit voltage (Voc) versus optical band gap (Eg) of different PV technology [16]. (c) PCE evolution of PSCs [17].

1.4.3. Ease and low cost of manufacturing

The main advantage above all the advantages is the ease and low cost of manufacturing perovskite solar cells. Perovskite solar cells can be easily fabricated using solution processing techniques such as spin coating, drop-casting, slot die coating, doctor blading [5]. On the other hand, commercial Si PV is expensive because of the high cost of manufacturing. The cost comparison of Si PV vs PSC (perovskite solar cells) is illustrated in Figure 7a. The manufacturing of Silicon-based solar cells requires purifying raw silicon

feedstock at very high temperatures (~2000 ˚C) and prepare ingots, which are later sliced into wafers. Those wafers are then processed to form panels. These procedures are energy-intensive. Further, installing those panels adds up the extra cost too. Thus, overall, in terms of payback, the energy and money spent on solar panels are higher than traditional fossil fuel resources [5,18]. Because of the energy-intensive silicon purifying and extraction process, the cost required to produce silicon PV is almost double that of perovskite light absorber materials (Figure 7a). Furthermore, it is projected that to cover 12.5 TWh consumption, three years of current production capacity is needed for silicon. On the other hand, perovskites would just take a few days to produce with the current lead manufacturing technology (Figure 7b) [19]. Thus, combining all these features makes perovskite-based solar cells a potential candidate to replace currently used Si PV technology.

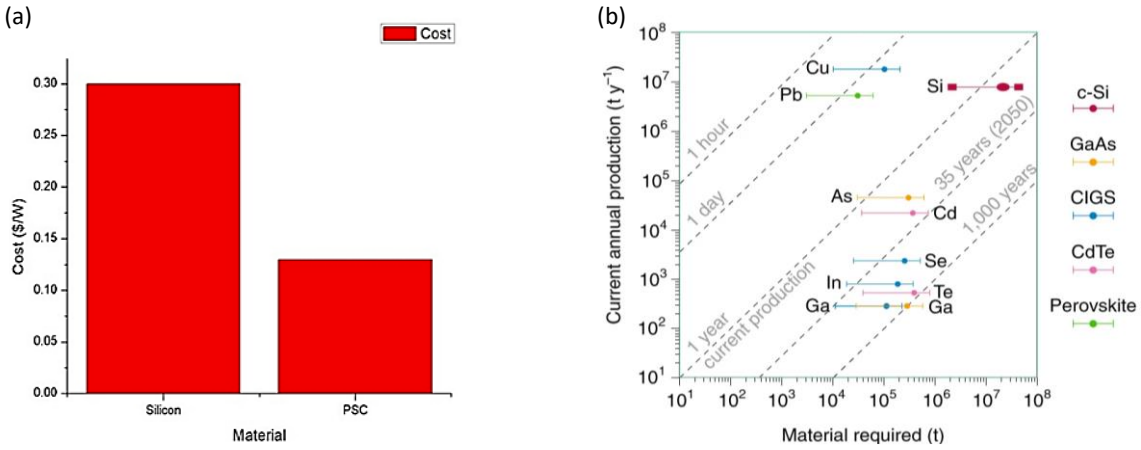

Figure 7 (a) Cost comparison of Si PV vs Perovskite solar cells [5] (b) material production capacity of various PV technologies [19].

1.5 Challenges: stability issues of complex lead halides

Since perovskite solar cells showed rapid progress of improvement in the efficiencies within a decade, they have emerged as future generation PV technology. However, long-term operational stability has been a significant factor that acts as a blockade for the

commercialization of PSCs. Silicon-based PV modules are considered to be stable for 25 years. On the contrary, perovskite solar cells are reported to be stable only for a few hundred hours to a maximum of one year [5]; thus, it faces serious stability issues compared to already available PV technology in the market. These stability issues can be further classified as extrinsic stability challenges and inherent stability challenges.

1.5.1 Extrinsic stability issues

The perovskite-based active layer is susceptible to external factors such as water, air and moisture. Out of many perovskite structures, $MAPbI_3$ perovskite-based active layer is widely explored to understand the degradation mechanism due to various extrinsic and intrinsic factors. Reports have shown that upon exposure to these external factors, PSCs degrade and lose their operational stability.

It was found that in the presence of water, $MAPbI_3$ crystal structure forms hydrates/complex with H_2O (equation 2) and deforms the perovskite structure destroying optoelectronic properties, resulting in loss of photovoltaic performance [20,21].

$$4CH_3NH_3PbI_3+H_2O \leftrightarrow 4CH_3NH_3PbI_3\cdot H_2O \leftrightarrow (CH_3NH_3)_4PbI_6\cdot 2H_2O +3PbI_2+ 2H_2O \quad (2)$$

Further, when $MAPbI_3$ is exposed to moisture under illumination, methyl-ammonium cation gets despoiled and results in PbI_2, I_2 and water (equation 3-6) [5]. Thus, the formation of PbI_2, I_2 and water results in the destabilization of the solar cells.

$$CH_3NH_3PbI_3(s) \rightarrow CH_3NH_3I\ (aq)+PbI_2\ (s) \quad (3)$$

$$CH_3NH_3I\ (aq) \rightarrow CH_3NH_2\ (aq)+HI\ (aq) \quad (4)$$

$$4HI\ (aq)+O_2\ (g) \rightarrow 2I_2\ (s)+2H_2O \quad (5)$$

$$2HI\ (aq) \rightarrow H_2\ (g)+I_2\ (g) \quad (6)$$

Whereas the exposure of $CH_3NH_3PbI_3$ photo-active layers to light and dry oxygen results in superoxide (O_2^-) species. This reactive O_2^- species can deprotonate the methylammonium cation ($CH_3NH_3^+$), leading to the formation of PbI_2, water, methylamine and iodine [22–24], as shown in equation 7.

$$4CH_3NH_3PbI_3+O_2^- \rightarrow 4CH_3NH_2+2I_2+2H_2O+4PbI_2 \quad (7)$$

Though, the impact of these external factors can still be minimized by encapsulating the active layer. However, it may result in loss of performance or increment in cost.

1.5.2 Intrinsic stability issue

Ironically, $MAPbI_3$ is intrinsically unstable as well. It means that in the presence of light and heat, $MAPbI_3$ tends to decompose. In practical terms, these conditions are unavoidable for the operation of a solar cell. When the temperature is above 85℃, $MAPbI_3$ forms ammonia or other volatile species and PbI_2 (equation 8) [21,25].

$$CH_3NH_3PbI_3 \rightarrow PbI_2 + CH_3I+NH_3 \quad (8)$$

Whereas, in the presence of light and temperature, the degradation pathways are reported as equations 9-10.

$$CH_3NH_3PbI_3 \rightarrow [PbI_2]+ \text{volatile species (rising from } CH_3NH_3I) \quad (9)$$

$$PbI_2 \rightarrow Pb^{2+} + 2I^- \rightarrow Pb^+ + I^0 + I^- \rightarrow (1/2)Pb^0 +(1/2)PbI_2 + (1/2)I_2 \quad (10)$$

In the presence of light and heat, PbI_2 is further decomposed and results in metallic lead and molecular iodine formation, as mentioned above [20,26].

Thus, this Pb^0 and iodine create defect sites resulting in instability of perovskite solar cell devices. These defect sites are often reported to be within the grains, at grain boundaries,

or at the surface of the $CH_3NH_3PbI_3$ perovskite layer. Moreover, these trap states can also alter the energy level alignment and destroy charge transfer properties in $CH_3NH_3PbI_3$ solar cell devices. Besides, non-radiative recombination becomes more prominent in such a scenario, a clear indication of deterioration of device performance. Therefore, it is crucial/important to chemically passivate these defect sites to achieve longer stability of the $CH_3NH_3PbI_3$ layer [23]. To do so, additives are often employed, i.e. a compound is added into the perovskite precursor.

2. Literature Review

So far, there is no proper rule of selection to choose additive for the $MAPbI_3$ light-absorbing layer. The majority of the additives have opted from already available literature or experimental data related to dye-sensitized solar cells (DSSC), for which additives are often categorized based on N, O, S atoms serving as electron donors. Since these electron donor atoms can bind /coordinate with Pb^{2+} species, it can result in adduct formation, passivate the grain boundaries, and improve efficiency and stability. Further, based on the electron-donating atoms, additives are subcategorized as amines, nitriles belonging to the N donor atom, amides, acids, acetates, alcohol, ester, ether belonging to the oxygen donor atom and sulfides, thiocyanates belonging to the S donor atom [27]. Following the same idea, here, additives are classified as organic and inorganic additives for the $MAPbI_3$ perovskite layer with further classifications as mentioned above. Thus obtained analysis of the available literature is then published in a reputed journal which can be accessed at https://doi.org/10.3390/cryst11070814

2.1 Organic additives

2.1.1 N donor atom-based additives

2.1.1.1 Amine additives

Scientists commonly refer to amine-based additives. Following the recommendation, the non-stoichiometric use of methylammonium iodide as an amine additive was investigated in the early phases of developing perovskite solar cells. It was established that adding excess MAI reduces defect traps density, increases PL lifetime, and further increases PCE regardless of fabrication methods [28–30]. Likewise, some other organic amine derivatives such as benzylammonium iodide (BAI) and Phenethylamine iodide (PEAI) have also been investigated as additives and found to improve light harvesting properties and exciton lifetime with reduced charge recombination [31,32]. Besides, attaching hydrophobic cations

within amine additives, such as hexylamine hydrochloride (1-HH), 1,6-diaminohexane dihydrochloride (1,6-DD) and phenylhydrazinium iodide (PHAI), may even work as a protection for the $MAPbI_3$ film against moisture, improving the stability in ambient conditions [33,34]**.** Later, it was found that if instead of iodide, chloride-based counterpart (such as MACl instead of MAI) was used as an additive, perovskite films became more crystalline, with increased grain size and homogenous, smooth morphology, which further resulted in grain boundary passivation, resulting in better performance. Unfortunately, the addition of MACl was reported to form mixed halide perovskite $CH_3NH_3PbI_{3-x}Cl_x$ (as the objective perovskite was $CH_3NH_3PbI_3$) [35–37]. Although there were opposite reports about mixed halide formation. It was shown that when other halide ions, i.e. X=Br/Cl, are used with a minimum concentration in $MAPbI_3$ precursor, it does not affect $MAPbI_3$ characteristics, and the final perovskite remains crystalline $MAPbI_3$ phase-only instead of mixed halide perovskite. This is because a low concentration of halide ions can quickly evaporate as the films are annealed during the fabrication process. Some of the examples of such additives are Amphiphilic hexadecyl trimethyl ammonium bromide(CTMAB), ethyl ammonium chloride (EACl), 1,3-diaminoguanidine monohydrochloride (DAGCl), methoxyammonium chloride (MeOCl), 2, 2, 2-trifluoroethylamine hydrochloride (TFEACl), benzenamine hydrochloride(BACl), 3-chloropropylamine Hydrochloride (3-CPACl), diethylamine hydrochloride (DEACl) [38–42].

Furthermore, nitrogen-containing heterocyclic amines play a great role in improving stability [43]. For instance, the introduction of 4, 4'-bipyridine in $MAPbI_3$ demonstrated complex adduct formation with PbI_2, slowing down the metallic lead formation, thus improved intrinsic stability against illumination [44]. Additionally, it has been shown that the presence of reduced N atoms prevents the loss of volatile species by reacting with Pb^{2+} from the perovskite film and acts in a similar way as polymeric passivation coating. Further, such a passivation effect was visible morphologically (in the SEM cross-section images and energy dispersive X-ray analysis) when PVC was added in $MAPbI_3$ [45]. Later,

scientists designed pyridine derivatives with units containing different multifunctional groups. One such additive is (C_{60}-PyP), which contains C_{60} units that are hydrophobic in nature and pyridine units which chelates Pb^{2+} by donating lone electron pair on the N atom. It is known that uncoordinated Pb^{2+} ions are considered trap states at grain boundaries and can block charge extraction [46]. Thus, grain boundaries are passivated by assisting coordination interactions with the Pb^{2+} ion of $MAPbI_3$ and PyP unit that further improved short circuit current density J_{sc} and eliminated ion migration, while the hydrophobic C_{60} unit does not let moisture directly affect the film [46]. Similar results were noticeable when pyridine-2-carboxylic lead salt ($PbPyA_2$) and polyvinylpyrrolidone (PVP) additives were employed in a $MAPbI_3$ precursor [35,47]. To add on, solvent additives with heterocyclic nitrogen-containing units also demonstrated similar results. In an investigation, Zhang and co-workers demonstrated that N-methyl-2-pyrrolidone (NMP) as a solvent additive when added in dimethylformamide (DMF) resulted in a high quality of perovskite film due to a Lewis acid-base reaction with the Pb atom. The study revealed that intermediates obtained with different PbI_2/NMP ratios are of the same kind, because of which the solar cell performance and stability do not depend on the NMP ratio in the precursor [48]. Following the idea of Lewis acid-base interaction, Kim and co-workers explored pyrrolidone-based solvent additives and compared them with a commonly used DMF based precursor [49]. For pyrrolidone-based solvent additives, different N-substituents: N-methyl-2-pyrrolidone (NMP), N-ethyl-2-pyrrolidone (NEP), N-cyclohexyl-2-pyrrolidone (CHP), and N-octyl-2-pyrrolidone (NOP) were employed. During the in situ crystal growth, it was observed that a solvent additive containing the pyrrolidone structure with a higher boiling point results in a lower vapour pressure over the pristine DMF based precursor. Thus, it resulted further improvement in the morphology of the perovskite film since the N substituent becomes bulkier with a higher boiling point (The boiling points of NMP, NEP, and CHP and NOP are 154˚C, 202˚C, 204 ˚C, 286 ˚C, 303 ˚C). Furthermore, it was discovered that the strength of coordination of a solvent component influenced the intermediate formation with PbI_2, which, in turn, was influenced by the boiling point of the solvent. This was based on the

evidence when the intermediate phase was found to vanish with a CHP solvent additive, whereas the pure DMF solvent without pyrrolidone-based solvent additives showed DMF: PbI_2 solvate formation. Therefore, it was suggested that the bulkier additive solvent suppress the DMF: PbI_2 solvate formation, which lacks stability when used without any cosolvent [49]. Some other derivatives such as DMI , 1-(4-ethenylbenzyl)-3-(3,3,4,4,5,5,6,6,7,7,8,8,8-tridecafluorooctylimidazolium iodide (ETI), 1-methyl-3-propylimidazolium bromide (MPIB), 1-butyl-3- tetrafluoroborate (BMIMBF4) are other examples that result in improved PCE and ambient stability due to hydrophobicity of N atoms within a ring like structure [50–52].

The chemical structures of the above-discussed amine additives are shown in Figure A0.1, Appendix, 0.

2.1.1.2 Cyano/nitrile additives

Subsequently, it was observed that the cyano group-containing N atom could be equally effective to passivate grain boundaries [53]. Triazine-graphdiyne (Tra-GD) is a graphene-like material that consists of pyridine-like nitrogen in the highly conjugated framework. It was suggested that a balanced charge distribution in the C=N bond in the triazine ring promotes stronger interaction with Pb^{2+}, resulting in a very tight contact between these two materials. This, in turn, did not allow the ion migration on the surface and successfully passivated grain boundaries [53]. Similarly, graphitic carbon nitride addition also resulted in good morphology due to highly compact bonding between Pb^{2+} and N of C=N that further endorsed to achieve power conversion efficiencies up to 21.1% (aperture 0.16 cm^2) and 19.5% (aperture 1.0 cm^2), featuring an open-circuit voltage of 1.16 V (corresponding to a slight voltage loss of 0.39 V) and improved operational device stability (~90% initial efficiency retained after constant one sun illumination for 500 h) [54,55]. Further, Zhou and co-workers demonstrated that by employing 1,8- Diazabicyclo[5.4.0]undec-7-ene (DBU), the formation of I^- can also be suppressed due to adduct formation with PbI_2 [56]. Besides,

another solvent additive, acetonitrile (ACN), also showed improvement in morphology due to adduct formation with PbI_2 when added in a DMF based precursor. This further proved to increase PCE from 15.04% to 19.7%, which remained stable without encapsulation for 160 h, with the PCE remaining ~60% of the initial value when exposed to the white light [57]. Figure A0.2, Appendix 0, shows the chemical structures of the nitrile additives mentioned above.

An overview of the influence of amines and nitrile additives on stability is shown in Figure A0.3, Appendix 0. Further, Table 1 below shows the effect of N donor atom-based additives on the PCE, stability and stability condition of $MAPbI_3$ PSC.

Table 1 Additives based on nitrogen donor atom containing amines or nitrile[58]

Additive in active layer	Architecture	PCE, % (Pristine)	Stability (Pristine)	PCE, % (with additive)	amount of additive	Stability with additive	Stability conditions	Role of additive	Ref
Excess MAI	FTO/ SnO_2 /$CH_3NH_3PbI_3$/PCBM/Ag	15.14	N/A	17.24	Molar ratio (PbI_2: MAI) =1:1.05	N/A	N/A	Hot casting, improved crystallinity, decrease in defect density, increased PL lifetime.	[28]
Excess MAI	ITO/PCBM/$CH_3NH_3PbI_3$/HTL/Au	N/A	N/A	N/A	MAI: PbI_2 molar ratio = 3:1	N/A	N/A	Vacuum deposition, increase PL lifetime, reduced trap states	[29]
Excess MAI	FTO/ TiO_2 / $CH_3NH_3PbI_3$/Spiro-OmATAD/Au	11.13	N/A	13.37	0.2 mM	N/A	N/A	Sequential deposition, Good quality perovskite film and increment in recombination rate	[30]
benzylammonium iodide (BAI)	FTO/TiO_2/ $CH_3NH_3PbI_3$/HTL/metal	6.83	N/A	9.05	molar ratio BAI/MAI = 0.2	N/A	N/A	better light harvesting property and low charge recombination	[31]
Phenethylamine iodide (PEAI)	FTO/ c-TiO_2/ m-TiO_2 / mp- ZrO_2 / $CH_3NH_3PbI_3$/ Carbon	6.3	Retained ~77% PCE after 80 days	8.60	molar ratio of PEAI	Retained 90% PCE	air, light-100mw/cm^2 ,	better contact with TiO_2, longer exciton	[32]

					:MAI = 1:20	after 80 days		lifetime Good quality of perovskite film	
Hexylamine Hydrochloride (1-HH)	Glass/ITO/PEDOT:PSS/ $CH_3NH_3PbI_3$/PCBM/BCP/Ag	14.37	Retained 43% PCE from initial after 16 days	15.70	0.05 wt%	Retained ~85% PCE from initial after 16 days	Un-encapsulated, ambient, RT, air, RH=10-20%	Increases grain size and passivate defects, NH^{3+} group could form N-H…I. hydrogen bond with the I- of the $[PbI_6]^{4-}$ passivating "A" vacancy; hydrophobic hexane alkyl chain protects against moisture	[33]
1,6-Diaminohexane Dihydrochloride (1,6-DD)				17.00		Retained 90% PCE from initial after 16 days			
phenylhydrazinium iodide (PHAI)	FTO/PEDOT:PSS/ $CH_3NH_3PbI_3$/PCBM/Rhodamine/Ag	14.63	a) Retained ~53 % PCE after 60 days b) died in 20 days	17.2	10 mg/mL	a) Retained ~90 % PCE after 60 days b) Retained ~85 % PCE after 20 days	a) unencapsulated, N_2, dark, RH=20%, T=26 ˚C b) (unencapsulated), ambient room environment (dark) at 30 ± 5% RH and 24 ± 2 °C	PbI_2 and PHAI complex/intermediate formation results in passivation against vacancy defects Hydrophobic phenyl rings acts barrier against moisture	[34]
Amphiphilic hexadecyl trimethyl ammonium bromide(CTMAB)	Glass/FTO/TiO_2/ $CH_3NH_3PbI_3$ /Spiro/Au	17.05	Retained 70 % PCE after 40 days	18.03	10mg CTMAB in 1 ml	Retained 95 % PCE	Non-encapsulated, RH~40%,	Improved crystallinity and morphology	[38]

					DMSO. Used 20 uL of this to add in 1 ml precursor	after 40 days	T=25˚C, dark		
ethylammonium chloride (EACl)	Glass/FTO/c-TiO_2/meso-TiO_2/ $CH_3NH_3PbI_3$/HTL/Au	17.35	Retained ~30% of the original PCE after 1000 h	20.3	2.5% , molar %	Retained ~89% of the original PCE after 1000 h	encapsulated	Improves morphology, grain boundary passivation	[39]
1,3-diaminoguanidine monohydrochloride (DAGCl)	Glass/ ITO/PolyTPD/ $CH_3NH_3PbI_3$/$PC_{61}BM$/ZrAcac/Ag	19.1	Retained 70% PCE after 20 days	20.3	0.6%, wt% of MAI	Retained 80% PCE after 20 days	Non-encapsulated , ambient, RH~50%	Increased grain size, reduced trap density, DAG cation can bond with I^- via hydrogen	[40]
methoxyammonium chloride (MeOCl)	FTO)/compact-TiO_2 layer/mesoporous-TiO_2 layer/ $CH_3NH_3PbI_3$ /spiro-MeOTAD)/Ag	17.15	N/A	19.71	PbI_2/MeOCl molar ratio =1:0.10	N/A	N/A	Improvement in Grain size and crystallinity	[41]
2, 2, 2-trifluoroethylamine hydrochloride (TFEACl)	Glass/ITO/PEDOT:PSS/ $CH_3NH_3PbI_3$/PCBM/Al	N/A	N/A	4.98	molar ratio of additive :MAI : PbI_2 = 0.4:1:1	N/A	N/A	Compact smooth high quality film	[42]
benzenamine hydrochloride (BACl)				11.07					
3-chloropropylamine hydrochloride (3-CPACl)				8.21					

diethylamine hydrochloride (DEACl)				9.89					
4-ethylamine Phenylphosphate disodium salt (EAPP)	FTO/C-TiO_2/mp-TiO_2/$CH_3NH_3PbI_3$/Spiro/Ag	18.83	(a) Dead in 6 h (b) Remained 60% from initial PCE after 100 h	17.61	1 mol%	(a) Remained 90% from initial PCE after 12 h (a) Remained ~99% from initial PCE after 100 h	(a) ATM condition, RH=80%, un-encapsulated, (b) inert, N_2, un-encapsulated,	phenylethylamine group protects against moisture and improves ambient stability, phosphate sodium prevents the formation of $(CH_3NH_3)_4PbI_6.H_2O$,	[59]
4,4'-bipyridine	Glass/ $CH_3NH_3PbI_3$	N/A	Died in ~900 h	N/A	5 wt %	Remained active for 1400 h	inert, un-encapsulated, 70-80 mW/cm^2, 50-60 C	Forms complex with PbI_2 thus slows down the formation of metallic lead	[44] (Our work)
poly 4-vinylpyridine (PVP)	FTO/TiO_2/$CH_3NH_3PbI_3$/Spiro/Au	6.09	Remained 1.55% PCE as of final PCE (absolute value) after 3 weeks	13.07	0.4 wt%	Remained 6.6 % PCE as of final PCE (absolute value) after 3 weeks.	Air, 50%RH, non-encapsulated	inhibits carrier recombination, reduced defects	[60]
Polyvinylcarbazole (PVC)	ITO/PTAA/$CH_3NH_3PbI_3$/PCBM/Al	17.4	Died in 1500 h	18.7	1 mass%	Retained ~70% of the initial efficiency after light soaking for 1500 h,	light power of 50±3 mW/cm^2, the temperature of 65±2 ˚C in inert nitrogen,	Defect passivation due to interaction with lone pair of electrons from N atom with Pb^{2+}	[45]
pyridine-functionalized fullerene derivative (C60-PyP)	ITO/TiO_2/ $CH_3NH_3PbI_3$ /Spiro-OMeTAD/Au	17.61	Retained 70% PCE after 30 days	19.82	0.13 wt %	Retained 90% PCE after 30 days	25 ℃, RH=30%, dark, non-	Enlarged grain size, improved crystallization, interaction b/w N atom of the	[46]

							Encapsulation, mppt-n/a, uv-filter-n/a	pyridine moiety within C60-PyP and Pb^{2+} ion within MAPbl3 leads to the passivation of trap states of perovskite layer, hydrophobic nature of C60-PyP molecule increases ambient stability	
pyridine-2-carboxylic lead salt (PbPyA2)	ITO/P3CT-N / $CH_3NH_3PbI_3$/ (PCBM)/C_{60}/ (BCP)/Ag	18.86	(a) Retained 20% of PCE after 480 h (b) retained 20% of PCE after 540 h (c) retained 30% of PCE from initial after 480h	19.96	4mg mL−1	(a)Retained 80% PCE after 480 h (b) retained 93% of initial PCE after 540 h (c) retained 90% PCE from initial after 480h	(a)90 °C,RH 40–60%, dark, not encapsulated, (b)MPP-tracking, non-encapsulated, white light-100mW/cm^2, inert, 25C, (c) Air, non-encapsulated, dark, RH 40–60%	Controlled crystallization, passivation of grain boundaries, the interaction of pyridine and carboxylate to cations increases hydrophobicity	[47]
polyvinylpyrrolidone (PVP)	Ito/SnO_2/ $CH_3NH_3PbI_3$/Spiro/Au	15.33	Retained 76% from initial PCE after 400 h	15.19	1 mg mL-1	Retained 80% of the initial PCE after 60 days	encapsulated, Ambient, RH-10%, RT,	Lewis base, the pyridine part (side chain) of the PVP polymer, can passivate the surface defects caused by misaligned lead	[35]

								ions and can fill the iodine vacancy traps on the surface of the perovskite film, c=o also stabilizes, allows not to degrade	
2-pyridylthiourea	FTO/C-TiO_2/mp-TiO_2/ $CH_3NH_3PbI_3$/Spiro/Au	15.5	a)Retained only ~10 % PCE from initial after 30 days b)Retained~ ~55 % PCE from initial after 30 days	18.2	0.5 mg mL-1	a)Retained ~95 % PCE from initial after 30 days b)Retained ~92 % PCE from initial after 30 days	ambient, air, dark a)RH= 55±5 %, dark, RT b) 65 ˚C, Rh=30%,dark,	N-donor and S-donor to coordinate with PbI_2 and slow down the formation of PbI_2. improved morphology, larger crystal size	[61]
NMP	FTO / ZnO-MgO-EA+ /mesoporous-TiO_2 / $CH_3NH_3PbI_3$/spiro-OMeTAD / Au	18.0	N/A	19.2	PbI_2/NMP molar ratios of 1:2	N/A	N/A	The same kind of intermediate, regardless of NMP ratio, results in excellent morphology	[48]
NMP	Glass/ITO/PEDOT:PSS/$CH_3NH_3PbI_3$/ $PC_{61}BM$/Al	1.50	N/A	7.03	60 µl in 1 ml precursor	N/A	N/A	lewis acid base interaction	[49]
NEP				10.04				-	
CHP				12.87				suppression of solvate formation	
NOP				2.79				lewis acid-base interaction	

DMI	FTO/compact-TiO_2/ $CH_3NH_3PbI_3$/Spiro-OMeTAD/Au	10.72	N/A	14.54	10 vol% in 1 ml precursor	N/A	N/A	Pb-O bond formation due to lewis adduct between DMI and Pb	[62]
1-(4-ethenylbenzyl)-3-(3,3,4,4,5,5,6,6,7,7,8,8,8-tridecafluorooctylimidazolium iodide (ETI)	FTO/C-TiO_2/mp-TiO_2/ $CH_3NH_3PbI_3$/Spiro/Au	19.2	(a)Retained 49% PCE from initial 700 h (b)Retained 60% PCE from initial 700 h	19.5	1 mol%	(a)Retained 85% PCE from initial 700 h (b)Retained 80% PCE from initial 700 h	(a) MPPT inert,60 °C, 100mw/cm2, un-encapsulated, (b)RH=40%, RT, dark,air	enables the full transformation into precursor, ii) suppresses thermal decomposition pathway and iii) provides outstanding hydrophobicity within the active material	[50]
1-methyl-3-propylimidazolium bromide (MPIB)	ITO/PEDOT:PSS/ $CH_3NH_3PbI_3$/$PC_{61}BM$/BCP/Ag.	15.9	retain ~50% of its original PCE after 150 h	18.2	0.5 mg in 1 ml	retain 78 % of its original PCE after 150 h	atmospheric environment, RT,	(1) passivation of the uncoordinated Pb2+ to reduce the defects in the perovskite film due to the lone-pair electron in its cation group, and (2) beneficial to promote crystal growth to improve film quality	[51]
BMIMBF4 1-butyl-3-tetrafluoroborate	ITO/NiOx / $CH_3NH_3PbI_3$ /C_{60} /Ag	18.13	retaining 30% of their initial PCE after thermal ageing of	18.07	0.4 mol%	retaining 80% of their initial PCE after thermal	at 85 ˚C, un-encapsulated,	thermal stability by effective suppression of perovskite decomposition	[52]

			400 h at 85 ˚C			ageing of 400 h at 85 ˚C			
triazine-graphdiyne (Tra-GD),	ITO/P3CT-K/ $CH_3NH_3PbI_3$/PC61BM/ZnO/ Al	17.90	Died in 1100 h	20.33	2 mg/ml	Retain above 90% after 1100 h	un-encapsulated ,	interacts with Pb2+ at grain boundaries and passivates grain boundaries and inhibits ion migration	[53]
graphitic carbon nitride(g-C_3N_4)	FTO/compact TiO_2/ $CH_3NH_3PbI_3$ /Spiro-MeOTAD/Au	18	Retained 46 % PCE after 300 h	21.6	0.1 wt%	Retained 90% PCE from initial after 500 h	Encapsulated , 100 mw/cm^2,	Improves grain size and crystallinity passivates grain boundaries. C=N to interact with Pb^{2+} that forms compact tight bonding resulting in good morphology	[54]
graphitic carbon nitride (g-C_3N_4)	FTO/ compact TiO_2/ $CH_3NH_3PbI_3$ /Spiro-OMeTAD/MoO_3/Ag	16.22 ± 0.83	N/A	19.34 ± 0.63	0.4 mg mL	N/A	N/A	Passivation , enhanced crystallinity, C=N to interact with Pb^{2+}, increases the conductivity and carrier mobility	[55]
1,8-Diazabicyclo[5.4.0]undec-7-ene (DBU)	Glass/ITO/NiOx/ $CH_3NH_3PbI_3$/PCBM/PEI/Ag	15.98	Retained 50% PCE from initial after 10 days	18.13	3% weight ratio	Retained 80% PCE from initial after 10 days	un-encapsulated , inert (N_2,) mpp tracking	Iodine quencher, adduct with PbI_2 (C=N interaction with Pb^{2+}), reduced defects, high-quality perovskite film	[56]

acetamidine salt (AcHc)	ITO/TiO_2/ $CH_3NH_3PbI_3$ /Spiro-OMeTAD/Au	15.45	N/A	16.54	Molar ratios of MAI and AaHc = 1 : 0.08	N/A	N/A	smooth film, full and uniform coverage, large grain size, improve carrier lifetime,	[63]
Spiro-OMeTAD	FTO/ Den TiO_2/mp-TiO_2 /$CH_3NH_3PbI_3$/spiro-OMeTAD/Au	15.52	N/A	17.77	0.01 wt %	N/A	N/A	Facilitates charge transport	[64]
ACN	ITO/TiO_2/ $CH_3NH_3PbI_3$ /Spiro-OMeTAD/Au	15.04±0.48	Remained ~20 % of initial PCE after 150 h	19.7	Molar ratio of ACN: PbI_2 is 0.5	Remained ~60 % PCE after 150 h	100 $mW{\cdot}cm^{-2}$ RH= 60%-90% , in air without encapusulation	morphology enhancement	[57]

RH= relative humidity

2.1.2 O donor atom-based additives

Additives containing an O atom as Lewis base may consist of various functional groups such as carbonyls, carboxyl, carboxylates, ester, ethers, alcohols [27].

2.1.2.1 Carbonyl and amide additives

One of the systematically investigated additives is urea. Urea is an eco-friendly compound consisting of a carbonyl group known to interact with PbI_2 [65]. It has been illustrated that PbI_2 and urea forms an intermediate $PbI_2.O=C(NH_2)_2$ when added to the PbI_2 precursor solution in the double-step spin coating process. The oxygen atoms act as a Lewis base, whereas Pb^{2+} acts as a Lewis acid, resulting in the formation of a Lewis acid-base adduct. This adduct formation further results in large, flat grains resulting in a smooth film morphology [66]. Similar results were observed for the single-step spin coating process, resulting in grain boundary passivation, improved crystalline film and suppressed non-radiative recombination losses, further improving the efficiency of solar cells. [67]. Moreover, it was shown that incorporating amides in $MAPbI_3$ changes the Fermi level by interacting with Iodine defect vacancy/site, reducing the density of trap sites and increasing the work function of $MAPbI_3$ perovskite, helping voltage gain. At the same time, the carbonyl group transfers electrons to perovskite, reducing the Fermi level, which in turn helps to achieve better charge transport properties [68]. Recently, the addition of biuret (a variant of urea) in $MAPbI_3$ precursor ascribed the intermediate formation with PbI_2 to the electron delocalization in the N-C=O-N system in the presence of carbonyl group and explained the cause of peak shift for C=O vibration in FTIR spectra. (in the case of biuret-modified $MAPbI_3$ film from 1722 to 1713 cm^{-1}) [69]. Some other additives such as benzoquinone (BQ), triazine perylene diimide (TPDI), 3,4-dihydroxybenzhydrazide (DOBD), benzamidine hydrochloride (BMCl) containing the carbonyl group have revealed similar properties [70–74]. Likewise, it was also presented that if a hydrophobic ring is attached within the additive framework in combination with the carbonyl group (Isatin-Cl additive), it also acts as a shield against humidity in ambient conditions, helping to maintain the PCE nearly to 95 % of the initial state [75]**.** Besides, the usage of the carbonyl group can also be expanded to improve the flexibility of flexible, printable solar cells (FPSC). Polycaprolactone (PCL) additive in $MAPbI_3$ has shown desirable improvement in PCE as well as mechanical strength. This improvement in mechanical stability was ascribed to a two-fold increase in grain size (from

200 nm to 400 nm) and homogenous grain distribution, leading to improved mechanical stability that maintained PCE more than 90 % of the initial state after 300 cycles for the radius from 20 mm to 4 mm and stability under illumination for 350 h [76].

2.1.2.2 Sulphonyl additives

Furthermore, carbonyl-based additives are often compared with the sulphonyl-based group, where the O atom is connected to different species, (i.e. S atom instead of C atom). Fang and co-workers have done one such study in which the strength of Pb coordination of sulphonyl group containing additive was compared with carbonyl-based additive. To do so, two novel fused ring non-fullerene acceptor materials IDIS-Th and IDIC-Th were introduced into $MAPbI_3$. IDIC-Th had the Lewis base functional group carbonyl (C=O), and IDIS-Th had a sulfonyl group (O=S=O). Since the sulfonyl group (O=S=O) is a stronger electron-withdrawing group compared with carbonyl (C=O), the sulfonyl group was predicted to have a stronger interaction with Pb ions than carbonyl (C=O) because the two sulphur-oxygen double bonds can chelate Pb^{2+} with stronger interaction. Besides, it was noticed that replacing carbonyl with a sulfonyl group can effectively downshift the lowest unoccupied molecular orbital (LUMO) level of IDIS-Th, which indicated the sulfonyl group is a stronger electron-withdrawing group. Thus, the interaction with Pb would reduce the defect traps density. Further, to confirm the defect passivation effect of IDIC-Th and IDIS-Th, the trap densities (n_{trap}) in bulk $MAPbI_3$ films were calculated and found to be 8.85×10^{15} cm^{-3} and 4.20×10^{15} cm^{-3}, respectively. Undoubtedly, the sulphonyl group reduced the defect states. This further reflected improvements in the contact angles of the film (which signifies an improvement in hydrophobicity of the films). The improvement in hydrophobicity indicated that the additive molecules at the GBs and surface could inhibit the raid of moisture to $MAPbI_3$ films /prevent moisture from penetrating $MAPbI_3$ film. Although, both IDIC-Th and IDIS-Th are known for their hydrophobic nature. Nevertheless, these changes reflect further improvement in hydrophobic nature. Besides, the influence of the two molecules on photovoltaic performance was also examined. The PSC with IDIS-Th molecule showed significant improvement in PCE and reached up to 20.01%. To add on, due to the strong passivation effect of IDIS-Th, PSC with IDIS-Th demonstrated superior stability over PSC with IDIC-Th in ambient conditions under solar radiation and in the dark at high temperature [77]. Likewise, a comparison of solvent additives hexamethyl phosphoric triamide (HMPA) and dimethyl sulphoxide (DMSO) were

made, which was further compared to solvent additive NMethyl-2-pyrrolidone (NMP). Here, Lewis basicity, donor number (D_N), and boiling point of solvents were utilised as comparison parameters to correlate the role of solvents in regulating morphology. This investigation done by Cao and Wei co-workers highlighted that the larger the donor number, the stronger is the Lewis basicity of the solvent additive. The donor number of DMF, NMethyl-2-pyrrolidone (NMP), dimethyl sulphoxide (DMSO), and hexamethyl phosphoric triamide (HMPA) are 26.6, 27.3, 29.8, and 38.8, respectively. Therefore, it was suggested that the Pb-O bond strength would increase with an increase in the donor number of additive [78,79]. Hence, NMP, DMSO and HMPA have been expected to form stronger intermediates over pure DMF. In addition, it is also observed that the strong Lewis base additives exhibit higher boiling points. (The boiling point of DMF, NMP, DMSO, and HMPA are 152, 202, 189, 235 °C, respectively) [80,81]. This, in turn, reduces the evaporation rate of the solvent during the spin-coating process, resulting in a good film morphology. As a result, DMSO followed by NMP cosolvents displayed excellent PCE of 14.66% and 16.17% over pristine DMF (12.25%). As no residue of PbI_2 remained, and complete conversion into perovskite resulted in less resistance [82]. Further, other solvent additives based on O donor atoms, such as tetramethylene sulfone (TMS) [83] and tetrahydrothiophene oxide (THTO), also utilized a similar mechanism of forming the Pb-O bond and improved performance and stability [84]. The chemical structure and influence of amides/carbonyl and sulphonyl group based additives on the stability of the $MAPbI_3$ layer have been presented in Figure A0.4, Appendix 0 and Table 2 respectively.

Table 2 A summary of additives containing Amides/carbonyls/sulphonyl functional group in $MAPbI_3$ active layer.[58]

Additive in active layer	architecture	PCE, % (Pristine)	Stability (Pristine)	PCE, % (with additive)	amount of additive	Stability with additive	Stability conditions	Role of additive	Ref
Urea	Glass/ITO/PEDOT:PSS/ $CH_3NH_3PbI_3$ /PCMB/BCP/Al	15.1	Retained ~35% from original PCE after 2 h	17	molar ratio of the urea: lead acetate = 0.5	Retained ~60% from original PCE after 2 h	Light, 100mW/cm^2, 50-60˚C, inert, unencapsulated	interaction of carbonyl group of urea with PbI_2 results in crystalline film , resulting passivation and improvement in stability	[65]
Urea	ITO/PEDOT:PSS/PbI_2/MAI/PCBM/BPhen/Ag	12.75	N/A	18.01	5 wt % , wt % of PbI_2	N/A	N/A	double step spin coating, Urea and PbI_2 together form $PbI_2.O=C(NH_2)_2$ complex/intermediate, resulting big flat grains	[66]
Urea	ITO/SnO_2/ $CH_3NH_3PbI_3$ /Spiro/Ag	16.80	a) Retained 10 % PCE as of final PCE after ~27 days b) retained nearly 90 % PCE from initial after 60 mins	18.5	4 mol%	a) Remained 12 % PCE as of final PCE after ~27 days b) retained nearly 100 % PCE from initial after 60 mins	mppt tracking a) dark, ambient, b) 1 sun, in-situ	adduct formation, high crystallinity, good film, suppress non-radiative recombination and passivates grain boundaries.	[67]
formamide	FTO/ (c-TiO_2/ (mp-TiO_2)/ mesoporous / $CH_3NH_3PbI_3$ /ZrO_2 layer (mp-ZrO_2) / carbon electrode	14.26	N/A	15.21		N/A	N/A	The amide additives shifted the Fermi level of the $MAPbI_3$ perovskite from −4.36 eV to −4.63, −4.65, and −4.61 eV, respectively for 1. formamide, 2. Acetamide, and 3. urea and suppressed non-radiative recombination. Reduced iodide defects vacancy	[68]
acetamide				15.57		N/A	N/A		
urea				15.07		N/A	N/A		
Thiourea			N/A	16.2	0.5 vol%	N/A	N/A		
Biuret	FTO/TiO_2/ $CH_3NH_3PbI_3$/PCBM/Ag	18.26	maintains ~50%PCE after 12 days	21.16	2 mol%	preserves 94% of its initial efficiency after 12 day	85°C , N_2, inert, non-encapsulated ,	Increased grain size, reduced trap state, additive acts as Lewis base and interacted with uncoordinated Pb^{2+},	[69]

								improves the thermal stability	
benzoquinone (BQ)	ITO /PEDOT:PSS /$CH_3NH_3PbI_3$ / C60 /BCP/Au	10.7	Remained ~50% PCE from initial after 900 h	15.6	0.5 mol%	Remained ~80% PCE from initial after 1000 h	unencapsulated, 1 sun, open circuit, without uv-filter	reduces trap density	[70]
benzoquinone (BQ)	FTO/TiO_2/ $CH_3NH_3PbI_3$ /SpiroOMeTAD/Au	17.37	(a) Dead in 1200 h (b)Dead in ~800 h	18.01	**0**.25%	(a)Retained 75 % PCE from initial after 2400 h (b) Retained ~30 % PCE from initial after 1200 h	un-encapsulated, without uv-filter (a) RH (~20%, RT, (b) ambient air, RH (40%-70%, RT)	Improves crystal quality, passivate grain boundary, reduce trap states, suppress PbI_2 formation at GB	[71]
triazine perylene diimide (TPDI)	ITO/PEDOT:PSS/ $CH_3NH_3PbI_3$ /PC61BM /Ag	8.32	Retained 30% from initial PCE after 400h	10.84	1.2 mg/mL	Retained 60% from initial PCE after 400h	Non-encapsulated, ambient,	minimize grain boundary defects and enhance the coverage and crystal grain sizes	[72]
3,4-Dihydroxybenzhydrazide (DOBD)	ITO/PEDOT:PSS/ $CH_3NH_3PbI_3/C_{60}$ /BCP/Al	14.47	Retained 70%PCE from initial after 35 days	17.58	3 mg/mL	Retained 85%PCE from initial after 35 days	Non-encapsulated, inert, dark,	increases grain size and decrease of grain boundaries, both of which facilitate charge transportation and suppress charge recombination, due to Lewis acid-base interaction between Pb^{2+} and C=O	[73]
BMCl, benzamidine hydrochloride	(ITO/TiO_2/$PC_{61}BM$/ $CH_3NH_3PbI_3$/PTAA/MoO_3/Ag	17.8	N/A	18.4	N/A	N/A	N/A	enhance work function of perovskite film improving efficiency	[74]
Isatin-Cl	ITO/PTAA:F4TCNQ/ $CH_3NH_3PbI_3$/ PCBM/ Al	18.13	a) Retained 60 % PCE from initial after 350 h. b)Retained 30 % PCE from initial after 24 h	20.18	0.0001 wt%	a) Retained 95 % PCE from initial after 350 h. b)Retained 75 % PCE from initial after 24 h	un-encapsulated, a)in ambient air, RH=45% , room temperature, b) in nitrogen atmosphere at 85 ˚C temperature,	The carbonyl groups and hydrogen-bond structures on Isatin-Cl passivate the defect states in the perovskite grain boundaries and improve charge transport, suppress charge recombination, hydrophobic ring attached to Isatin-Cl improves stability against humidity.	[75]

polycaprolactone (PCL)	glass or PET/ITO/PEDOT:PSS/ $CH_3NH_3PbI_3$/PC61BM/BCP/Ag	10.52	Retained 32 % of initial PCE (10.12 %) after 300 bending cycles	14.49	0.025 wt%	Retained 90 % of initial PCE (10.12 %) after 300 bending cycle	mechanical bending stability	carbonyl (C=O) and Pb^{2+} bond helps the uniform coverage of perovskite, which avoids the defects and achieve the grain boundary regulation on flexible PSC	[76]
IDIS-Th	ITO/P3CT-N/ $CH_3NH_3PbI_3$/PC61BM/Bphen/Ag	17.78	(a)Retained 50% from initial PCE after 300h (b) Retained 78% from initial PCE after 200 h	20.1	0.05mg mL-1	(a)Retained 80% from initial PCE after 300 h (b) Retained 85% from initial PCE after 200 h	(a)100 mW cm^{-2}, ambient, RH=30%, non-encapsulated, (b) 85C, inert, dark,	Passivate grain boundary, reduce charge recombination, adduct between additive and under coordinated Pb ions can effectively inhibit ion migration and moisture diffusion to enhance the stability of PSC devices	[77]
IDIC-Th				18.78		(a)Retained 80% from initial PCE after 300 h (b) Retained 78% from initial PCE after 200 h			
NMP	FTO/TiO_2/PbI_2/MAI/Spiro-OMeTAD /Au	12.25	Died after 14 days	14.66	30% NMP in 1 ml precursor	N/A			[82]
DMSO				16.17	20% DMSO in 1 ml precursor	Retained 66 % PCE from initial after 14 days	in air	morphology control based on Lewis basicity based, Donor number and boiling point	
HMPA				12.06	5% HMPA	N/A			
tetramethylene sulfone (TMS)	FTO/bl-TiO_2/mp-TiO_2/ $CH_3NH_3PbI_3$/Spiro/Au	8.7	Retained ~70% from initial PCE after30 days	16.2	molar ratio =PbI_2 :MAI :TMS (2:2:1)	Retained 80% from initial PCE after30 days	RT, RH-10-40%, un encapsulated, dark	Intermediate phase via cross-linking. PbI_2 act as Lewis acid TMS with S=O group acts as Lewis base.	[83]
tetrahydrothiophene oxide (THTO),	ITO/PEDOT:PSS/ $CH_3NH_3PbI_3$/PCBM/A	N/A	N/A	12.1	the molar ratio of THTO to Pb (3:1 THTO: Pb)	N/A	N/A	additive alters the nucleation and growth processes, lowered the free energy of the precursor by incorporating a sulfoxide (S=O), which strongly interacts with $MAPbI_3$ precursors, allowing an unprecedented degree of control over the nucleation density and growth rate.	[84]

2.1.2.3 Carboxylic /acid additives

Besides, acids additives have also been incorporated in the $MAPbI_3$ precursor. The most commonly reported acid additive is 5-amino valeric acid (5-AVA). Dauskardt and co-workers showed that the introduction of 5-AVA into $MAPbI_3$ precursor could be helpful to increase the mechanical robustness of the perovskite film. To test the mechanical reliability double cantilever beam method was used, and the cohesion energy (Gc) was calculated from the critical load at which the film created cracks. It was observed that the incorporation of 5% concentration of 5-AVA into $MAPbI_3$ precursor increased cohesion energy (Gc) from 0.61 ± 0.27 J/m^2 (pristine) to 6.04± 2.04 J/m^2 (with AVA additive) almost by 12-fold. This improvement in Gc with 5-AVA was attributed to enhanced interaction forces due to the longer alkyl chains present in the 5-AVA [85]. Additionally, a further increase in plasticity and crack deflection around the additive-containing perovskite grain boundaries was observed. Later, the elastic moduli of $MAPbI_3$ perovskite films with 5-AVA showed a slight decrease in the elastic modulus from 20.5 GPa (pristine) to 18.9 GPa (5-AVA) (using the Nanoindentation method). This decrease in stiffness of the planar perovskite structure made it more mechanically robust and less brittle. Also, it was confirmed that adding 5 AVA in $MAPbI_3$ precursor does not change $MAPbI_3$ lattice parameters [85]. Simultaneously, another study done by Durrant and the group reported enhanced photostability of $MAPbI_3$ solar cells due to surface defect passivation in screen printed, HTM free, carbon electrode based PSC consisting of 5 AVA in $MAPbI_3$. They found a 40-fold increase in device lifetime measured under full sun illumination in ambient air (RH± 15%). Further, it was proposed that AVA is located at grain boundaries and thus able to passivate surface defect sites, resulting in enhanced resistivity to oxygen-induced degradation [86]. The impressive improvement in the stability due to AVA additive is attributed to the interaction of halides with –COOH and NH_3^+ group, through hydrogen bonding [(O-H----I) and (N-H----I)] and also been further verified in the large area cell with an area of 0.25 cm^2 that demonstrated the efficiency of 6.6% with a decent shelf life of 75 days, maintaining more than 90% of initial efficiency [87]. Later, using polyacrylic acid (PAA), Cao and workers also demonstrated that acid additives could be useful for large area (1 cm^2) films using the doctor blade method. Using the carboxyl functional groups of PAA, iodide ion vacancies at the perovskite crystal surface could be cross-linked. Thus the interaction of the PAA molecule with $MAPbI_3$ passivates defects and improves PCE and stability [88]. In addition, it was demonstrated

that bifacial passivation could also be obtained by the interaction of a functional group of -COOH, combined with -C,-S (of thioctic acid (TA)). Lewis acid-base reaction between under-coordinated Pb^{2+} and S atom in $MAPbI_3$ can passivate one side, and at the same time, TiO_2 can interact with COOH through hydrogen bonding, resulting in double-sided passivation [89]. Likewise, various studies reported that if multiple –COOH groups are attached with hydrophobic phenyl ring – it can chelate with Pb^{2+} atom and act as a shield against moisture and humidity under ambient conditions, maintaining the overall crystallinity of film. Terephthalic acid (TPA) and trimesic acid (TMA) are examples. The proposed mechanism of stability in such a case is given as follows: negatively charged groups ($–COO^–$) strongly attract Pb^{2+} ions in the precursor solution via electrostatic interactions. At the same time, the hydrogen atom from carboxylic acid can bond covalently with the halide anion in the solution due to the strong electronegativity of halide ions. Thus, it overall suppresses the loss of iodine molecules and, in turn, slows down the decomposition of $MAPbI_3$ light absorbing layer. Simultaneously, benzene ring with rigidity and π-π bond effect does not allow to interact with water and protects against thermal stress and UV-illumination in ambient conditions [90,91]. Similar effects were observed when 3,30,5,50 -azobenzene-tetracarboxylic acid (H4abtc) containing two benzene rings connected via azo bonding is introduced in PbI_2 precursor in optimum amount (2 mass %). Although the purpose of using the azo group was to reduce the stiffness of the perovskite film [92], due to the hydrophobic nature of attached cation in the acid-containing additive**,** most of them also increase ambient stability. Further details of acid-based additives in $MAPbI_3$ are provided in Table 3 below. The chemical structures of acid additives are shown in Figure A0.5, Appendix 0.

Table 3 A summary of acid additives for $MAPbI_3$ active layer.[58]

Additive in active layer	architecture	PCE, % (Pristine)	Stability (Pristine)	PCE, % (with additive)	amount of additive	Stability with additive	Stability conditions	Role of additive	Ref
5-aminovaleric acid (5-AVA)	ITO/ C_{60}/ $CH_3NH_3PbI_3$ /PTAA /Au	15.4	N/A	13.7	5% wt	N/A	N/A	Larger grain size, improved crystallinity, improved mechanical robustness	85
amino valeric acid AVA	FTO/compact TiO_2/mesoporous TiO_2/mesoporous ZrO_2/mesoporous carbon	11.1	Died in 110 h	9.1	3% molar ratio of AVA: MAI	Retained 50 % PCE from initial after 110 h	RH =15%, 1 Sun, non-encapsulated,	AVA located at grain boundaries is able to passivate surface defect sites, resulting in enhanced resistivity to oxygen-induced degradation.	86
5-ammonium valeric acid iodide (5-AVAI)	FTO/TiO_2/ $CH_3NH_3PbI_3$/ ZrO_2/Carbon	N/A	N/A	6.68	0.072M of AVAI	5.62 % PCE as of final PCE after 75 days	Ambient,	Big area 0.25cm^2, lower charge transport resistance	87
aminovaleric acid iodide (AVA)	TiO_2 /ZrO_2/ $CH_3NH_3PbI_3$/Spiro/Au	~7	N/A	~9	AVA:PbI_2= 3 mol%	N/A	N/A	Controls ion migration-	93
Poly(acrylic acid) PAA	FTO/ NiOx:Zn/ $CH_3NH_3PbI_3$/ ($PC_{61}BM$)/bathocuproine (BCP)/Ag	10.3	Retained 60% from initial PCE after 24 days	14.9	5 mg/mL	Retained 80% from initial PCE after 24 days	RT, air, ambient,RH~30 ±5%, non-encapsulated,	Using the doctor blade method, a smooth, uniform, and pin-hole free film of high electronic quality, passivate defects, large area devices (1cm^2)	88
aminopropanoic acid (APPA)	ITO/PTAA/$CH_3NH_3PbI_3$/ $PC_{61}BM$/BCP/Ag,	17.51	6% as of PCE after 90 days	19.23	weight ratio of MAI:APPA= 0.56	13% as of PCE after90 days	Un-encapsulated, RH-10%,	Smaller grain size, smooth surface, suppress non-radiative charge recombination, resulting in enhanced J_{SC} and V_{OC}	94
thioctic acid (TA)	FTO)/compact TiO_2 (c-TiO_2)/TiO_2-Poly(TA)/ $CH_3NH_3PbI_3$/Spiro-OMeTAD/Au	17.4	a) Died after 180 mins b) a) Died after 400 h c) n/a	20.4	20 mg/ml	a) retains 98% of its original PCE after 450 min b) 97 % PCE after 2100 h c)retained 92 % PCE from initial after 600 h	a) under UV irradiation time (35.8 mW cm^{-2}). b) air (50 ± 10 RH%), light/dark-n/a, temp-n/a, c)mppt-yes, inert,1.5 AMG	carboxylic acid moieties Binds TiO_2 surface Then five-membered ring-containing the dynamic covalent disulfide is bonded to the other end of the molecule through the thermal-initiated ring-opening and interacts with Pb , forming high-quality perovskite film due to the Lewis acid-base reaction between S and Pb^{2+}. Extra passivation on TiO_2 helps for efficient charge extraction and stability under UV illumination and ambient conditions	89

terephthalic acid (TPA)	FTO/compact-TiO_2/ $CH_3NH_3PbI_3$ /Carbon layer	11.5 ±0.67	a)retained 81% PCE from initial after 21 days b) ~6 % PCE as of final PCE after 700 h c)retained 79% PCE from initial after 40 mins	14. 29 ± 0	8 mg/mL	a)retained 94% PCE from initial after 21 days b) 10.7 % PCE as of final PCE after 700 h c)retained 90% PCE from initial after 40 mins	a) un-encapsulated, air, RH= 35%, 25˚C, ambient , dark, b)60˚C c) 365 nm UV illumination with an intensity of 250 mW cm^{-2} (equivalent to 56 suns equivalent of UV light below 400 nm in wavelength	($–COO^–$) from TPA can strongly attract Pb^{2+} ions crosslinking additive within perovskite, resulting in compact, dense improved morphology., the rigidity of the phenyl skeleton allows moisture and thermal resistance	90
trimesic acid (TMA)	FTO/TiO_2/$CH_3NH_3PbI_3$/ Spiro-OMeTAD /Ag	14.27	(a)retained 49% from initial PCE after 10h (b)retained 46% from initial PCE after 20 days	17.21	1.0 mol L^{-1} PbI_2 precursor solution	(a)retained 49% from initial PCE after 10 h (b)retained 71% from initial PCE after 20 days	(a) 100C, air, ambient, dark, non-encapsulated, (b)RT, air, Rh~30%, dark, non-encapsulated,	maintains stability, (TMA with a benzene ring and three carboxyl groups). The strong hydrogen bond between the hydroxyl group and iodide to suppress the loss of iodide ion, preventing the perovskite from decomposing. Moreover, the benzene ring with rigidity and the π-π bond effect, and the hydrophobic alkyl chains further protects the perovskite from reacting with water	91
3,3',5,5'-azobenzene-tetracarboxylic acid (H(4)abtc)	FTO/TiO_2/ $CH_3NH_3PbI_3$ /Spiro/Au	14.25	a)remained nd 25% after 20 h b) e retained 66% of its initial PCE after 30 d	17.67	2.0% (mass ratio with respect to PbI_2	a)remained 61% after 20 h b) retained 84% of its initial PCE after 30 d	a)100˚C without encapsulation in air 100 mW cm^{-2} (AM 1.5), b) RT, RH=30%without encapsulation.	High-quality perovskite film, H4abtc can passivate grain boundaries by reacting with the lead cation, therefore leading to good thermal stability and anti-moisture of perovskite films due to rigidity of the benzene ring and azo bond	92
4-methylbenzene sulfonic acid (4-MSA)	FTO/bl-TiO_2/mp-TiO_2/ $CH_3NH_3PbI_3$ /Spiro-OMeTAD/Au.	14.05	N/A	17.58	6 mg/mL	N/A	N/A	Improved performance, reduced hysterias, improve J-V characteristics, the sulfonic group is chemically bonded to mp-TiO_2 and phenyl backbone has p-conjugated structure. Jsc and V_{oc} of 4-MSA doped PSC are enhanced.	95

2.1.2.4 Carboxylate/acetate additives

In a similar fashion, the acetates in the form of additives also show improvement in crystallinity and grain size, passivating the grain boundaries. One of the examples is formamidine acetate salt (FAAc). It is reported that FAAc controls the film morphology of $MAPbI_3$ film and improves fill-factor over 80%, improving PCE to 16.59%. The improved photovoltaic parameter was further associated with incorporating FAAc that eliminated the defect and trap density in the $MAPbI_3$ film and thus improved the charge transport efficiency and reduced the hysteresis [96]. On the contrary, methyl ammonium acetate (MAAc) resulted in lower crystallinity and a smaller grain size ~200 nm [97]. However, it was suggested to use MAAc together with thiosemicarbazide (TSC) salt in the precursor to overcome lower crystallinity. This combination of additives (10–15% MAAc (molar ratio) and a tiny amount of TSC (3–5% molar ratio) gave a certified PCE of 19.19% for an aperture area of 1.025 cm^2, and the high-performing devices were able to sustain over 80% of the initial PCE after 500 h of thermal ageing at 85°C [98]. Besides, acetate additives were also reported to be used as complementary to halogens. For instance, ammonium acetate (NH_4Ac) was found to produce full film coverage with higher crystallinity. It was speculated that NH_4Ac resulted in the formation of methylamine acetate salt by forming NH_4PbI_3 as an intermediate phase with a volatile by-product NH_3 resulting in a higher nucleation density of grains and full coverage of the surface. This, in turn, resulted in higher efficiency of 13.9% in carbon-based solar cells (FTO/TiO_2/perovskite/Carbon) and 17.02% in the two-step spin coating in FTO/TiO_2/$CH_3NH_3PbI_3$/spiro-OMeTAD/Au configuration [99,100]. Further, the influence of NH_4Ac addition was compared with NaAc and $ZnAc_2$. Unfortunately, the incorporation of sodium acetate (NaAc) into the $MAPbI_3$ precursor reported no improvement in photovoltaic performance. However, the PCEs were comparable. While compared to Zinc-acetate ($ZnAc_2$) additive, (devices with $ZnAc_2$) demonstrated improved fill factor and short circuit current density over reference cells, resulting in improved PCE from 11.1% to 12.30%. Furthermore, against the speculation that Zn^{2+} might partially replace Pb^{2+}due to the smaller ionic radius, the small quantity of $ZnAc_2$ (MAI/PbI_2/$ZnAc_2$ (1:1-x:x, x= 7%) was reported to assimilate well within $MAPbI_3$ framework and maintained ~89% of initial PCE after 1900 h when stored in RH=40%, dark. However, NH_4Ac incorporated devices exhibited ~96% PCE of the initial stage after1900 h with the same conditions [99,100]. Later on, lead acetate ($PbAc_2$) was employed as an

additive and demonstrated an excellent PCE improvement from 17.25% to 19.07%. It was further demonstrated that incorporating $PbAc_2$ in precursor creates an intermediate phase by forming a hydrogen bond due to the interaction between hydrogen from MA^+ and O from acetate. Thus, this hydrogen bonding acts as a crosslinking agent for the intermediate phase, which later causes improvement in intrinsic stability of devices that maintained almost 95% of initial PCE till 20 days [101]. A similar mechanism was utilized in another study where the addition of barium acetate ($BaAc_2$) has been explored in $MAPbI_3$ perovskite with a lower concentration of (0-2mg /mL), which suppressed ion migration and improved thermal stability. The devices could sustain ~90% PCE of the initial stage after exposure to thermal stress at 90˚C in the dark in inert conditions without any encapsulation up to 400 h [102]. Thus, by employing acetate-based additives, improved stability can be obtained both in ambient and inert conditions. Most of the acetate-based additives are summarized in Table 4, as shown below, and their respective chemical structures are presented in Figure A0.6, Appendix 0

Table 4 Acetate based additives in $MAPbI_3$ active layer.[58]

Additive in active layer	architecture	PCE, % (Pristine)	Stability (Pristine)	PCE, % (with additive)	amount of additive	Stability with additive	Stability conditions	Role of additive	Ref
formamidine acetate salt (FAAc)	ITO/PEDOT:PSS/ $CH_3NH_3PbI_3$ /PCBM/Al	12.13	(a)n/a (b)n/a	16.59	5 mol%	(a) Retained 90 % PCE from initial after 30 days (b)16.10 as of final PCE after 320 s @ (0.87 V)	inert, un-encapsulated,	control film morphology and crystallinity, improves optical and electrical properties reduces hysteresis	96
methylammonium acetate (MAAc) and thio-semicarbazide (TSC), combined	FTO/NiO/ $CH_3NH_3PbI_3$/PCBM/Ag	N/A	N/A	19.19	10–15% MAAc (molar ratio) 3–5% TSC (molar ratio)	a)Retained 90% PCE from initial after 1000 h b) Retained 80% PCE from initial after 500 h	a) AM 1.5 light soaking (short-circuit, temperature of ≈25 °C and RH < 25%), mppt b)dark, 85˚C, RH < 25%	large-area (aperture area of 1.025 cm^2 using one step solution process, high crystalline quality of film	98
ammonium acetate (NH_4Ac,)	FTO/TiO_2/$CH_3NH_3PbI_3$/spiro-OMeTAD/Au	13.82	N/A	17.02	10 wt%	N/A	N/A	Improved film morphology and increased surface coverage	99
ammonium acetate CH_3COONH_4 (NH_4Ac)	FTO/TiO_2/ $CH_3NH_3PbI_3$/carbon devices	11.11	Remained 60% from initial PCE after 1900h	13.9	MAI/PbI_2/NH_4Ac (1:1:x=0.08%)	Remained 96% from initial PCE after 1900h	Dark, RH=40%,	Carbon electrode-based device, improved crystallinity	100
$Zn(CH_3COO)_2$ ($ZnAc_2$)				12.30	MAI/ PbI_2/$ZnAc_2$ (1:1-x:x= 7%,)	Remained 89% from initial PCE after 1900h			
Lead acetate ($PbAc_2$)	Glass/ ITO/PTAA/ $CH_3NH_3PbI_3$ /PCBM/BCP/Ag	17.25	Retained 80% PCE from initial after 20 days	19.07	3% $PbAc_2$ (molar ratio with respect to PbI_2)	Retained 95% PCE from initial after 20 days	un-encapsulated, inert,	PbAc2 additive aids cross-linking to form a strong hydrogen bond with MAI, leading to a more stable perovskite intermediate phase, retards crystallization process, resulting, perovskite thin films with better morphology and larger grains	101

barium acetate ($BaAc_2$)	ITO/P3CTN/ $CH_3NH_3PbI_3$/$PC_{61}BM$/C_{60}/BCP /Ag	18.99	Retained only 20% from initial PCE after 400 h	19.82	2 mg/mL	Retained 90 % from initial PCE after 400 hours	Non encapsulated, inert,90 °C, dark,	suppression of ions migration, high quality perovskite film, grain boundary passivation	[102]

2.1.2.5 Ester and ether based additives

Interestingly, phenyl-C61-butyric acid methyl ester (PCBM), which is commonly employed as a charge transport layer in organic-inorganic hybrid solar cells, has also been examined as an additive in the perovskite layer to achieve hole transport material (HTM) free fully printable MPSC (mesoporous perovskite solar cell). It was shown that when the concentration of PCBM increased in the active layer from 0 to 0.25 mg/mL, the PCE significantly improved from 8.58% to 12.36%, achieving a PCE enhancement of more than 44%. This enhancement of PCE was further ascribed to increased J_{sc} from 14.56 mA cm^{-2} to 20.26 mA cm^{-2} due to higher photo-generated charge separation and suppressed the charge recombination process. Later, it was illustrated that the PCBM-perovskite intermediate phase is facilitated due to the formation of an intermediate adduct with PbI_2 and carbonyl groups in PCBM [103]. Afterwards, Hu et al. compared PCBM incorporation with only C_{60} unit and C_{60}-Taurine unit in single-step spinning coating method in p-i-n configuration. It was reported that C_{60} (16.59%), PCBM (15.94%), C_{60}-Ta (16.59%) all improved PCE over pristine (14.87%), which was consistent with the previously published report. Further, it was found that the addition of C_{60} and its derivatives decreased the trap densities and exhibited higher stability when exposed to ambient conditions RH=25-50% without encapsulation [104].

Likewise, investigations have shown that ethers can help passivate grain boundaries on the perovskite surface boundary. Poly (propylene glycol) bis (2-aminopropyl ether) (PEA) and Jeffamine are some of the examples that showed interaction with Pb ions due to lone pair of electrons on the oxygen-containing ether part of the additives. Simultaneously, the MA^+ cation from perovskite forms hydrogen bonding with the counter ion of additive. Thus the polymer works as a cross-linking agent that decreases trap densities and hysteresis, improving the device performance and stability. To add on, the cross-linking properties can also improve the ductility of perovskite film while stretching when fabricated on a flexible substrate (such as D2000, Jeffamine variation) [105,106]. Furthermore, using the mechanism above, ethyl cellulose (EC), a low cost, environmentally friendly, thermally stable and water-insoluble compound, also demonstrated chemical passivation of defect traps. Thus, because of the passivation effect of EC additive, the $MAPbI_3$ crystal structure remained stable against moisture and air, maintaining 80 % of PCE when exposed un-encapsulated to ambient air at RH=45% in the dark for 30 days [107]. Later on**,** tetraorthosilicate (TEOS) additive in $MAPbI_3$ was also reported to

lower the cost of processing by making the fabrication process feasible in the air instead of the glove box, which was found to be valid both for single and double steps. This achievement was due to the fact that when TEOS is introduced to $MAPbI_3$ in air, SiO_2 precipitates at the surface, acting as a passivation for the perovskite surface and shielding it from moisture and air. This improved the overall stability in ambient conditions [108–110]. Further, cyclic ether compound THF (Tetrahydrofuran) was also reported to improve stability in ambient air, which the pioneer of PSCs Miyasaka group investigated. The study demonstrated that THF and PbI_2 in DMF interact and form complex, resulting in dense, homogenous and pinhole-free film due to complex formation between Pb and O donor from THF because of the Lewis acid nature of Pb and Lewis basicity of THF. This, in turn, avoids a direct interaction of PbI_2 with water, improving T80 (T80 is the time after which PSC remain 80% of initial efficiency) for 20 days in the ambient environment with 50% RH when devices were exposed un-encapsulated [111]. Further, a table describing ester and ether containing additives and their role in the $MAPbI_3$ layer is presented in Table 5. The chemical structures of ester and ether containing additives discussed above are presented in Figure A0.7, Appendix 0.

Table 5 Ester and Ether based additives for $MAPbI_3$ and their role.[58]

Additive in active layer	architecture	PCE, % (Pristine)	Stability (Pristine)	PCE, % (with additive)	amount of additive	Stability with additive	Stability conditions	Role of additive	Ref
[6,6]-phenyl-C_{61}-butyric acid methyl ester	FTO/c-TiO_2/m-TiO_2/mZrO_2/ $CH_3NH_3PbI_3$/m-carbon	8.58	N/A	12.36	0.25 mg mL-1	N/A	N/A	Improved morphology, intermediate formation between C=O of PCBM and PbI_2	[103]
PCBM	Glass/ITO/ $CH_3NH_3PbI_3$ /PCBM/BPhen/Ag	13.94	Retained ~9% (absolute value) as of final PCE after 10 days	15.94	3.5 mg/mL	Retained ~12% (absolute value) as of final PCE after 10 days	without encapsulation, ambient RH= 25-50% ,	improves crystallinity, passivates defects, suppress non radiative recombination	[104]
C_{60} -Ta				16.46	1.5 mg/ mL	Retained ~12% (absolute value) as of final PCE after 10 days			
C_{60}				16.59	0.1 mg/mL	Retained ~11% (absolute value) as of final PCE after 10 days			
Poly(propylene glycol) bis(2-aminopropyl ether) (PEA)	FTO/c-TiO_2/mp-TiO_2/ $CH_3NH_3PbI_3$/Spiro/Au	17.18	maintains ~55% of its original PCE after 30 days	18.87	1 wt%	maintains 95% of its original PCE after 30 days	dark, ambient air with 30±5% relative humidity,	Grain boundary passivation, the oxygen atom from ether in PEA, acts as a crosslinking agent, reduces trap density and hysteresis.	[105]
Jeffamine	ITO/NiO_x/$CH_3NH_3PbI_3$ /$PC_{61}BM$/BCP/Ag	14.5	Showed major cracks	16.8	0.05 wt%	Retained original morphology	10 cycles of stretching at 30% strain	Defect passivation through lewis acid-base reaction of N atom and O atom with Pb^{2+} / or interaction of MA^+ and hydrogen bond of jeffamine decrease trap density, enhances the ductility of the perovskite film to prevent cracking during stretching.	[106]
ethyl cellulose (EC)	FTO/c-TiO_2/ $CH_3NH_3PbI_3$/Spiro-OMeTAD/ MoO_3/Ag	17.11	Completely died in 30 days	19.27	0.1 mg/mL	Retained 80% PCE from initial after 30 days	Non – encapsulated, dark, Ambient, air, RH=45%,	Hydrogen bonding between EC and MAI passivates defects at the grain boundary, reduces hysteresis and improves stability	[107]

tetraethyl orthosilicate (TEOS)	TiO_2/ $CH_3NH_3PbI_3$/Spiro-OMeTAD/Ag	15.96	Retained 73% of its initial PCE after 28 days	18.38	0.3 mol%	Retained 77% of its initial PCE after 28 days	Ambient , 25˚C, RH=30%, non-encapsulated,	Reduce trap density, improves carrier lifetime	[108]
THF	FTO/TiO_2/ $CH_3NH_3PbI_3$/ Spiro-OMeTAD / Au	11.3	Retained 35 % PCE from initial after 20 days	15.1	THF: DMF(1:10) v/v	Retained 80% from initial PCE after 20 days	RH 50% , un-encapsulated,	Complex formation due to lewis acid-base reaction	[111]
Diethyl ether	Glass/ITO/NiOx/ $CH_3NH_3PbI_3$/PCBM/BCP/ Ag	13.28	N/A	15.09	the molar ratio of 4% with matrix solvent	N/A	N/A	Grain size improvement	[112]

2.1.2.6 Hydroxyl/alcohol additives

The Hydroxyl group can also play a vital part in interacting with perovskite through hydrogen bonding, further improving crystallinity and performance. For example, enhanced PCE and stability was observed when dibutyl hydroxyl toluene (BHT) additive containing a phenol group was mixed in $MAPbI_3$ precursor [113]. Furthermore, methanol and isopropanol showed larger grain size, reduced grain boundaries, lessened defect density and demonstrated efficient charge carrier extraction at the interfaces leading to improved PCE stability in ambient conditions without encapsulation. Similarly, improvement in PCE was also noticed due to other hydroxyl based additives such as 2-methoxy ethanol (ME), 2-ethoxyethanol (EE), and 2-propoxy ethanol (PE) and n butanol [114–116]. A summary of alcohol-based additives and their influence on the PCE and role with the perovskite framework is described in Table 6, and their respective chemical structures are shown in Figure A0.8, Appendix 0.

Table 6 Alcohol based additives and their role in $MAPbI_3$ perovskite framework.[58]

Additive in active layer	architecture	PCE, % (Pristine)	Stability (Pristine)	PCE, % (with additive)	amount of additive	Stability with additive	Stability conditions	Role of additive	Ref
dibutylhydroxytoluene (BHT)	ITO/ PEDOT: PSS/ $CH_3NH_3PbI_3$/ $PC_{61}BM$/ZnO/Al	17.1	Retained 85% from initial PCE after 180 min	18.1	0.02 M	Retained 93% of initial PCE after 180 min	100 mW cm^{-2} , RT, non-encapsulated, RH<5%	intermolecular hydrogen bonds between the MA^+ and −OH groups of the BHT Additive improves film crystallinity, reducing the sub-Eg states and carrier traps,	113
methanol	FTO/TiO_2/ $CH_3NH_3PbI_3$/ Spiro-OMeTAD /Au	16.53	Retained 40% from initial PCE after 30 days	19.51	5 vol%	Retained 90% from initial PCE after 30 days	Dark, ambient, nonencapsulated,	morphology control/enhancement	114
2-methoxyethanol ME	ITO/ZnO/ $CH_3NH_3PbI_3$ /Spiro-OMeTAD/MoOx/Ag	14.2	N/A	16.7	30µl to 1 ml MAI solution	N/A	N/A	two-step interdiffusion protocol to prepare pin-hole free perovskite films, glycol ethers changes the lead iodide to perovskite conversion dynamics and enhances PCE resulting in more compact polycrystalline films, and it creates micrometer-sized perovskite crystals vertically-aligned across the photoactive layer	116
2-ethoxyethanol (EE),				13.2					
2-propoxyethanol (PE)				15.1					
isopropanol (IPA)	FTO/compact-TiO_2/ $CH_3NH_3PbI_3$ /Spiro-OMeTAD/Au	16.02	Retained 40 % PCE from initial after 40 days	19.70	precursor: IPA volume ratio = 4:1	Retained 85 % PCE from initial after 40 days	un-encapsulated, air, ambient , RT, dark/light-n/a, mppt-n/a, uv-filter-n/a,	morphology enhancement/control	115

n-butanol	FTO/CT-IO_2/mp-TiO_2/ $CH_3NH_3PbI_3$/Spiro-OMeTAD /Ag	13.8	N/A	15.5	5.0 v% for 1 ml precursor	N/A	N/A	morphology enhancment	[117]

2.1.2.7 Oxygen based multifunctional group containing additives

Other than these additives, other oxygen atom-based additives with multiple functional groups consisting of C=O, COOH and OH are also employed in the $MAPbI_3$ precursor. One example is reduced graphene oxide (rGO), which was used to achieve fast electron transport rates toward the anode and the growth of large, uniform, smooth and crystalline perovskite film, resulting in a massive improvement in device performance from 13.6% to 20% [118]. Another example includes Poly (amic acid) (PAA) and polyimide (PI) additive. However, the PAA and PI additives also consisted of N atoms, other than C=O, COOH and OH functional group. The O atoms in PAA and PI form hydrogen bonds with H atoms in $CH_3NH_3^+$. The lone pair of electrons of N atoms interact with Pb ions, which stabilized the PVSK framework. Furthermore, these interactions improved the optoelectronic properties of the perovskite layer. As a result, an increment in the grain size was observed when 0.0497 mg/mL PAA-derived perovskite was employed, illustrating the Lewis acid−base interaction between C=O and Pb^{2+} that controls the crystallization process and defects passivation of PVSK. Besides, both PAA and PI are hydrophobic and highly heat-resistant polymers and further contribute to the stability of PSC when operated in a humid and high-temperature environment [119]. Table 7 presents the details of these additives. Figure A0.9, Appendix 0 presents the chemical structures of such additives.

An overall comparison of stabilizing effect of additives of different functional groups associated with O donor atom has been shown in Figure A0.10, Appendix 0.

Table 7 Other oxygen atom-based additives with multifunctional group.[58]

Additive in active layer	architecture	PCE, % (Pristine)	Stability (Pristine)	PCE, % (with additive)	amount of additive	Stability with additive	Stability conditions	Role of additive	Ref
Reduced graphene oxide (rGO)	FTO/TiO_2/ $CH_3NH_3PbI_3$/Spiro/Ag	13.8	retained 20% of their initial PCE after 50 days	16.5	9 μg mL^{-1}	retained 40% of their initial PCE after 50 days	dark, RH=10%, un-encapsulated,	defect-free perovskite films of enhanced crystallinity, larger and evenly distributed grains, enhanced light harvesting potential, increasing the photocurrent density and the resulting improved PCE	[118]
Poly(amic acid) (PAA)	ITO/NiO_x/ $CH_3NH_3PbI_3$ /$PC_{61}BM$/BCP/Ag	14.16	(a)Remained 13% as of final PCE after 500 h (b) Retained 50% from initial PCE after 70h	17.85	0.0497 mg/ml	(a)Remained 16.57% as of final PCE after 500 h (b) Retained 88% from initial PCE after 70h	Inert, dark, non-encapsulated, (b) 85˚C, RH=45% without encapsulation, dark, in the glovebox	The O atoms in PAA and PI form hydrogen bonds with H atoms in $CH_3NH_3^+$ and lone pair of electrons of N atoms interact with Pb ions, which stabilized the PVSK framework. Furthermore, these interactions improve the optoelectronic properties of the perovskites resulting	[119]
polyimide (PI)				16.49	0.0990 mg/ml	N/A	N/A		

2.1.3 S donor atom-based additives

2.1.3.1 Sulphide and organosulphur additives

Further, sulphur-based donor atoms have also improved crystallinity and device performance [27]. For instance, Yang and co-workers used dimethyl sulphide (DS) additive in $MAPbI_3$ precursor solution (based on DMSO precursor) and demonstrated a record high PCE of~ 18.4% for a flexible perovskite solar cell. Also, the formation of a stable intermediate complex between PbI_2 and DS molecule was observed that further enhanced stability. The enhancement of stability due to DS solvent additive was ascribed to the smaller electronegativity of the sulphur atom (2.5) in DS molecule compared to an oxygen atom (3.5) in DMSO molecule, which allowed sulphur molecules to provide electronins to empty 5d Pb orbitals, ultimately resulting in a hexa-coordinated complex formation. Therefore, with better crystallization and stable intermediate formation, 86% of initial PCE remained for 60 days when un-encapsulated devices were exposed to moisture RH~35% in the dark at room temperature [120]. Thiourea is another example of such an organosulphur compound, the addition of which into the photo-active layer results in improved performance and stability due to intermediate formation because of Lewis acid-base reaction. However, the addition of thiourea in the active layer is often compared to similar compound urea where O atom from carbonyl group (in urea) is replaced with S atom for thiourea. (the carbon atom is connected to different species). Both thiourea and urea have been found to show similar effects of increasing grain size, crystallinity, grain boundary passivation and coordination with PbI_2 in the $MAPbI_3$ framework [121]. Besides, many other organosulphur derivatives have been reported to form an adduct with PbI_2 as the Pb atom acts as Lewis acid. One such example is a volatile Lewis base, thioacetamide (CH_3CSNH_2), abbreviated as TAA [122].Another example is 2-pyridylthiourea, which has an S donor from thiourea, with a better ability to coordinate with PbI_2, and N donor from pyridine, which can co-ordinate with PbI_2 as a Lewis acid-base and regulate the co-ordination strength with PbI_2. This, further results in an improvement in crystallinity, which in turn resulted in better light-harvesting ability, charge transport, the reduction of defect and recombination loss leading to PCE of 18.2 %. In addition, this allowed retaining the stability of PSC more than 90% when exposed to ambient conditions, at room temperature or at higher temperature in the dark [61]. Recently, Zhang and his co-worker combined thiourea with water and Iodine (ITU) ions to reduce iodine defect vacancy produced during the film fabrication process. Afterwards,

the grain size was found to be increased with ITU (3.4 um) compared to when thiourea is added (800- 2000 nm), reducing the defects at grain boundaries. Besides, PSCs with ITU additives displayed a higher V_{oc}, longer decay time and longer carrier lifetime with a lower charge recombination rate. Thus overall, the addition of ITU resulted in improvement in PCE from 17.75% to 20.3%. In addition, the trap densities of the perovskite film significantly reduced as the ITU additive was incorporated into PSC, allowing PSC to stabilize and maintain ~80 of initial PCE after 100 h of exposure to 1.5AMG solar irradiation and 30 days in the ambient atmosphere [123].

2.1.3.2 Thiocyanates

Above and beyond, thiocyanates (SCN^- containing anions) additives are another subcategory for S atom-based additives. It should be noted here that thiocyanates are also considered pseudo halides. However, the role of thiocyanates in the perovskite film is very controversial. For example, Yanfa Yan and group demonstrated that a small amount (5%) of $Pb(SCN)_2$ addition in the precursor can significantly increase the grain size and crystalline quality of perovskite thin films using a one-step solution process method. This increased the average PCE from 15.57 to 17.80%. It was proposed that SCN^- anions do not incorporate in the perovskite film. SCN^- react with $CH_3NH_3^+$ and form volatile products HSCN and CH_3NH_2. This allows excess Pb^{2+} and I^- to form PbI_2 at grain boundaries that sources passivation effect [124]. On the contrary, Kim et al. demonstrated that $Pb(SCN)_2$ in $CH_3NH_3PbI_3$ partially substitute I anions and forms $CH_3NH_3Pb(SCN)_xI_{3-x}$ at lower temperatures. This phenomenon was observed not dependent on the concentration of $Pb(SCN)_2$. However, similar reports of enhancement of crystal size were found. Thus, it was concluded that the influence of processing temperature could affect the purity of the final perovskite film when $Pb(SCN)_2$ additive is used with $MAPbI_3$ [125]. Whereas, the addition of potassium thiocyanate (KSCN) also reported to form volatile products HSCN and CH_3NH_2, consistent with earlier mentioned results, with no traces of SCN^- found in the final perovskite film [124]. In the case of the KSCN additive, however, the residue was KI instead of PbI_2. Nevertheless, the authors illustrated that the final product upon KSCN incorporation was $MAPbI_3$, not $KPbI_3$, due to the smaller radius of K cation. In addition, KI residue improves the crystal quality of perovskite film, resulting in enhancement of charge transport, reduced carrier recombination and eliminating hysteresis [126].

Conversely, when NH_4SCN is incorporated in $MAPbI_3$, it was reported to form an unstable intermediate phase $NH_4PbI_{3-x}SCN_x$ due to lower formation enthalpy ($\triangle Hf$) of the NH_4PbI_3 over $MAPbI_3$, which later resulted in $CH_3NH_3PbI_{3-x}SCN_x$, a mixed halide perovskite after annealing of the films [127]. Therefore, when methylammonium thiocyanate (MASCN) was introduced as an additive to the precursor, a rapid vacuum-based drying approach was used to extract volatile intermediate products. So that, $MAPbI_3$ is formed as the final product with no traces of SCN^-. The films fabricated using this fabrication technique was reported to gain grain size of more than one micrometres with uniform surface morphology, resulting in high crystallinity and significantly large carrier lifetimes ($\tau1 = 931.94 \pm 89.43$ ns; $\tau2 = 320.41 \pm 43.69$ ns), Improving the ambient stability up to 1000 h [128]. However, when a larger cation Guadinium (Gu), is directly added in $MAPbI_3$ as GuSCN, $GuPbI_3$ was formed as an intermediate phase present with $MAPbI_3$ phase. It was contradictory to the earlier belief and reports, which showed that Gu single-handedly could not form three dimensional perovskite materials due to a larger ionic size (278 pm) over MA cation (217 pm). As a result, improved crystallinity, grain size and reduced trap density were noticed further, resulting in improved PCE (from 15.57% to 16.70%) that maintained stability ~90 % of the initial value after being stored for 15 days without encapsulation [129]. On the other hand, when guanidinium isothiocyanate is added in PbI_2 precursor, with dual step fabrication method; mixed cation perovskite was formed $(GU)_x(MA)_{(1-x)}PbI_3$ [130]. Nevertheless, most S donor atom-based additives are found to influence ambient stability. See Figure A0.11 and Figure A0.12, Appendix 0. At a glance summary of additives containing S atom and their role in the $MAPbI_3$ framework has been presented in Table 8.

Table 8 S atom based additive in $MAPbI_3$.[58]

Additive in active layer	architecture	PCE, % (Pristine)	Stability (Pristine)	PCE, % (with additive)	amount of additive	Stability with additive	Stability conditions	Role of additive	Ref
DS	MgF_2/PET/ITO/Nb_2O_5/ $CH_3NH_3PbI_3$/Spiro-OMeTAD /Au	17.03	(a)Retained 50% PCE from initial after 60 days (b) n/a	18.40	10 vol% in 1 ml precursor	(a)Retained 86% PCE from initial after 60 days (b)15.24 (83% of initial) as of final PCE after 5000 cycles	(a)Un-encapsulated, RH=35%, dark, RT (b) bending stability- bending radius of 4 mm	Intermediate between Pb^{2+} and S atom	[120]
Thiourea	ITO/ PEDOT:PSS/ $CH_3NH_3PbI_3$ /PCBM/Ag	13.4	N/A	16.2	0.5 vol%	N/A	N/A	Urea and thiourea both promote grain growth, reduce trap states, passivate grain boundaries.	[121]
thioacetamide (TAA),	ITO/SnO_2/ $CH_3NH_3PbI_3$ /Spiro-OMeTAD/Au	17	retains ~75.1% of its initial performance after aging 816 h	18.9	1.0% (molar ratio to PbI_2)	retains 88.9% of its initial performance after aging 816 h	RH=25-35%, unsealed , air,	Interaction of of TAA with Pb^{2+} , improved grain size	[122]
2-pyridylthiourea	FTO/C-TiO_2/mp-TiO_2/ $CH_3NH_3PbI_3$/ Spiro-OMeTAD Spiro/Au	15.5	a)Retained only ~10 % PCE from initial after 30 days b)Retained~55 % PCE from initial after 30 days	18.2	0.5 mg mL-1	a)Retained~95 % PCE from initial after 30 days b)Retained~92 % PCE from initial after 30 days	ambient, air, dark a)RH= 55±5 %, dark, RT b) 65 ˚C, RH=30%,dark,	N-donor and S-donor coordinate with PbI_2 and slow down the formation of PbI_2. improved morphology, larger crystalline size, smooth compact, homogeneous film	[61]
ITU for I− and thiourea	ITO/SnO_2 / $CH_3NH_3PbI_3$/Spiro-OMeTAD/Au	17.75	retain 30% of the initial PCE after 100 h	20.3	0.003 mM	retain 80% of the initial PCE after 100 h	AM 1.5 light soaking. in ambient atmosphere	Reduction of iodine ions and reduces defect state concentration, and defect passivation of grain boundaries crystalline quality, improve charge transport,	[123]

lead thiocyanate (Pb(SCN) 2	FTO/SnO_2/ $CH_3NH_3PbI_3$/ Spiro-OMeTAD /Au	15.57	N/A	17.80	5% $Pb(SCN)_2$ (molar ratio with respect to PbI_2	N/A	N/A	forms volatile products HSCN and CH_3NH_2, resulting in formation of excess PbI_2 that passivates GB	[124]
potassium thiocyanate	FTO/c-TiO_2/ m-TiO_2/$CH_3NH_3PbI_3$/Spiro-OMeTAD/Ag	19.38	N/A	19.6	1 mol%	N/A	N/A	Grain size and crystallinity improvement reduced recombination density,	[126]
methylammonium thiocyanate (MASCN) additive	Glass/FTO/TiO_2/ $CH_3NH_3PbI_3$/ Spiro-OMeTA)/Au	15.81	Died in 150 h.	18.71	40 mol%	Retained 16.34 % as of final PCE after 1000 h ~89.7 % from initial	air, RH= ~20-25%, without encapsulation,	rapid vacuum-based drying approach, high crystallinity, large carrier lifetimes	[128]
guanidinium thiocyanate (GuSCN)	FTO/TiO_2/ $CH_3NH_3PbI_3$/PCBM/Ag	15.57	Retained 60% PCE from initial PCE after 15 days	16.70	10% mmol	Retained 90% PCE from initial PCE after 15 days	Un-encapsulated, dark, RH=30-40%,	enhance the crystallinity, enlarge the crystal size, and reduce the trap density of the perovskite film	[129]

2.1.4 Alkane additives

Furthermore, alkane based additives can be another class of additives that has been briefly investigated within the $MAPbI_3$ framework. Additives like poly(vinylidene fluoride-co-hexafluoropropylene) (PVDF-HFP) have shown interaction with MA cation via hydrogen bonding with fluorine atoms in the additive. Such an additive is quite useful for indoor photovoltaic applications as the additive is reported to control the nucleation and growth rate on a very thin (~150 nm) active layer of $MAPbI_3$ through a one-step solution processing method. Thinner light absorber perovskite is usually full of voids and results in low fill factor, lower internal quantum efficiency due to poor perovskite film quality. However, increasing the thickness is not suitable to obtain semi-transparent films [131]. To solve this problem, poly(vinylidene fluoride-co-hexafluoropropylene) (PVDF-HFP) additive had illustrated less rough morphology when ~150 nm thick perovskite layer was obtained. Also, it was found that perovskite solar cells with PVDF-HFP film have a higher charge transfer rate and lower carrier recombination rate [132]. Similar observations were seen when another derivative of PVDF polyvinylidene fluoride-trifluoroethylene polymer P(VDF-TrFE) was employed in a two-step fabrication process instead [133]. Other than these additives, some other haloalkane additives like diiodomethane (CH_2I_2) and diiodoctane ($C_8H_{16}I_2$) have also been reported to reduce the trap states resulting in improved morphology and enhanced PCE [134,135]. Further, Table 9 represents the alkane additives and discuss their role in the $MAPbI_3$ framework. See Figure A0.13, Appendix 0, for chemical structures of discussed alkane additives.

Table 9 Alkane based additives and their role within $MAPbI_3$ framework.[58]

Additive in active layer	architecture	PCE, % (Pristine)	Stability (Pristine)	PCE, % (with additive)	amount of additive	Stability with additive	Stability conditions	Role of additive	Ref
poly(vinylidenefluoride-co-hexafluoropropylene) (PVDF-HFP	FTO/$cTiO_2$/$CH_3NH_3PbI_3$/spiro-MeOTAD/Au	7.2	N/A	10.6	N/A	N/A	N/A	Interact with uncoordinated MAI molecule through hydrogen bonds between fluorine atoms. This can improve the carrier lifetimes and reduce the charge transfer resistance, which contributes to enhancing PCE.	[132]
polyvinylidene fluoride-trifluoroethylene polymer P(VDF-TrFE)	FTO/c-TiO_2/mesoporous-TiO_2/ $CH_3NH_3PbI_3$ /spiro-MeOTAD/Ag	9.57±0.25%	N/A	12.54± 0.40	N/A	N/A	N/A	Two-step deposition, improved crystallinity and morphology, reduced carrier recombination of charge carrier, increased carrier lifetime	[133]
diiodomethane CH_2I_2	Glass/FTO/TiO_2/ $MAPbI_3$/Spiro-OMeTAD /Au	10.0	N/A	16.5	0.25 ml in 1 ml precursor	N/A	N/A	Iodine liberation, morphology enhancement	[135]
Diiodooctane DIO	Glass/ITO/PEDOT:PSS/$MAPbI_3$/PCBM/Ag	10.61	N/A	17.74	1 vol% in 1 ml precursor	N/A	N/A	Intermediate formation and morphology enhancement	[134]

2.1.5 Quantum dot-based additives

Recently, a new area of additives emerged based on quantum dots containing different functional groups introduced in the precursor. This allows the functional group to chelate with under coordinated Pb vacancy or iodine defect sites at the surface of the perovskite layer. At the same time, quantum dot reduces non-radiative recombination centres (due to the quantum confinement effect), while the chelating functional groups attached to quantum dot help co-ordinate with defect sites, improving the crystallinity of the film, thus passivating defects at grain boundaries [136–141]**.** In some cases, quantum dots can even promote charge transfer from the oxide surface to the perovskite layer, further reducing the charge trap density, boosting fill factor as high as 84% and efficiency as 21.04% [140,142]. A summary of such additives based on Quantum dots (QDs) is presented in Table 10.

Table 10 Quantum dots based additives for $MAPbI_3$.[58]

Additive in active layer	architecture	PCE, % (Pristine)	Stability (Pristine)	PCE, % (with additive)	amount of additive	Stability with additive	Stability conditions	Role of additive	Ref
carbon quantum dot (CQD)	ITO/NiO_x/ $CH_3NH_3PbI_3$ /PCBM/Ag	15.25	Remained ~ 10 % PCE from initial after 48 h	18.24	0.15 mg/mL	Remained~ 73.4 % PCE from initial after 48 h	Un-encapsulated, dark, RT, RH=80%,	Reduce non-radiative recombination loss, improves the crystallinity of film. Thus passivates grain boundaries and improves stability	[136]
carbon nanodots (CNDs)	ITO/NiO_x/$CH_3NH_3PbI_3$ /PC61BM/BCP/Ag	14.48% ± 0.39%	N/A	16.47% ± 0.26%	10 mg/mL	Remained ~18% as of an absolute value of PCE after 500 h	dark, 25 °C, RH=40% , air, un-encapsulated,	increase in the crystal size and a lower content of grain boundary defects and, longer carrier lifetimes.	[139]
carbon quantum dots (CQDs)	FTO/TiO_2/ $CH_3NH_3PbI_3$/ Spiro-OMeTAD /Ag	17.59	(a)Retained 74% from initial PCE after 1500 h (b)Retained 17% from initial PCE after 216h	18.81	0.05 mg/mL	(a)Retained 90% from initial PCE after 1500 h (b)Retained 70% from initial PCE after 216 h	(a) un-encapsulated, inert, (b) un-encapsulated, RH=50-60%,	passivate the grain boundaries and decrease the trap-state density. The bonding between CQDs and $MAPbI_3$ leads to a stable absorption of CQDs on the $MAPbI_3$ surface, forming a protective layer to prevent the perovskite from coming in contact with water, thereby enhancing the stability of PSCs.	[138]
nitrogen doped CQDs (N-CQDs),	ITO/PEDOT:PSS/ $CH_3NH_3PbI_3$/PCBM/Al	8.34	N/A	13.936	3 vol%	N/A	N/A	N-CQDs act like an intermediate and help to form dense and smooth perovskite, passivates the trap states and decreased the non-radiative charge recombination	[137]
Nitrogen-doped carbon dots (NCDs)	FTO/blTiO_2/ml-TiO_2/ $CH_3NH_3PbI_3$ /Spiro-OMeTAD/Ag	12.12 ± 0.28%	N/A	15.93 ± 0.15%	0.05 mg/mL	N/A	N/A	coordinate with the iodide ions and lead cations on the surface of perovskite, which effectively passivates the surface traps and help reduce non-radiative charge carrier recombination, the	[141]

								nitrogen dopants with lone electron pairs in NCDs optimise the interfacial energy level to enhance the charge carrier extraction efficiency at photoactive layer/TiO_2 interface	
potassium cation (K+) functionalized carbon nanodots (CNDs@K)	ITO/PTAA:F4TCNQ/$CH_3NH_3PbI_3$/PCBM/BPhen/Ag	18.25	N/A	21.04		N/A	N/A	defects passivation and crystallisation control of the perovskite film. K^+ in the grain boundary and prevents excessive cations from occupying interstitial sites, thereby reducing microstrain of polycrystalline film. the synergistic effect of tailored crystal size and suppressed grain boundary defects could reduce charge trap density, facilitate charge generation, and lengthen carrier lifetime,	[140]
graphene quantum dots (GQDs)	FTO/c-TiO_2/mp-TiO_2/ $CH_3NH_3PbI_3$/ Spiro-OMeTAD /Au	16.83	Remained ~ 15.6% as of final PCE after 30 days	18.34	1.5 mg/mL	Remained ~ 17.4% as of final PCE after 30 days	encapsulation-n/a, RH=36%, atm,	promote charge transfer from the perovskite layer to TiO_2 film. Faster electron extraction and a slower recombination rate , passivate hanging bonds at the perovskite GBs,	[142]

2.2 Inorganic additives

Inorganic salts can be further explained as per the category in the periodic table, i.e. based on alkali metals, alkaline earth metals, transition metals, other metals and other non-metals. These additives may exist in the form of inorganic halide salts or inorganic acids [143]

2.2.1 Alkali metals additives

Hydro halides are at the top, as hydrogen is the first element in group one of the periodic table. Soe et al. studied the incorporation of hydrohalic acids (HX, X=I, Br, Cl) in $MAPbI_3$ precursors prepared using DMF. It was found that HX incorporation in the perovskite layer alters the bandgap and unit cell parameters. The HI addition compressed bandgap, whereas HBr widens the bandgap at high concentrations (20-25 vol %). Further, these changes were found to be correlated with the types of defects present in polycrystalline perovskite thin films combined with the structural strain induced in very small crystallites. Thus, it was concluded that these acids could influence crystallization rate, surface coverage and improve morphology. However, HCl incorporation showed no influence on bandgap [144,145]. The same was verified by Yan and co-workers who investigated HI (Hydriodic acid) as an iodine quencher in $MAPbI_3$ precursor solution (prepared with isopropyl alcohol (IPA)), that further led to chemically passivate grain boundaries and increase in PCE from 16.13% (pristine) to 18.21% (with HI additive) [146]. Likewise, alkali metals such as Li, Na, and K combined with halogen counterparts have been inspected as additives for the $MAPbI_3$ light absorber layer. Grätzel and Friend co-workers demonstrated the influence of NaI (sodium iodide) on the optical, excitonic and electrical properties of $CH_3NH_3PbI_3$ perovskite prepared by a two-step sequential deposition technique. It was revealed that the NaI additive helps in the complete conversion of PbI_2 into $CH_3NH_3PbI_3$, leaving no unreacted PbI_2 and enhancing the crystallinity. Furthermore, KPFM measurements showed a reduction in work function (towards Au metal) for contact-potential difference (CPD) and proved the chemical passivation of perovskite surface due to additive incorporation in the precursor. Additionally, the hypothesis of partial substitution of Pb^{2+} with monovalent cations Na was discarded because replacing Pb^{2+} with the Na cations requires high energy, which cannot be obtained at room temperature since additives and films were processed at room temperature [147]. Similar reports were published from Chu and co-workers who investigated alkali metal chloride additives (LiCl, NaCl and KCl) in $MAPbI_3$ and suggested that mixed halide formation does not occur as Cl atoms easily evaporate due to the annealing

process, improving the crystallinity and carrier charge transport [148]**.** However, as the nuclei weight and radius increase, the A site cation is partially replaced, and a mixed perovskite with a double cation is formed (i.e. in the case of RbX and CsX, where X represents halide) [149] The partial substitution of cation was also observed when alkaline earth metals were employed as additives in the precursor. Hence, they are not the centre of attraction here and suggested that alkaline earth metals are best suited to replace Pb due to their divalent nature [150,151]. Further, alkali metal additives' chemical structures and role in the $MAPbI_3$ framework are summarized in Figure A0.14, Appendix 0 and Table 11, respectively.

Table 11 Alkali metal additives and their role in $MAPbI_3$ perovskite.[58]

Additive in active layer	Architecture	PCE, % (Pristine)	Stability (Pristine)	PCE, % (with additive)	amount of additive	Stability with additive	Stability conditions	Role of additive	Ref
HI Hydriodic acid	ITO/PTAA/ $CH_3NH_3PbI_3$/PCBM/Ti/Au	16.1	N/A	18.21	0.004 vol%	N/A	N/A	Grain size improvement	[146]
HCl	Glass/TiO_2/ $CH_3NH_3PbI_3$ /Spiro-OMeTAD/Au	9.96	N/A	14.49	volume ratio 8%,	N/A	N/A	Grain size improvement and morphology enhancement	[152]
HBr				13.53	volume ratio 6%	N/A	N/A		
HI				15.21	volume ratio 8%	N/A	N/A		
LiI	FTO/TiO_2/$CH_3NH_3PbI_3$/electrode	11.3	Remained ~1% PCE as of final value after 25 days	17.01	12mg/mL	Retained ~6% PCE as of final value after 70 days	un-encapsulated, ambient, air, RH=40%,	larger grain size and higher crystallinity and reduced PbI_2 residue	[153]
NaI	FTO/compact TiO_2 /mesoporous TiO_2 /CH_3 NH_3PbI_3 /SpiroMeOTAD/Au	14.01	N/A	15.14	0.02 mol/L	N/A	N/A	Improved crystallinity and grain boundary passivation	[147]
LiCl	Glass/ITO/PEDOT:PSS/ $CH_3NH_3PbI_3$ /$PC_{61}BM$/C_{60}/BCP/Al	11.40	Died in 50 days	9.98	0.25%, wt%	N/A	N/A	Improved crystallinity and homogenous nucleation, and crystallisation	[148]
NaCl				12.77	1.0%, wt%	N/A	N/A		
KCl				15.08	0.75%, wt%	Remained ~85% after 50 days	unencapsulated, inert (glove box) dark		

2.2.2 Transition metals additives

Additionally, some transition metals have also been reported as additives in $MAPbI_3$ precursors. One such example is n-type goethite (FeOOH) quantum dots that act as multifunctional additives. The addition of FeOOH QDs into precursor solution improves not only the performance but also stability. The investigation done by Wang and the group showed that FeOOH QDs could produce heterogeneous nucleation, passivate the trap states, and obstruct the ion migration. The investigation demonstrated that the oxygen (in FeOOH) as a Lewis base could coordinate with Lewis acid Pb^{2+}. The –OH group (in FeOOH) can coordinate with hydrogen atoms of MA^+. Thus, this interaction results in the delay of crystal growth kinetics, resulting in good quality of perovskite films that result in high PCE. Further, the iron in FeOOH QDs as a Lewis acid interact with Lewis base I^-. Thus, ion migration of I^- and MA^+ is controlled, resulting in enhanced intrinsic stability of solar cells [154]**.** Further, the transition metal halides, either with monovalent cations (i.e. AgI, CuI, CuBr), divalent cation ($NiCl_2$, $CuCl_2$, $ZnCl_2$, $CdCl_2$) [155–158] or trivalent cation (RhI_3) [159], frequently pointed out the improvement in crystallinity and grain boundary passivation.

Interestingly, in all these reports, Chlorine-based additive salts were reported to form the $MAPbI_3$ phase without mixed iodide and chloride as it was proposed that Cl atoms evaporate while annealing the films. Similarly, trivalent cation like Rh^{3+} was also noticed not replacing lead atoms when used in small quantities like 1 mol%. However, the addition to 5% could result in partial replacement of the Pb atom**.** Further, Table 12 summarizes the details associated with transitional metal additives. See Figure A0.15, Appendix 0, for chemical structures of transition metal additives.

Table 12 Transition metal additives and their role in $MAPbI_3$ perovskite.[58]

Additive in active layer	Architecture	PCE, % (Pristine)	Stability (Pristine)	PCE, % (with additive)	amount of additive	Stability with additive	Stability conditions	Role of additive	Ref
n-type goethite (FeOOH)	FTO/$cTiO_2$/mp-TiO_2/ $CH_3NH_3PbI_3$/Spiro-OMeTAD/Au	15.4	(a)Remained only 5.7 % as of final PCE after 360h. (b) retained 61% from initial PCEafter60 days (c) retained only 42% from initial PCE after480h	19.7	0.1mg/ml	(a) Retained 94 % after 360h. i.e. 17.9% (b) Retained 97% from initial PCE after 60 days (c)retained 92% from initial PCE after 480h	(a) inert, 85˚C, dark, non-encapsulated, (b) 10± 5% RH, (c) 100 mW cm^{-2}, inert, RT, mpp tracking,	Improved quality of perovskite and inhibition of iodine and methylamine ion migration	[154]
AgI	FTO/compact TiO_2 /mesoporous TiO_2 / $CH_3NH_3PbI_3$ /SpiroMeOTAD/Au	14.01	N/A	14.18	0.02 mol/L	N/A	N/A	Improved crystallinity and grain boundary passivation	[147]
CuI				15.25		N/A	N/A		
CuBr				15.61		N/A	N/A		
$NiCl_2$	ITO/SnO_2/ $CH_3NH_3PbI_3$ /SpiroMeOTAD/Au	17.25	Retained ~70% PCE after 100 h	20.61	0.03mM	Retained ~70% PCE after 100 h	En-capsulated, air,65 mW cm^{-2}, ~25 °C , RH=45%, without ultraviolet filter	High crystallinity, GB passivation,	[155]
$CuCl_2$	FTO/NiO_X/ $CH_3NH_3PbI_3$ /PCBM/BCP/Ag	9.73	N/A	15.22	2.5 mol%	N/A	N/A	improves morphology	[156]
$CdCl_2$	FTO/SnO_2 / $CH_3NH_3PbI_3$ /Spiro-OMeTAD/Au	11.7	N/A	13.2	1 % molar ratio	N/A	N/A	Enhance grain size and crystallinity	[157]
$ZnCl_2$				13.76	0.1 % molar ratio	N/A	N/A		
RhI_3	ITO/SnO_2/ $CH_3NH_3PbI_3$ /Spiro OMeTAD /Ag	19.09	Retained 75% of efficiency after 500 h	20.71	1 mol%	Retained 92% of efficiency after 500 h	un-encapsulated, dry air	Improved crystallinity and grain boundary passivation	[159]

2.2.3 Other metals additives

The most widely reported metal additive is PbI_2. Several groups have suggested using excess PbI_2 as an additive and studied the effect of the stoichiometric and non-stoichiometric composition of PbI_2 in $MAPbI_3$ perovskite [160,161]. Reports suggest that the addition of excess PbI_2 in perovskite increases power conversion efficiency (PCE) [160,162]. However, the influence of excess PbI_2 on photochemical stability is debatable [163]. Some research groups claim that excess PbI_2 passivates grain boundary [164], thus creates extra passivation [165], enhancing performance and stability overall [161,166]. On the contrary, some reports showed that excess PbI_2 could increase PCE but decreases PSC stability [167,168]. To resolve the issue, Stevenson and the group demonstrated that the stability associated with excess PbI_2 is affected by solvent coordination capacity with Pb atom and suggested that excess PbI_2 can work as a stabilizer to improve intrinsic stability if correct solvent (NMP) is chosen over commonly-used solvent DMF [169]. Later, other than PbI_2, adding $PbCl_2$ also reported to result in an equally good perovskite film quality with improved performance, but the outcome was reported as a mixed halide [170,171]**.** Hence, it is not focused here. Interestingly, Ngo and the group demonstrated a different approach by using PbS quantum dots as capping ligands in the precursor solution to control nucleation and morphology. This approach allowed to improve crystallinity and enhanced grain size, resulting in improved solar cell performance [172]. Further, a relevant summary is presented in Table 13. The chemical structures of other metal additives can be seen in Figure A0.16, Appendix, 0.

Table 13 Other metal additive for $MAPbI_3$.[58]

Additive in active layer	architecture	PCE, % (Pristine)	Stability (Pristine)	PCE, % (with additive)	amount of additive	Stability with additive	Stability conditions	Role of additive	Ref
PbI_2	FTO/c-TiO_2/m-TiO_2/ $CH_3NH_3PbI_3$/Spiro- OMeTAD/Au	15.95	N/A	18.42	10 % excess PbI_2	N/A	N/A	improves the crystallinity	[160]
PbI_2	Glass/FTO/ $CH_3NH_3PbI_3$/ Spiro-OMeTAD/Electrode/Encapsulation(UV-epoxy)	16.2	Retained 80% PCE till 12 h	16.5	10 mg/mL	Retained 80% PCE till 10 days	ambient air, 85ºC and 60% RH, 1sun	N/A	[168]
PbI_2	Glass/ITO/SnO2/ $CH_3NH_3PbI_3$/PTAA/MoO3/Al	~8.9%	Remained ~ 40% PCE after 1500 h	~15.6%	15% excess	Remained ~ 95% PCE after 1500 h	30 mW cm^{-2} at 40 ℃, inert	Excess PbI_2 forms adduct with the cosolvent (NMP) , improving PCE and stability.	[169] (Our work)
PbI_2	FTO/TiO_2/ $CH_3NH_3PbI_3$/Spiro-OMeTAD /Ag	7.23 ± 0.10	N/A	14.32±0.28%	concentration – N/A, by annealing @130˚C	N/A	N/A	grain boundary passivation	[173]
PbS QDs	FTO/SnO_2/ $CH_3NH_3PbI_3$ /Spiro-OMeTAD/Au	15.2	N/A	15.7	12.5mg/mL	N/A	N/A	Capping ligand for surface functionalization to improve crystallinity	[172]

2.2.4 Non-metal inorganic salts

Furthermore, the controlled nucleation, improved morphology, enhanced crystalline size and grain size with lower trap density were also noticed with additives based on other non-metals salts. During the two-step method, which is one of the commonly used fabrication approaches to fabricate planar heterojunction complex lead halide perovskite solar cells, the complete conversion of PbI_2 into $CH_3NH_3PbI_3$ is often observed to be restricted by the inadequate diffusion of CH_3NH_3I into PbI_2 film, which affects the short circuit current density. To overcome this problem, Pathipati and co-worker used ammonium iodide (NH_4I) in small quantity (5 wt%) in the PbI_2 solution and found this approach increases the porosity of PbI_2 film, allowing to improve film morphology and increasing grain size up to 500 nm. This, in turn, improves the fill factor and short circuit current density, improving the PCE compared to pristine solar cell [174]. Similarly, a drastic improvement in fill factor (from 27.53 without additive to 80.11 with NH_4Cl additive) was noticed when NH_4Cl was added in $MAPbI_3$ precursor. Moreover, as reported earlier, due to the quick evaporation of chlorine atoms, mixed halide formation did not take place [175]. Furthermore, improved performance and higher stability were observed with different ammonium halide salts (NH_4X, where X can be I, Cl, Br) even when using the single-step solution process method. Although, NH_4I showed the highest performance amongst all [174–176]. Another ammonium-based additive, $NH_4H_2PO_2$ (ammonium hypophosphite-AHP), was reported to show similar behaviour. Surprisingly, one of the by-products (H_3PO_2) from CH_3NH_3I synthesis was found suppressing the formation of molecular iodine (i.e.the oxidation of I^- to I^2) [177,178]. This led to the idea of using $NH_4H_2PO_2$ (ammonium hypophosphite-AHP) as an additive in the PbI_2/CH_3NH_3I precursor. Huang and co-workers found that AHP forms a complex with PbI_2, which leads to improvement in crystallinity and grain size. In turn, this improves PV performance due to crystalline grain boundaries [179]. Besides, in a recent report, it was illustrated that N_2H_5I, an iodine quencher in the $MAPbI_3$ active layer, can form an intermediate complex with PbI_2 and enhanced crystallinity and grain size ~1100 nm, causing grain boundary passivation. Which, in turn, reduced hysteresis in solar cells, improved efficiency and intrinsic stability of solar cells up to 4400 h [180]. Similar reports were received from Huang and the group who reported N_2H_5Cl incorporation in $MAPbI_3$ [181]**.** Whereas hypophosphorous acid (HPA) was used to assist crystallization dynamics for large area substrates [182]. Chemical structures and a summary of these additives is presented in Figure A0.17, Appendix 0 and Table14, respectively.

Table 14 Non-metal additives and their role in $MAPbI_3$ active layer.[58]

Additive in active layer	Architecture	PCE, % (Pristine)	Stability (Pristine)	PCE, % (with additive)	amount of additive	Stability with additive	Stability conditions	Role of additive	Ref
NH_4I	Glass/ITO/PTAA/ $CH_3NH_3PbI_3$/PCBM/Ag	15.2	Retained ~70% PCE after 20 days	17.4	5 wt%	Retained ~80% PCE after 20 days	RH=50 ± 5%, un-encapsulated, ambient air,	Improved morphology, increased crystalline size and grain size, lower trap density	[174]
NH_4Cl	ITO/PEDOT:PSS/ $CH_3NH_3PbI_3$/ $PC_{61}BM$/Al	7.97	N/A	9.93	17.5mg/mL	N/A	N/A	Improved morphology, increased crystalline size and grain size, lower trap density	[175]
NH_4F	ITO/PEDOT:PSS/ $CH_3NH_3PbI_3$ /$PC_{61}BM$/LiF/Al	13.74	Retained 70 % PCE after 5 weeks	15.15	10 mol%	Retained 82 % PCE after 5 weeks	Encapsulated, air	Improved morphology, increased crystalline size and grain size, lower trap density	[176]
NH_4Cl				16.88		Retained 87 % PCE after 5 weeks			
NH_4Br				16.85		Retained 89 % PCE after 5 weeks			
NH_4I				17.44		Retained 91 % PCE after 5 weeks			
$NH_4H_2PO_2$	ITO/PTAA:F4-TCNQ/ $CH_3NH_3PbI_3$/$PC_{61}BM$/TrNBr/Ag	9.4 ± 1.0%	N/A	16.5 ± 0.7%	2.5mg/ml	N/A	N/A	Intermediate with Pb and improved crystallinity grain size	[179]
N_2H_5I	Glass/ITO/SnO_2/ $CH_3NH_3PbI_3$/PTAA/MoO_x/Al	14.98	Retained ~60 % PCE after 4400 h	17.03	0.5%, % by wt	Retained ~80 % PCE after 4400 h	inert, light 50-60 $mWcm^{-2}$, 50-60 ˚C.	Intermediate between PbI_2 and N_2H_5I, improved crystallinity, grain size	[180] (Our work)
N_2H_5Cl	ITO/PEDOT:PSS/ $CH_3NH_3PbI_3$/PCBM/C_{60}/ BCP/Ag	7.14	N/A	12.66	PbI_2/MAI/N_2H_5Cl molar ratio = 1:1:0.2	N/A	N/A	Intermediate between PbI_2 and N_2H_5Cl, improved crystallinity, grain size	[181]

hypophosphorous acid (HPA)	Glass/FTO/TiO_2/ $CH_3NH_3PbI_3$/ETL/electrode	5.1	N/A	8	0.75 ul/mg solution in 1 ml of MAI	N/A	N/A	larger grains with a smoother surface, Additive acts as a reducing agent for iodine	[182]

2.3 Summary of literature review:

To conclude, the progress and updates in additives for the $MAPbI_3$ photoactive layer in perovskite solar cells were covered. As known, the poor intrinsic and extrinsic stability causes a restriction in the substantial commercialization of the PSC. Intrinsic instability is considered due to the presence of under-coordinated Pb sites or escape of a volatile product or formation of molecular iodine; either of these creates a defect in the perovskite surface. This literature review summarized various additives that can coordinate with the mentioned defect sites and improve stability. The literature review analysis suggested that amines, heterocyclic amines, and their derivatives, followed by carbonyl and acetate functional groups, can improve intrinsic stability by co-ordinating with Pb defect sites. On the other hand, acid, esters, ether and alcohol, and S atom-based additives can be mainly valuable to boost ambient stability. For a comparison, see Figure A0.3, Figure A0.10, Figure A0.12, Appendix 0, respectively. Similarly, the comparison for inorganic additives is presented in Figure A0.18, Appendix 0. However, it must also be noted that additive investigation is often limited to efficiency enhancement instead of intrinsic photostability improvement, despite operational stability being a must condition to commercialize PSCs successfully. Therefore, investigating the additive influence on the intrinsic photostability of perovskite films and solar cells is essential and demands immediate attention.

2.4 Aim

Thus, this research project aims to improve the intrinsic stability of the $MAPbI_3$ perovskite-based light-absorbing layer using additives. For this purpose, the impact of additives incorporation within perovskite films and their influence on photochemical stability have been intensively investigated. Further, the impact of additive incorporation on the morphological, optical, and electrical properties of perovskite films and solar cell devices has been studied. This is because additives with stabilization effect typically resulted in improved nucleation and growth, film morphology, crystallinity, and grain size leading to passivate grain boundary via complex /intermediate formation as observed in the literature review. Similar characteristics were also observed during the additives investigation for this thesis and presented under the section “Results and discussion.” In the same context, device performance and intrinsic device

operational stability under illumination have been further tested. Later, the stability mechanism is proposed with respect to the structure and composition of additives in the perovskite film.

Utilizing literature review analysis as a valuable key for rationalising additives, pyridine derivatives (amines), acids, esters, ethers are investigated as organic additives to monitor the effect on intrinsic stability of $MAPbI_3$. On the other hand, N_2H_5I and PbI_2 are investigated as inorganic additives.

3. Experimental section

This section describes the additives and materials used, methodology to conduct experiments, and techniques performed to characterize thin films and solar cells in the scope of this thesis.

3.1 Materials

The chemical structures of investigated additives are shown in Figure 8 below.

Inorganic additives

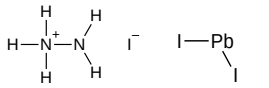

Hydrazinium iodide Lead iodide

Organic additives

Acid containing additives

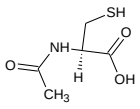

Acetyl cysteine

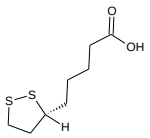

Lipoic acid

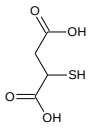

Mercaptosuccinic acid

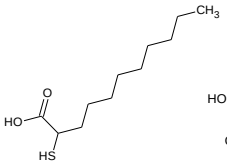

Mercaptoundecanoic acid

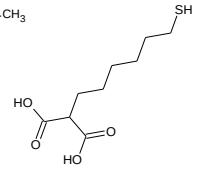

SHS-35

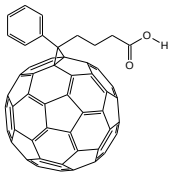

PCBA

Ester based additives

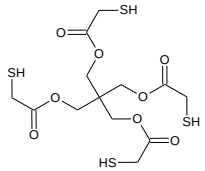

Pentaerythritol tetrakis(2-mercaptoacetate)

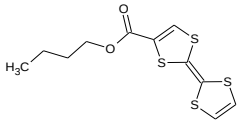

Tetrathiofulvalene derivatve 1,3-Dithiole-4-carboxylic acid, 2-(1,3-dithiol-2-ylidene), butyl ester

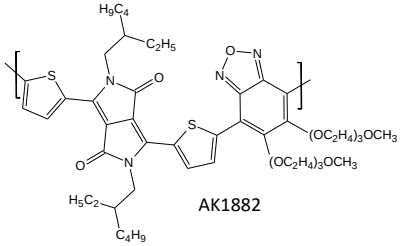

AK1882

Ether based additives

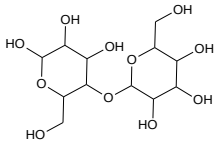

Lactose

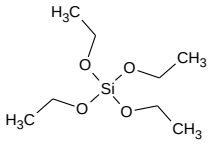

Tetraethyl orthosilicate

Pyridine derivatives

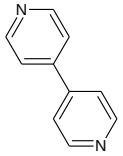

γ-bipyridyl

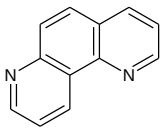

1,10 phenanthroline

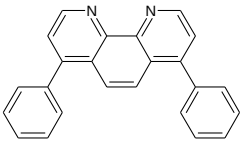

Bathophenanthroline

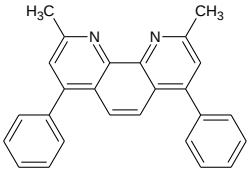

Bathocuproine

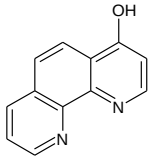

Oxiphenanthroline

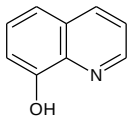

8 Oxyquinoline

Carbonyl vs Sulphide

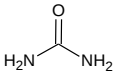

Urea

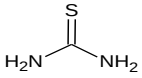

Thiourea

Other additives

Commercially available photocurable epoxy resin Delo: exact structure not available

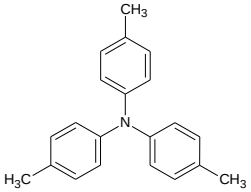

PTA

Figure 8 Investigated additives and their chemical structures

Following the classification in the literature review, the functional groups present in the investigated additives are shown in Table 15.

Table 15 Investigated additives with their respective functional group

S.No	Name of Additive	Functional groups in additive							
		amines and derivatives	carbonyl	acid	ester	ether	alcohol	thiols	other sulphur based additives
1.	Hydrazinium Iodide	✓							
2.	Lead Iodide with NMP -(functional group shown here is for NMP)	✓	✓						
3.	Acetylcysteine	✓		✓				✓	
4.	Lipoic Acid			✓					✓
5.	Mercaptoundeconic acid			✓				✓	
6.	Mercaptosuccinic acid			✓				✓	
7.	SHS35			✓				✓	
8.	Phenyl-C_{61}-butyric acid (PCBA)			✓					
9.	Poly[bis(4-phenyl)(4 -trimethylphenyl)amine] - PTA	✓							
10.	Urea	✓	✓						

11.	Thiourea	✓							✓
12.	Lactose					✓	✓		
13.	Tetraethyl orthosilicate(Si-(O-C_2H_5)$_4$					✓			
14.	Gamma bipyridyl	✓							
15.	8 Oxyquinoline	✓					✓		
16.	4-hydroxy-phenanthroline	✓					✓		
17.	1,10 Phenanthroline	✓							
18.	Bathoocuproine	✓							
19.	Bathophenanthroline	✓							
20.	Pentaerythritol tetrakis(2-mercaptoacetate)				✓			✓	
21.	Tetrathiafulvalene				✓				✓
22.	AK1882	✓	✓		✓				✓
23.	Delo (commercial product - functional group not known)								

The highlighted additives (green coloured) in Table 15 showed improved intrinsic stability over pristine $MAPbI_3$ films (Figure A1.1, Appendix A1). While unhighlighted represents additives, those did not improve the photostability of thin-film (Figure A1.2, Appendix A1). However,

only the best results will be the focus of this thesis. Therefore, the best additives improving stability will be described under the section " 4. Results and discussion".

Besides the above-studied additives, other typically used materials and chemicals involved are N N dimethylformamide (DMF, anhydrous, 99.99%), and N-methyl-2-pyrrolidone (NMP), aqueous tin oxide (15% concentration), PCBM, toluene, chlorobenzene and ethyl acetate; those were purchased from Sigma-Aldrich and used as received. PCBA, PTA, PTAA, MAI, PbI_2 were home-grown and used as 99.999 % pure. Glass substrates were used for thin-film experiments. ITO coated substrates were used as required for device performance and device stability experiments.

3.1.1 Preparation of Precursor Solutions:

0.3M solution of $MAPbI_3$ combined with additives was used to prepare thin films. Additives were added by 5%, percentage by weight unless specified. Further, 1.4M solution of $MAPbI_3$ was used to prepare devices unless specified. Filtered solutions were used for film and device fabrication and characterisation. Precursor solutions were filtered with 0.45um PTFE filters. The precursor solutions usually contained MAI and PbI_2 dissolved in either pure DMF or the mixture of DMF/NMP (4:1 v/v) and annealed at 70 ˚C overnight. The absorber layer for thin films and PSCs are made using this solution-processed precursor with a one-step spin coating method. For which, toluene is used as an antisolvent.

3.1.2 Thin Film Preparation:

Glass substrates were cut into 25 mm* 25 mm size and cleaned. Deionized water, acetone and isopropanol were used to give an ultra-sonication bath for 15 minutes in this particular sequence for cleaning substrates. Upon cleaning, substrates were plasma treated for 5 minutes. Then, transferred into Argon filled glovebox. 0.3M solution of $MAPbI_3$ is used to prepare perovskite film on the glass substrate. (with the respective additive added by 5 wt% in 1 ml precursor). The absorber layer was spun at 3000 rpm and annealed at 100°C for a minute.

3.1.3. Device Preparation:

Devices are prepared in n-i-p configuration due to better reproducibility and higher efficiencies. Typically architecture of the device consists of Glass/TCO/ETL/Passivation layer/$MAPbI_3$(with or without additive)/HTL/metal electrode. ITO is used as TCO. To prepare PSCs, glass substrates coated with Indium Tin Oxide(ITO) were cut into 25 mm* 25 mm size and cleaned. Deionized water, acetone and isopropanol were used to give an ultra-sonication bath for 15 minutes to clean the ITO substrates in this particular sequence. Upon cleaning, substrates were plasma treated for 5 minutes. Usually, SnO_2 is used as ETL followed by a passivation layer of either PCBA or PCBM. Incase of PCBA concentration used is 0.4mg/ml in toluene and in case of PCBM concentration used is 30mg/ml in CB. ZnO is occasionally used as specified. The ETL layer of SnO_2 is spun at 4000 rpm and annealed at 170℃ for 15 minutes. This SnO_2 solution was made by adding deionized water to dilute tin oxide concentration from 15 % to 10 %. Water was added in the ratio of 2:1. Further, this solution was ultra-sonicated for 5 minutes and filtered using a 0.45um PES filter. The filtered solution was used to spin coat on cleaned substrates. In the case of ZnO, ZnO is spun at 6000 RPM and further annealed at 200℃ for 1 hour. The ZnO solution was made by mixing 0.100 g zinc acetate dihydrate with 28.0 ml monoethanolamine in 1 ml of 2-methoxyethanol and stirring it overnight at room temperature. Thus obtained ZnO was filtered using 0.45 um filters before spinning coating onto the substrates.

All the subsequent layers after SnO_2 is spin-coated in Ar filled glovebox. In the glovebox, these substrates were heated at 150 ℃ for 10 minutes. Inside the glove box, first, PCBM /PCBA layer was spun at 3000 rpm and annealed for 5 minutes at 80℃/100℃ respectively. Further perovskite layers were spun at 4000 rpm. For the perovskite layer, the one-step spin coating was used, toluene was used as antisolvent. These films were further annealed at 85 ℃ for 10 minutes. Either PTA (6 mg /ml in toluene) or PTAA (6mg/ml in toluene) was used as HTL and was spun on the perovskite layer at 3000 rpm. Polystyrene (0.4mg /ml in ethyl acetate) is spun on the perovskite layer before evaporating electrodes. Then, MoO_3 (10nm) and Silver (100nm) electrodes were used.

To test the device stability, devices were fabricated as Glass/ITO/SnO_2/$MAPbI_3$/PTAA/V_2O_5/Al. This is to investigate that stability of the absorber

layer is not affected by the instability of the passivation layer. Here V_2O_5 and Al were thermally electrodes.

3.2 Methodology

The scheme of the methodology implemented during the thesis work is shown in Figure 9. The motivation behind this methodology is to screen additives that enhance the intrinsic stability of the perovskite photoactive layer. Additives are added to the precursor solution. A thin film study is opted before investigating solar cell performance with additives. This allows monitoring the influence of additives on the perovskite layer without the effect of the charge transport layer or passivation layer. The intrinsic photostability tests are designed according to International Summit on Organic Photovoltaic Stability (ISOS) protocols[183]. The exact ageing conditions are described separately for each section.

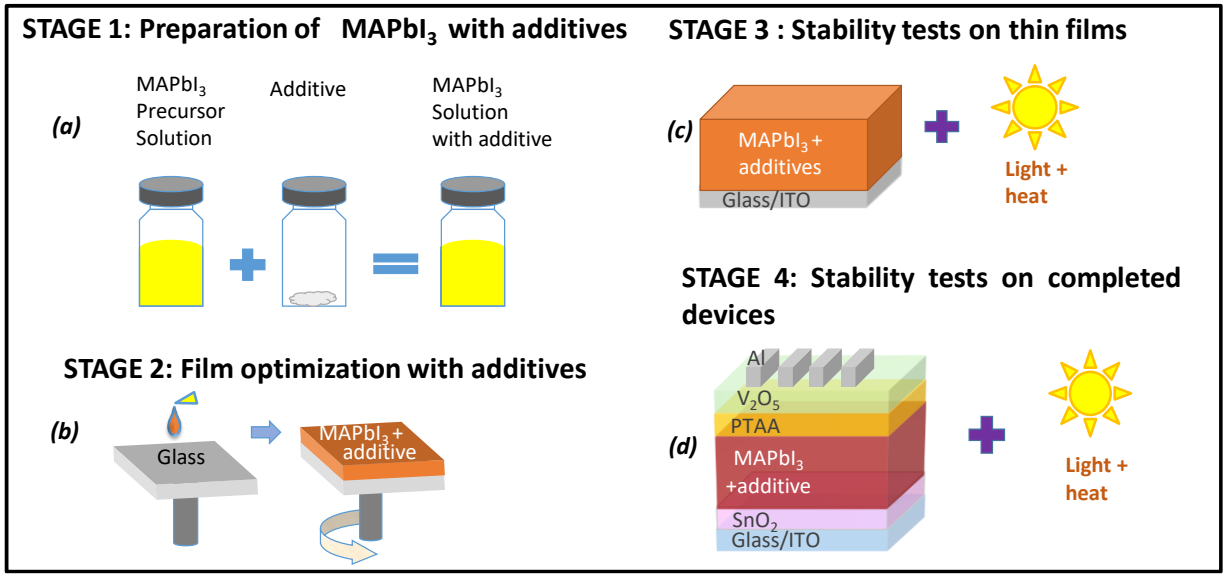

Figure 9: Methodology of the experiment. (a) solution preparation (b) Spin coating process for device optimization (c) conditions for stability tests (d) completed device upon stability tests.

The methodology of the experiment can be described in the following parts:

i) Prepare the precursor solution with an additive.

ii) Next, prepare thin films of perovskite precursor with additives on glass substrates, using the one-step spin-coating method. This allows understanding the impact of

additives on the photostability absorber layer. Because glass substrate is considered inert material, hence it will not influence degradation dynamics.

iii) Test photochemical stability of perovskite film with the additive by exposing the film to the given light intensity at a certain temperature in an inert environment. Therefore, the experiments are performed in a glovebox to minimise the effect of external factors such as moisture, water, air.

iv) Further, improvement in intrinsic stability is characterised using UV-Vis and XRD measurements (primarily), performed with a specific time interval.

v) Thus, the most stable additive is screened and further adopted to check the device performance of the solar cell with the selected additive.

vi) If device performance is higher than pristine perovskite, prepare solar cell devices with this additive and check device stability. This is because the PCE of PSCs is going higher, but stability is still to be achieved. Hence here, the aim is to screen the additive that enhances stability and shows decent performance.

3.3 Characterisation Techniques:

3.3.1 UV-visible spectroscopy

The absorbance feature of the perovskite layer can be monitored using UV-Vis spectra. The evolution of the absorbance feature further indicates the stability or instability of film for additive incorporation with respect to time. The UV-Vis spectra were measured using AvaSpec-2048-2 UV–Vis fibre spectrometer integrated inside the glove box.

3.3.2 XRD measurements

Additionally, X-ray diffraction patterns are used to verify the phase and crystallinity of the perovskite films. Besides, XRD can help to investigate adduct formation, degradation byproducts. XRD patterns were measured using a Bruker D8 Advance powder diffractometer (Cu-K_α radiation, 5-60° 2 theta range, 0.0219° increment step). Measurements were carried

out in fixed illumination mode with no sample rotation. The time interval of 0.2 seconds, voltage 40kV, filament current 40 mA was used for all the measurements.

3.3.3 FTIR spectroscopy

FTIR spectroscopy can reveal the changes in vibrations corresponding to the functional groups associated with additive in $MAPbI_3$. Thus, it can help to understand the additive interaction with the $MAPbI_3$ framework. The FTIR spectra were obtained using Bruker Alpha II with an ATR module (diamond crystal).

3.3.4 Photoluminescence

Photoluminesce measurements can reveal the changes in photoemission upon additive incorporation. That can further lead to correlate charge transport properties. The PL measurements were carried out using Automatic Research GmbH LBIC+PL+EL microscopy setup with Horiba spectrometer. All samples were measured with 532 nm laser wavelength at 0.05s integration time, 0.5 slit-width. For PL vs Power dependency, laser power variation was from 18.5 μW (10%) to 185 μW (100%).

3.3.5 Atomic Force Microscopy

AFM topography is a useful tool to reveal changes on the surface of perovskite film upon additive incorporation and photostability experiments. AFM topography images were obtained in a semicontact mode using Cypher ES atomic force microscope installed in an Ar-filled glovebox. Single crystal diamond probes (HA_NC/FD) were used to reduce the sticking of material from the photodegraded samples to the tip and avoid imaging artefacts.

While in-situ measurements can reveal the detailed mechanism of adduct formation, AFM Insitu photo-degradation was performed using a laser beam of 405 nm wavelength, with a light intensity of 10 kW m^{-2}.

3.3.6 Scanning Electron Microscopy & Energy Dispersive Xray.

Similar to AFM topography, SEM topography is very useful, especially in measuring grain size and change in morphology upon additive incorporation in $MAPbI_3$ film. Additionally,

EDX allows to compare the quantity of lead before and after photostability test and thus additive binding with Pb site can be understood.

For excess PbI_2 investigation, EDX analysis was performed on an Oxford Instruments Inco Energy unit integrated with the Zeiss SUPRA 25 microscope. For HAI related studies, SEM and EDX measurements were performed using the Helios G4 Plasma FIB Uxe double-beam scanning electron microscope. A top view imaging was performed in secondary electron (SE) mode at 5-10 kV. The energy-dispersive X-ray spectroscopy (EDX) was implemented at 10kV. The Octane Elite Super detector by EDAX and Team Software by EDAX was used within the FEI Helios system. The EDX signal was averaged along the sample surface in order to determine the I:Pb ratio.

3.3.7 X-ray photoelectron spectroscopy

XPS was used to measure core level and VB spectra with the assistance of a PHI XPS 5000 VersaProbe spectrometer (ULVAC-Physical Electronics, USA) equipped with a spherical quartz monochromator and an energy analyzer working in the range of binding energies from 0 to 1500 eV. The energy resolution was $\Delta E \leq 0.5$ eV. The samples were kept in the vacuum chamber for 24 h prior to the experiments and were measured at a pressure of 10^{-7} Pa.

3.3.8 J-V characterisation

Device performance characterisation was done by measuring Current-Voltage (*J-V*)behaviour under AM 1.5G (100 mW cm^{-2}) solar illumination simulator inside the glovebox. This instrument is provided by a Newport Verasol AAA class solar simulator. The illumination intensity was checked before each measurement using a calibrated silicon diode with known spectral responses. The *J-V* curves of all devices were measured while applying a metal mask with a 0.041 cm^2 window (unless specified) using the Advantest 6240A Source measurement units.

4. Results and Discussion

4.1 Impact of solution formulation on the excess of PbI_2 additive in $MAPbI_3$ thin films and solar cells

PbI_2 as an additive is one of the controversial additives investigated in the $MAPbI_3$ light-absorbing layer. Many groups have investigated the non-stoichiometric usage of PbI_2. The majority of researchers have reported that excess of PbI_2 (over stoichiometric) improves PCE. Nevertheless, its impact on photostability was debatable [184,185]. Some reports showed that excess PbI_2 passivates grain boundary [164,186], generating passivation effect [165,187], improving performance and stability overall [166,187,188]. Contrariwise, some reports showed, employing an excess of PbI_2 in precursor solution reduced the stability of PSC [189], even in an inert environment [168,190].

However, these reports lack the focus on the aspect of solvent engineering while reporting excess PbI_2 and its impact on photostability. Since the choice of solvents affects perovskite film quality, morphology, device performance and stability due to the difference in coordination between perovskite material and various solvents [191–200], studying the impact of excess PbI_2 in $MAPbI_3$ perovskite with respect to different solution formulations is investigated. For this purpose, DMF was chosen, a commonly used solvent to prepare perovskite ink [196,201]. However, reports have shown that DMF exhibits poor coordination ability with PbI_2 due to lower boiling point (152℃) and higher evaporation rate, which may cause instability. Next, NMP was chosen, which exhibits a higher boiling point (203℃) and low evaporation rates [202,203], producing a relatively stable intermediate phase with PbI_2 [195,204,205], due to the strong intercalation properties [193,206], further leading to rapid nucleation and growth of perovskite crystals with a uniform and good film morphology [203,207]. Further, reports have shown that 20 % addition of NMP gives the best results; therefore, 20 % NMP with 80% DMF is used to yield 1 ml of DMF/NMP mixture solution

[197]. An overview of the chemical structures of these two solvent DMF and NMP is further shown in Figure A2.1 in Appendix 2.

Then, films were prepared with these two solution formulations- pure DMF and DMF/NMP mixture. The films were prepared in the following configuration: ITO/ZnO/$MAPbI_3$ (with and without excess PbI_2) /PTA. Then, films were placed into a photodegradation chamber in N_2 filled glovebox under white light with power 50 mW cm^{-2} at 60°C for 200 h [183]. Fresh and photoaged films were characterized using UV-Vis Spectra, X-ray diffraction (XRD) primarily.

Here, the reference $MAPbI_3$ film from pure DMF is represented as $MAPbI_3$. DMF and $MAPbI_3$ film with 15% excess PbI_2 from pure DMF is represented as $MAPbI_3$+PbI_2.DMF. Likewise, the reference $MAPbI_3$ film from DMF/NMP mixture is represented as $MAPbI_3$.NMP and 15% excess of PbI_2 in DMF/NMP is denoted as $MAPbI_3$+PbI_2.NMP.

4.1.1 Photostability of thin-films

The XRD patterns of all four films (fresh stage) are presented at a glance in Figure A2.2a, Appendix 2, which indicates the XRD patterns of $MAPbI_3$. DMF and $MAPbI_3$+PbI_2.DMF films are less crystalline. On the other hand, XRD patterns of $MAPbI_3$.NMP and $MAPbI_3$+PbI_2.NMP films appear more crystalline. Later, the SEM images revealed the morphological changes in the films (Figure A2.2b-e, Appendix 2). It is noticed that $MAPbI_3$.NMP and $MAPbI_3$+PbI_2.NMP improves the film morphology, resulting in a smooth surface.

UV-Vis tests revealed that all fresh films (independent of solvent formulation or excess PbI_2 content) had an absorbance feature/characteristic at 750 nm, corresponding to perovskite formation. However, at 500 nm, a shoulder corresponding to PbI_2 emerged for fresh $MAPbI_3$.DMF and $MAPbI_3$+PbI_2.DMF films [188]. Whereas for fresh $MAPbI_3$.NMP and $MAPbI_3$+PbI_2.NMP films, this shoulder was observed to be prolonged (from 450 nm

to 540 nm), possibly due to the presence of an intermediary phase/adduct between PbI_2 and NMP [197,207,208].

Following the photoaging, the absorbance feature/characteristic at 750 nm for $MAPbI_3$+PbI_2.DMF vanished utterly. Only a peak matching to PbI_2 remained near 500 nm, demonstrating that extra PbI_2 speeds the disintegration of perovskite film when made with pure DMF. The absorbance characteristic/shoulder at 750 nm for $MAPbI_3$+PbI_2.NMP, on the other hand, remained stable, implying that the destabilising effect of over stoichiometric PbI_2 was inhibited due to the presence of co-solvent NMP. Further, comparing absorbance spectra with and without excess PbI_2, before and after photoaging is displayed below (Figure 10a and 10b) [169].

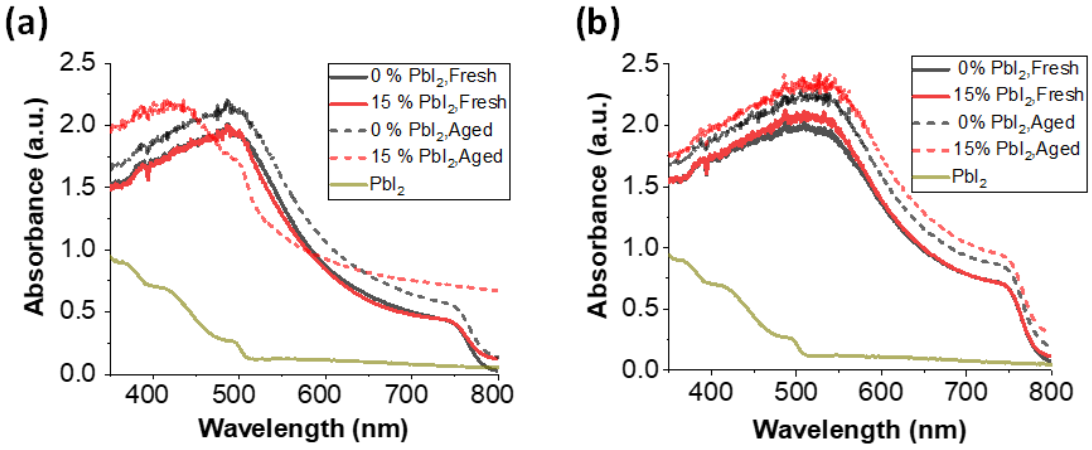

Figure 10 Absorbance spectra of fresh and photoaged $MAPbI_3$ films with 0% and 15% excess PbI_2 (a) from pure DMF (b) from DMF/NMP cosolvents.[169]

XRD measurements demonstrated similar observations. The fresh $MAPbI_3$.DMF exhibited XRD patterns of perovskite at 14.14°, 20.03°, 23.52°, 24.54°, 28.45°, 31.93°, 40.65°, and 43.21° [191,209]. However, peaks matching to PbI_2 were observed at 12.70° and 25.68° [201]. These peaks were visible even after photoaging. However, photoaging resulted in a small peak at 31.32° that was linked to Pb. $MAPbI_3$+PbI_2.DMF exhibited the same position of XRD peaks as

$MAPbI_3$.DMF. But, more PbI_2 peaks were located at 12.68°, 25.69°. To add on, the intensity of the PbI_2 peak at 12.68° was found to increase due to increased PbI_2 content for $MAPbI_3$+PbI_2.DMF film. Unfortunately, $MAPbI_3$+PbI_2.DMF was totally degraded after photoaging, leaving PbI_2 as a minor by-product and Pb as the predominant by-product, with strong peaks at 12.68° and 31.27°, respectively (Figure 11a) [210]. Fresh $MAPbI_3$.NMP revealed peaks of perovskite at 14.14°, 20.06°, 23.53°, 24.57°, 28.51°, 31.94°, 40.80°, and 43.31° [208]. Further, PbI_2 signals were found to be displaced at 12.78° and 25.69° (Figure 11c) [198], accompanied by the additions peaks at 8.3° and 11.10°, belonging to NMP-PbI_2 adduct [197,198]. When PbI_2 concentration is increased ($MAPbI_3$+PbI_2.NMP), the low-intensity peak of NMP-PbI_2 adduct developed a stronger peak intensity (combined with PbI_2 peak at 12.78°), and the signal at 11.10° disappeared. Later, after photoaging, the adduct formed by NMP and over stoichiometric PbI_2 remained stable but displaced slightly from its initial position to 8.18° (Figure 11d) [191,198,208]. Furthermore, the PbI_2 peak was observed to be slightly shifted to 12.76°, with only a minimal peak corresponding to Pb at 31.31°, implying that when formulated from DMF/NMP combination, conversion of PbI_2 into Pb is slowed, resulting in visible, stable peaks corresponding to perovskite (Figure 11c and 11d). It implies that the PbI_2-NMP adduct is stable against photodegradation over pure PbI_2, which is why $MAPbI_3$+PbI_2.NMP remains intrinsically photostable but $MAPbI_3$+PbI_2.DMF degraded in the absence of PbI_2-NMP adduct.

Additionally, a qualitative comparison of photoaged $MAPbI_3$.DMF, $MAPbI_3$+PbI_2.DMF, $MAPbI_3$.NMP and $MAPbI_3$+PbI_2.NMP films showing a share (%) of perovskite, lead iodide and lead that remains upon photoaging is represented in Figure A 2.3, Appendix 2.

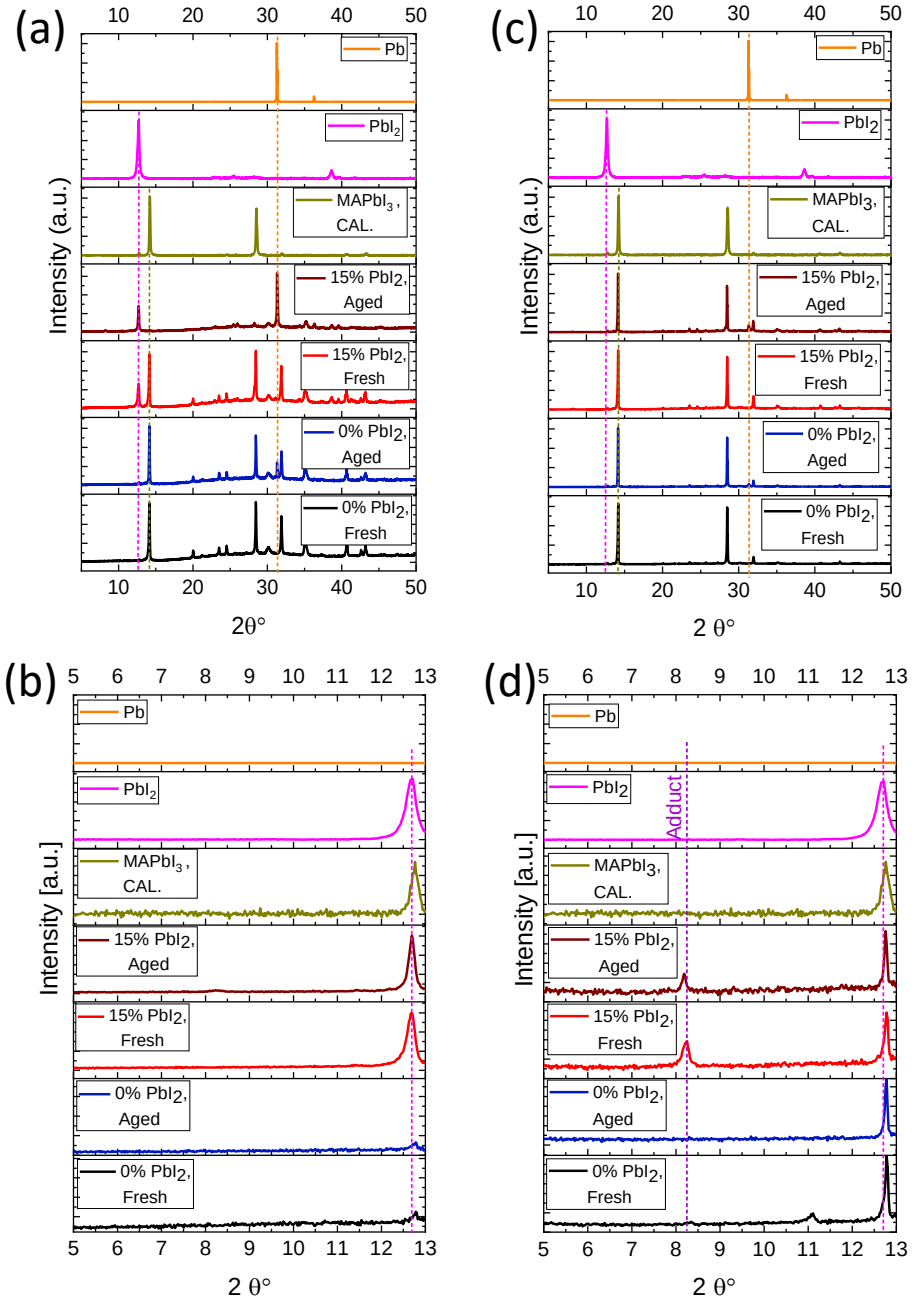

Figure 11 XRD pattern of fresh and photoaged $MAPbI_3$ films with 0% and 15% PbI_2 (a) from pure DMF (b) zoomed XRD patterns from 5° to 13° from pure DMF (c) from DMF/NMP mixture (d) zoomed XRD patterns from 5° to 13° from DMF/NMP showing adduct formation .[169]

4.1.2.Proposed mechanism of improved stability with $MAPbI_3$+PbI_2.NMP

XRD results suggested that PbI_2-NMP adduct formation improves the photostability of $MAPbI_3$+PbI_2.NMP. To gain a deeper insight, the effect on the binding of lead iodide to yield $MAPbI_3$ with these two solvent compositions – pure DMF and DMF/NMP was investigated using the XPS technique. The XPS spectra of Pb $4f_{7/2}$ fresh films (Figure 12a and12b) demonstrated that the chemical state of lead atoms was found to be similar to that of the $MAPbI_3$, regardless of the type of formulation or the amount of excess PbI_2. Conversely, XPS Pb $4f_{7/2}$-spectra of photoaged $MAPbI_3$+PbI_2.DMF film revealed a high-energy shift with the excess of PbI_2 for full coincidence with the spectrum of reference PbI_2, proposing full degradation of perovskite (Figure 12c). On the other hand, $MAPbI_3$+PbI_2.NMP film did not show any shift in XPS spectra of Pb $4f_{7/2}$ spectra (Figure 12d). This validates that when over-stoichiometric PbI_2 is present in the system, NMP as a co-solvent forms a stable and robust adduct with Pb. This was further supported with EDX measurements of the atomic ratio of iodine to lead atoms (Figure 12e).

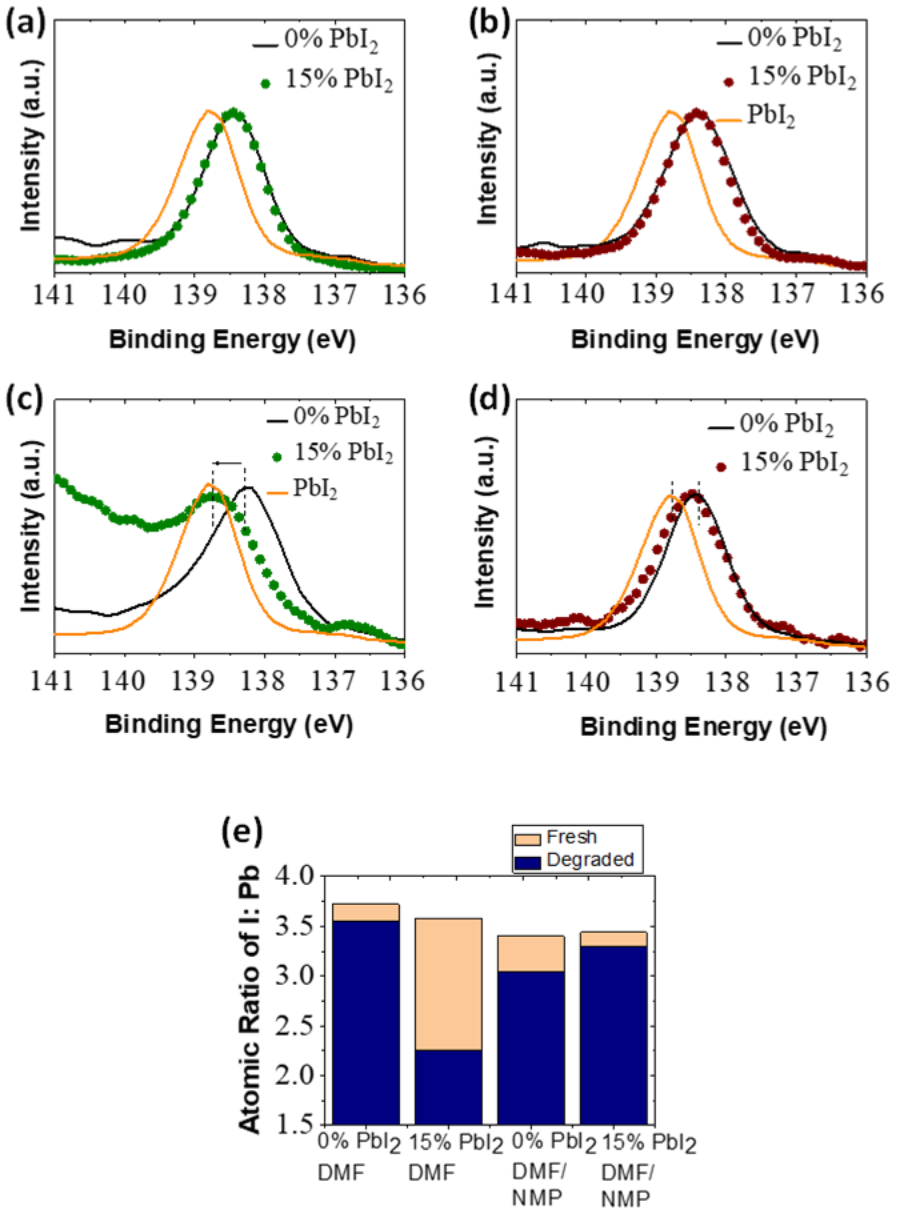

Figure 12 XPS spectra of Pb 4f of MAPbI3 films with 0% and 15% excess lead iodide (a) fresh, from DMF (b) fresh, from DMF/NMP mixture (c) photoaged, from DMF (d) photoaged, from DMF/NMP mixture (e) comparison of EDX analysis of fresh and photoaged film with reference to solution formulation with and without excess PbI_2

AFM Insitu photodegradation experiments further verified this as well. The $MAPbI_3$+PbI_2.NMP film illustrated the appearance of needle-like structures in film morphology upon illumination, which can be considered the result of the adduct formation during in situ AFM photodegradation. (Movie 4, Appendix 2 and Figure 13h). $MAPbI_3$+PbI_2.DMF film, on the other hand, had lost volatile species, which resulted in defects and accelerated photodegradation (For the comparison, see Movie 1-4, Appendix 2 and Figure 13a-h) [169].

Alternatively, Movies 1-4 can be accessed using the link: https://drive.google.com/file/d/1FAkhjbRRxfiF4Qzz7FBvCn5Evn85Cydc/view?usp=sharing

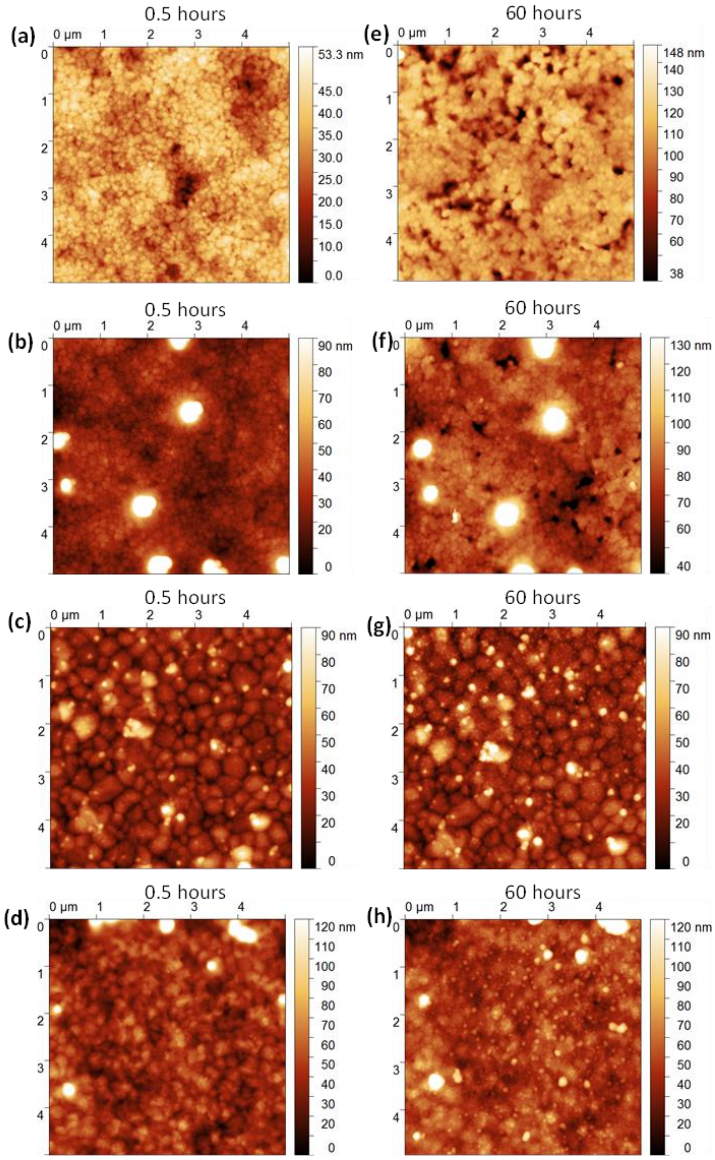

Figure 13 AFM images of $MAPbI_3$ thin films acquired as a result of in situ photo-degradation. (laser beam of 405 nm wavelength, with the light intensity of 10 kW m^{-2} was used). (a) fresh,0% excess PbI_2, from pure DMF. (b) fresh,10% excess PbI_2 from pure DMF (c) fresh, 0% ex cess PbI_2 from DMF/NMP mixture. (d) fresh,10% excess PbI_2 from DMF/NMP mixture. (e) aged,0% excess PbI_2, from pure DMF. (f) aged,10% excess PbI_2 from pure DMF (g) aged, 0% excess PbI_2 from DMF/NMP mixture. (h) fresh,10% excess PbI_2 from DMF/NMP mixture.[169]

Further investigation revealed that adducts between NMP and PbI_2 are favoured by the uniform distribution of valence states (Figure A2.4a and A2.4b, Appendix 2) in the accumulation with NMP's great coordination capacity with PbI_2. Furthermore, investigations have demonstrated that NMP sits near Pb sites in the PbI_2 lattice due to its ring-like structure and binds with lead atoms [195,202,208]. As a result of the strong intercalation of NMP with PbI_2, and due to low evaporation rates and good morphology, the adduct is more photodegradation resistant, improving the photostability of $MAPbI_3$+PbI_2.NMP film over $MAPbI_3$+PbI_2.DMF film[194,199,204].

4.1.3 Device performance and Device stability

Later, solar cells with excess PbI_2 addition were prepared by using co-solvent DMF/NMP. Perovskite solar cells were fabricated in n-i-p configuration Glass/ITO/ZnO/ PCBM/$MAPbI_3$ (with and without excess PbI_2)/ PTA/ MoO_x /Ag architecture. The PbI_2 concentration was varied from 5% to 15% by weight. The relevant fabrication steps are described in "3.2.3 Device preparation". A decent efficiency of 14.4 % was obtained by 10 % excess PbI_2 in the solution. This was almost double that of without excess PbI_2. In addition, excess PbI_2 improved open-circuit voltage, short circuit current densities and fill factor, thus increased overall solar cell performance. This improvement in photovoltaic parameters was associated with good morphology [203]. (Figure A2.5, Appendix 2)

Since the objective of this work was to check the influence on the photostability of solar cells, the operational stability of solar cells was also investigated. Solar cell devices based on $MAPbI_3$ using following configuration was fabricated: Glass / ITO / SnO_2 / $MAPbI_3$ / PTAA / MoO_x / Al. Here, the passivation layers are not used to avoid their impact on degradation dynamics. This will further allow monitoring the influence on photostability due to the excess PbI_2 and DMF/NMP cosolvent. However, skipping passivation layers often result in loss of performance [169]. Solar cell devices were made with 0 % and 15 % excess PbI_2 from pure DMF and the same from DMF/NMP mixture. These devices were

kept at 50℃ and exposed to light having power 50 mW/cm^2 inside a glovebox for 1500 h. (Figure A2.6, Appendix 2)

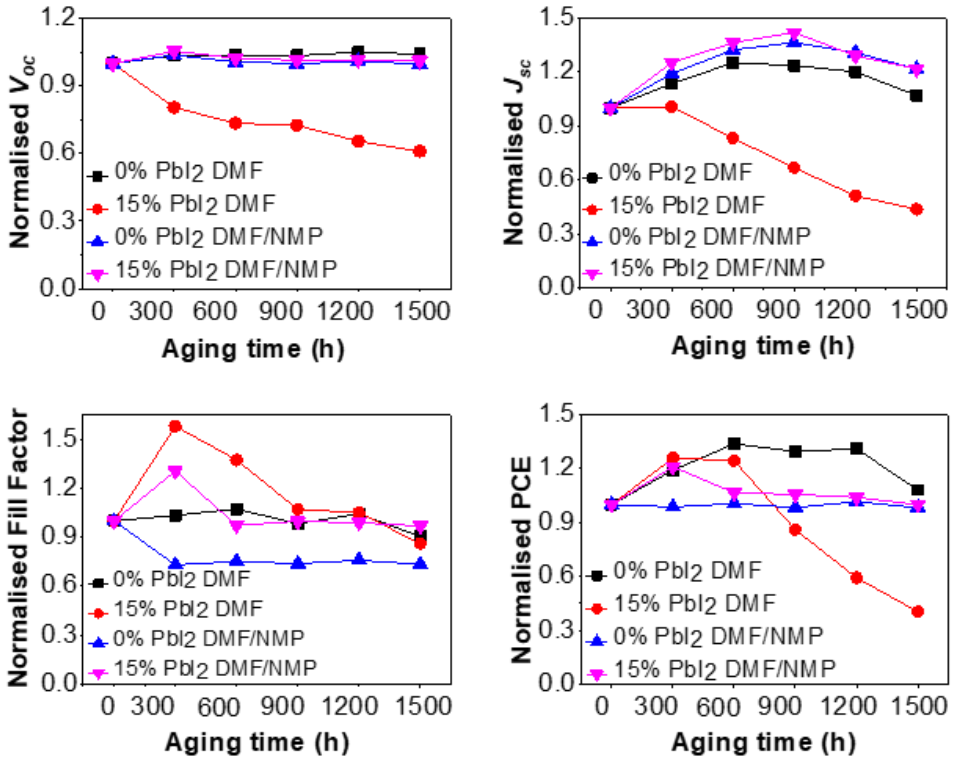

Figure 14 Device stability of solar cells made of $MAPbI_3$ with 0%, and 15% excess PbI_2, coated from pure DMF and DMF /NMP mixture. [169]

As shown in Figure 14, the solar cells with $MAPbI_3$+PbI_2.DMF are unstable and consistent with thin-film results. While solar cells with $MAPbI_3$+PbI_2.NMP remained fully functional. Thus, the presence of NMP co-solvent contributes to the improved photostability of PSC, while over stoichiometric PbI_2 is present in the $MAPbI_3$ frame.

4.2 Enhanced intrinsic photostability of $MAPbI_3$ thin films and solar cells with hydrazinium iodide

Hydrazinium iodide (N_2H_5I)is an inorganic salt additive. It has been reported that it can also act as an iodine quencher, reducing molecular iodine to iodide. Hence, the salt should be added in the perovskite framework [211–214]. Earlier reports showed that partial or full substitution of MA^+ cation using hydrazinium cation improved the efficiency and stability of solar cells, forming mixed cation perovskite [211].

However, exploring hydrazinium based salts as additives is another aspect. Hydrazinium halides are majorly investigated in the context of $FASnI_3$ based perovskite solar cells. For instance, a tiny amount of N_2H_5Br has been demonstrated to inhibit tin oxidation in $FASnI_3$ based perovskite solar cells and reduce defects and trap states in perovskites [215]. In the same way, adding N_2H_5Cl to $FASnI_3$ improved perovskite film morphology and crystallinity, yielding excellent power conversion efficiency [216]. Likewise, the addition of N_2H_5Cl to $MAPbI_3$ also improved PCE, coverage, quality and crystallinity of perovskite film due to intermediate formation with PbI_2 [181,217].

Following the idea, hydrazinium iodide (HAI) additive in $MAPbI_3$ is investigated. Further, its impact on the morphology, crystallinity, intrinsic photostability of thin-film, device performance and operational stability of solar cells was also studied [180].

4.2.1 Photostability of thin-films with HAI additive

The pristine $MAPbI_3$ film is defined as a reference $MAPbI_3$ film with 0% HAI. Similarly, $MAPbI_3$ film with 15% HAI is referred to as $MAPbI_3$+HAI. The photostability test was conducted inside a glovebox by illuminating perovskite films to 30 mW cm^{-2} using white LED light at 40 ℃ up to 1200 h. The white LED lamps had a similar spectrum to the solar

AM1.5G spectrum [183]. Further, UV-Vis and XRD were performed in regular intervals to check the intrinsic stability of films.

UV-vis test results revealed that the fresh, pristine $MAPbI_3$ film exhibits absorbance characteristics of perovskite ~750 nm. However, this absorbance feature of perovskite vanished after photoaging. Additionally, a shoulder matching to PbI_2 is visible ~500 nm (Figure 15), implying that pristine perovskite is unstable and degrades as suspected. In comparison, the absorbance characteristics of perovskite in fresh $MAPbI_3$+HAI film is observed ~750 nm, which remains very much visible even after 1200 h of photoaging. This indicates that adding HAI to the $MAPbI_3$ precursor improves its intrinsic photostability. However, a shoulder matching to PbI_2 was noticeable ~500 nm (Figure 15b).

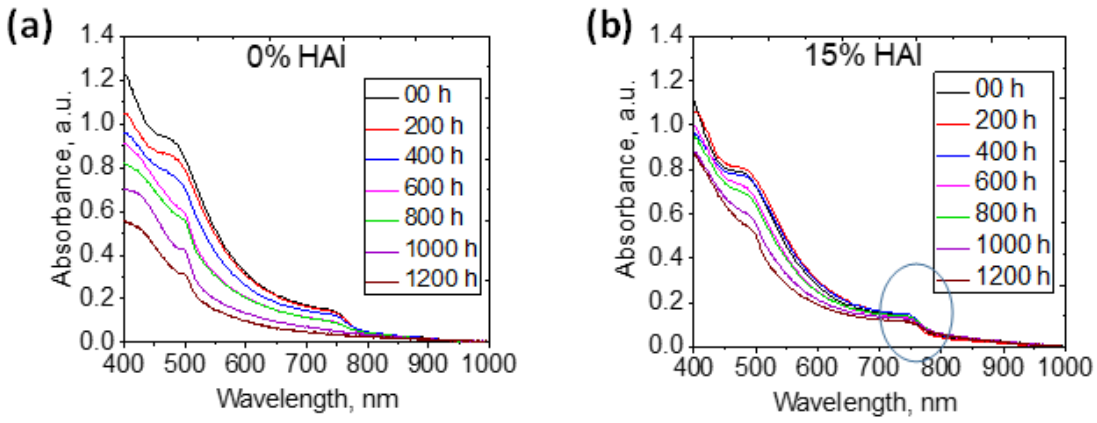

Figure 15 Evolution of the UV-Vis spectra of $MAPbI_3$ films (a) reference film with 0 % HAI.(b) $MAPbI_3$+HAI film. Ageing test conditions: White light:30 mW cm^{-2}, temperature: 40 °C, inert.

Simultaneously, the XRD patterns for fresh, pristine $MAPbI_3$ revealed less crystalline nature of the film with peaks located at 14.34°, 28.67°, 32.09°, 40.83°, 43.39° [218,219]. Further, these peaks related to the perovskite structure vanished with photoaging. Instead, at 12.80° and 31.40°, new peaks corresponding to PbI_2 and Pb emerged [218], showing perovskite deterioration. The fresh $MAPbI_3$+HAI film, on the other hand, displays a small

shift in the peaks that correspond to the perovskite structure with shifted peaks noticeable at 14.11°, 28.37°, 43.10°, and 58.61° [217,220]. Moreover, the fresh $MAPbI_3$+HAI film exhibits a more crystalline nature than the pristine film. Additionally, the peak intensity at 14.11° gets immensely intense (which becomes almost 100 times more than pristine) (Figure A2.7a, Appendix 2). Furthermore, a peak at 7.60° is observed due to an intermediate phase with PbI_2 that have peaks at 12.74°, 24.18°, and 25.58° [220,221]. Upon photoaging, the intermediate phase vanishes, while the PbI_2 peak becomes evident, with perovskite peaks slightly shifted to 14.14°, 28.42°, 43.19° and 58.71° after light soaking [222,223] and perovskite film exhibits the crystalline nature even after photoaging (Figure 16).

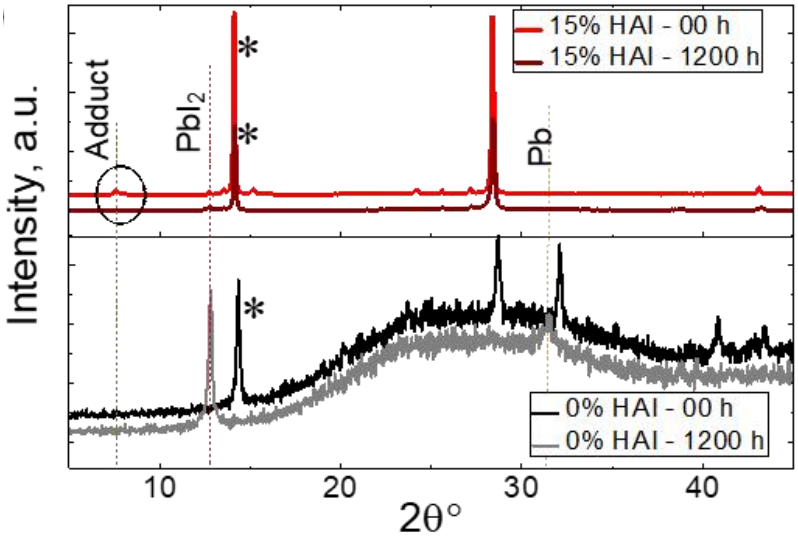

Figure 16 XRD patterns of fresh and aged $MAPbI_3$ (0% HAI) and $MAPbI_3$+HAI (15% HAI) films. * represents perovskite peaks.

Thus, The UV-Vis and XRD results confirm that adding HAI salt in $MAPbI_3$ does not destroy perovskite and improves intrinsic stability.

4.2.2. Proposed mechanism of improved stability with HAI salt

The XRD results suggest that the intermediate form between PbI_2 and HAI salt improves photostability. To gain a deeper insight, crystallinity, morphological, optical and FTIR characterisation were further investigated in correlation to intermediate formation.

The crystalline nature of a film is typically linked to a decrease in FWHM with an increase in peak intensity [224,225]. FWHM and crystallite size for pristine $MAPbI_3$ and $MAPbI_3$+HAI films were calculated following this concept. For the fresh state, the FWHM of pristine $MAPbI_3$ was 0.18° and dropped to 0.09° for $MAPbI_3$+HAI. After the photostability test, the FWHM of $MAPbI_3$+HAI showed less deviation with FWHM values as 0.10°. It should be noted here that the pristine $MAPbI_3$ degrades with photoaging. As a result, no perovskite phase was available; therefore, the FWHM value of photoaged $MAPbI_3$ is not comparable to photoaged $MAPbI_3$+HAI. The crystallite size is calculated using Scherer's equation [225] given as:

$$D=0.89\lambda/((\beta.Cos\theta)) \quad (11)$$

Where D represents average crystallite size, λ is the wavelength of X-ray (1.54 A°), θ is diffraction angle, and β is FWHM of the peak in XRD. The average crystallite size of the fresh, pristine $MAPbI_3$ film was observed 36 nm, which increased to 60 nm for $MAPbI_3$+HAI. After photoaging, the pristine perovskite was defragmented into lead iodide and lead. Therefore the average crystallite size for the photoaged pristine film was reduced to 23 nm compared to the fresh condition, which was determined using PbI_2 and Pb peaks as perovskite was defragmented. While the $MAPbI_3$+HAI film did not show any significant variation in the average crystallite size (50 nm). This indicates that HAI addition improves the crystallinity of perovskite film (Figure A2.7a and b, Appendix 2).

The improvement in crystallinity is connected to an improvement in grain size. Therefore SEM measurements were performed. The grain size of $MAPbI_3$+HAI was grown from 50-

150 nm (pristine $MAPbI_3$) to 400-1100 nm. The morphological changes showed that HAI addition resulted in a homogeneous film with flat and big grains passivating the grain boundaries, which can be caused by an intermediate phase between HAI and PbI_2 (Figure 17 a and b) [217]. The atomic ratio of I:Pb obtained using EDX measurements further validated this due to a higher value for $MAPbI_3$+HAI film over the pristine film (Figure A2.8, Appendix 2).

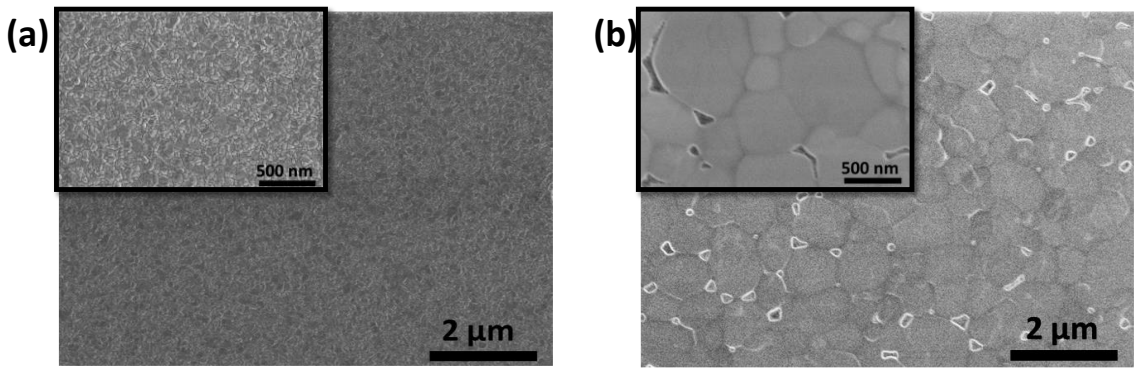

Figure 17 SEM images of (a) pristine $MAPbI_3$ film (0% HAI) (b) $MAPbI_3$ + HAI film (15% HAI).

As a result, photoluminescence peak intensities for $MAPbI_3$+HAI film exhibited a stronger peak intensity, implying that the HAI additive lowered non-radiative recombination losses at grain boundaries [213]. Furthermore, PL spectra indicated a peak shift from 767 to 753 nm (Figure A2.9a, Appendix 2), implying that the addition of HAI altered the bandgap of the perovskite layer, potentially increasing open-circuit voltages [215,181]. Additionally, the charge carrier recombination dynamics of $MAPbI_3$ film also changes with the κ factor of 0.6 for pristine $MAPbI_3$ to κ factor of 1.16 for $MAPbI_3$+HAI film; suggesting that HAI addition in $MAPbI_3$ influenced the recombination process that changed from free to bound for pristine to exciton-like recombinations for $MAPbI_3$+HAI film (Figure A2.9b and c, Appendix 2). This is linked with the reports suggesting that smaller grain size and non-radiative recombination losses lower the κ factor due to the disordered phase. On the other

hand, larger grains size result in an exciton-like transition at grain boundaries, implying an ordered phase and homogeneous perovskite layer [180,226,227].

Later, FTIR measurements/investigations confirmed the formation of an intermediate in the $MAPbI_3$+HAI film, which was believed to be the reason for the increased grain size. Peaks belonging to pristine perovskite are identified as C-H bend at 1380 cm^{-1} and 1470 cm^{-1}, weak N-H bend at1582 cm^{-1}, C-H stretch at 3030 cm^{-1} and N-H stretch 3133 cm^{-1} and 3180 cm^{-1} in pure $MAPbI_3$, which are consistent with the literature [217]. In the case of $MAPbI_3$+HAI, an additional N-H bend emerged at 1418 cm^{-1} in addition to the prominent N-H bend seen at 1565 cm^{-1} [217]. A tiny peak showing $N_2H_5^+$ deformation was also be seen at 1384 cm^{-1} [228]. Peaks of PbI_2 were found at 2360 cm^{-1}, 2924 cm^{-1} [229]. In addition, the N-H stretch got concentrated at 3136 cm^{-1}, while the NH_2 stretch related to N_2H_5I was observed at 3282 cm^{-1}[228]. These additional peaks point to the presence of an intermediate phase /complex formation of hydrazinium with lead iodide [217,228], which exhibited peaks of cubic $MAPbI_3$ at 1384 cm^{-1}, 1418 cm^{-1}, 1575 cm^{-1}, 1650 cm^{-1}, 3135 cm^{-1}, and 3178 cm^{-1} upon photoaging [217]; enhancing the intrinsic photostability of thin films. Further, these results are consistent with XRD and UV-Vis test outcome [180]. See Figure 18.

Thus, intermediate formation between PbI_2 and HAI improved crystallinity, grain size, and smooth morphology with passivating grain boundaries perceived to be the reason for the improved photostability of $MAPbI_3$+HAI film.

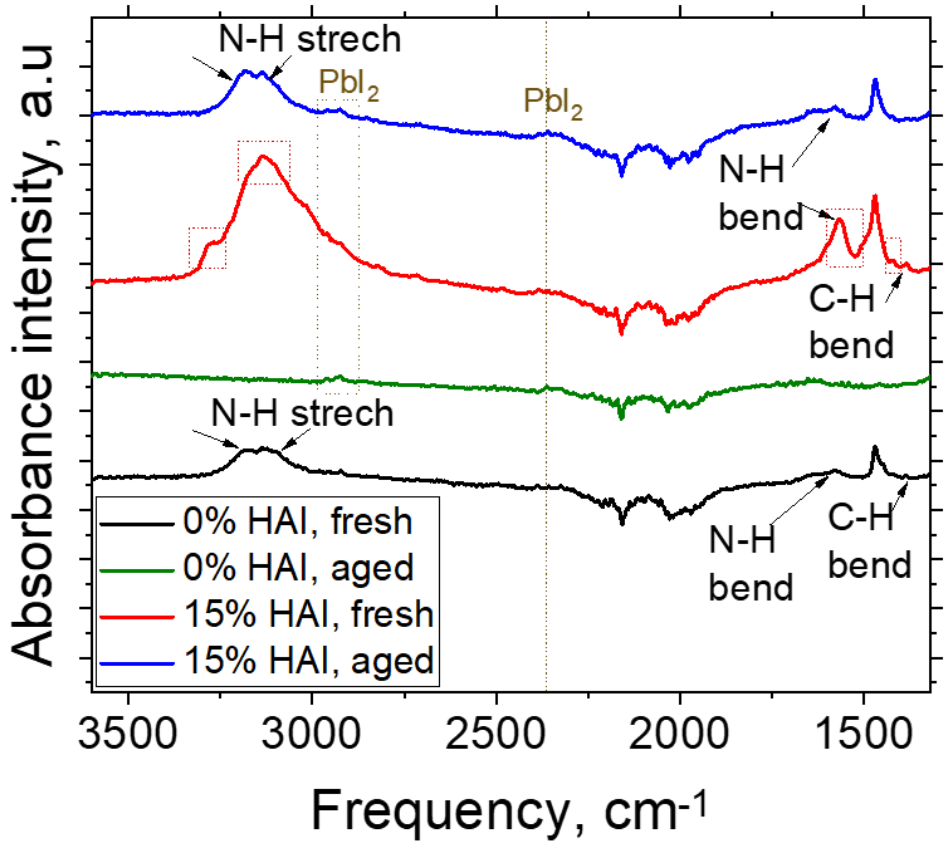

Figure 18 FTIR spectra of pristine and $MAPbI_3$+HAI films before and after photoaging test.[180]

4.2.3 Device performance and Device stability

To investigate the device performance of $MAPbI_3$ solar cell devices with HAI additive solar cells were fabricated in the n-i-p configuration in the following architecture Glass/ ITO/ SnO_2/ PCBA/ $MAPbI_3$/ PTA/ Polystyenere/ MoO_x/ Ag. Different HAI concentrations were employed in precursor as 0% (pristine), 0.5%, 1%, 2.5% and 5%, % by weight. Amongst which, 0.5% HAI addition showed the best PCE of 17.03% over pristine perovskite with 14.98%. Furthermore, V_{oc}, J_{sc}, and fill factor began to fall as HAI concentration rose above the optimum level (0.5%). Although the addition of 1% and 2.5 % HAI yielded in functional devices, the performance had reduced. The addition of 5%

HAI, on the other hand, ruined the performance of solar cells completely (Figure A2.10 a and b, Appendix 2). The best and average solar cell performance with respect to change in HAI concentration is shown in Table 16. According to reports, high current and open-circuit voltage are linked to increased crystallinity and grain size, resulting in improved charge transport characteristics [218,224,230,231]. As a result of the grain boundary passivation, the PCE was boosted up. On the other hand, excessive passivation might obstruct charge carrier transport and reduced device performance, as shown in the case of 5% and higher [180]

Table 16 HAI concentration vs IV parameters.[180]

HAI Content,%		$V_{oc,}$ mV	J_{sc}, mA cm^{-2}	Fill Factor	PCE, %
0	Best Avg	1040.67 1013.23±16.67	18.19 16.70±2.05	79.06 72.48±6.23	14.98 12.30±1.81
0.5	Best Avg	1058.13 1014.88±28.92	20.02 18.95±1.36	80.39 76.79±3.79	17.03 14.78±1.38
1	Best Avg	940.82 914.99±36.85	18.07 15.12±1.69	51.50 44.26±7.30	8.75 5.88±1.86
2.5	Best Avg	921.50 893.23±78.49	16.82 15.26±1.61	57.71 47.70±6.97	9.95 6.48±1.49
5	Best Avg	387.99 285.20	2.90 1.09±0.73	36.54 35.04±1.31	0.41 0.11±0.10

Further, the *J-V* characteristics of the best solar cell (with 0.5 HAI) exhibited reduced hysteresis over the pristine solar cell (Figure A2.11, Appendix 2). Reports suggest that in perovskite solar cells, the short circuit current hysteresis is induced by trap states present at the active layer interface that acts as a recombination centre [219]. Hence, reduced hysteresis is attributed to reduced recombination centres at the grain boundaries due to the high quality of the $MAPbI_3$+HAI film with enhanced crystallinity and larger grains, further resulting in improved fill factor [180,181,211,217].

Later, the operational stability of solar cells containing HAI additive was investigated. To do so, solar cells were fabricated in Glass/ITO/SnO_2/ $MAPbI_3$+HAI / PTAA/ V_2O_5/ Al configuration. For the operational stability test of solar cells, passivation layers like Phenyl-C_{61}-butyric acid (PCBA) and polystyrene were not used to minimise the influence on degradation dynamics. Unfortunately, without the passivation layers, the solar cell performance was reduced (Figure A2.12, Appendix 2). However, it allowed the photostability to be monitored associated with the active layer containing the HAI additive [232–235]. An optimum concentration of 0.5% was investigated for the photostability test. Solar cells were illuminated with white light with an intensity of 30 mW cm^{-2} at 40℃ for 1400 h. Afterwards, the entire set of devices was exposed to white light of the higher intensity of 60 -70 mW cm^{-2} at 50 ℃, from 1400 h till 4400 h. This experiment was performed inside the glovebox in an inert environment. After 4400 hours of constant illumination, the operational stability test revealed that reference solar cells containing pristine $MAPbI_3$ retained 60% of their initial efficiency. Solar cell devices containing 0.5% HAI maintained 80% of their initial efficiency, demonstrating that adding HAI improves the operational stability of $MAPbI_3$-based solar cells under light and heat. See Figure 19.

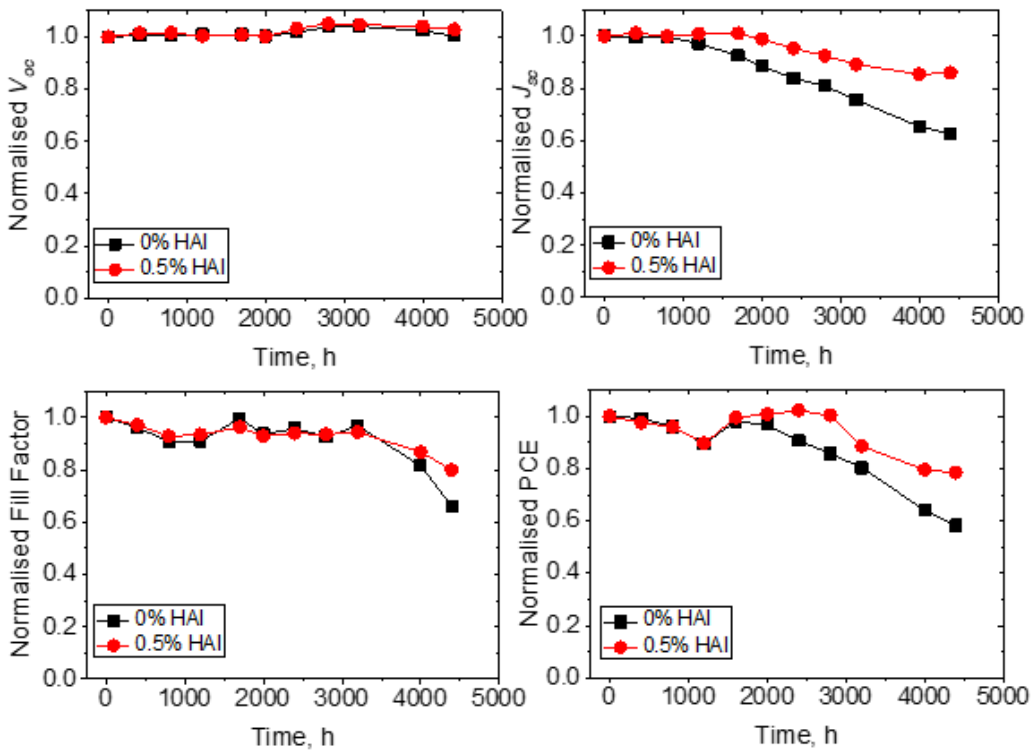

Figure 19 Operational stability of $MAPbI_3$ solar cells due to HAI additive.

Thus, enhanced/improved stability of $MAPbI_3$ film was achieved due to HAI incorporation $MAPbI_3$ in precursor solution [180].

4.3 Photostability of $MAPbI_3$ thin films with pyridine-based ligands

Pyridine based compounds are heterocyclic N atom-based compounds that are considered electron-deficient by nature. Furthermore, The N atom in pyridine derivatives has been demonstrated to be capable of interacting with Pb^{2+} defect sites as lewis base [27], while Pb^{2+} defects sites act as Lewis acid [236]. Because the N atom can undergo protonation and passivate defect sites as a chelating ligand, nitrogen-based chelating compounds are often used as passivation agents, which promote charge carrier transport [237–239]. Therefore, particularly, the main interest has been in studying the effects of pyridine derivatives as additives for the $MAPbI_3$ light-absorbing active layer in this experiment. Following the idea, bathophenanthroline (N1**)**, ϒ-bipyridyl (N2**)**, 4-hydroxy-1,10-phenanthroline (N3**)**, bathocuproine (N4**)**, oxyquinoline (N5) and 1,10 phenanthroline (N6**)** were investigated [44]. The chemical structures of these additives are shown in Figure 9, under the section "3.2 Materials".

4.3.1 Photostability of thin-films with pyridine-based ligands

The UV-vis results of fresh $MAPbI_3$ films illustrated that incorporation of additives in $MAPbI_3$ precursor resulted in the blue shift of the absorbance edge, altering the bandgap of the perovskite layer (Figure 20) [240]. The pristine $MAPbI_3$ displayed the absorbance feature of the perovskite phase ~750 nm. Whereas the absorbance feature of perovskite vanished for $MAPbI_3$+N1 and a small edge/bend appeared ~692 nm. $MAPbI_3$+N2 depicted the absorbance feature ~745 nm and maintained the perovskite phase. However, $MAPbI_3$+N3 and $MAPbI_3$+N4 badly affected the perovskite structure, and absorbance feature corresponding to the perovskite phase, similar to N1**,** was not observed. Whereas $MAPbI_3$+N5 and $MAPbI_3$+N6 displayed absorbance features of perovskite formation, those were found ~730 nm and ~736 nm, respectively (Figure 20a). Similarly, the blue

shift was noticed for PL emission peaks upon the addition of N1-N6, with the reduction in peak intensity compared to pristine (except for N6) (Figure 20b).

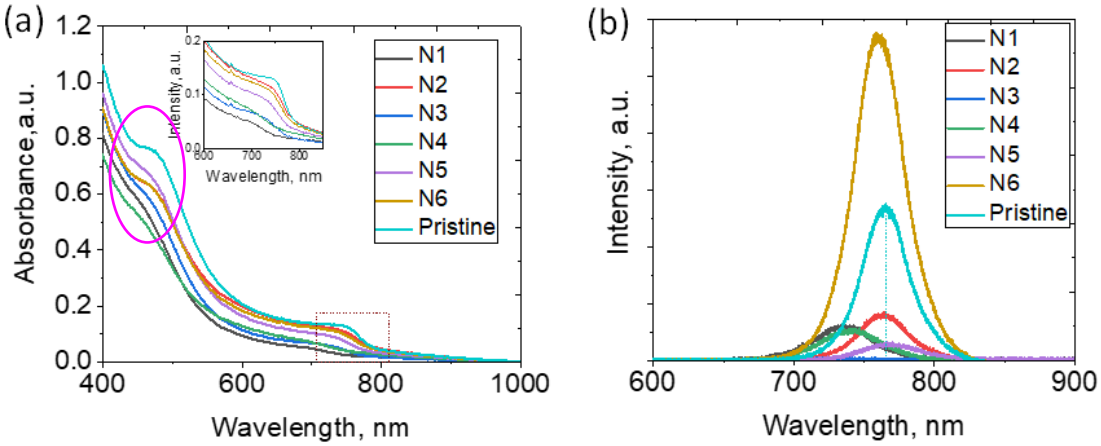

Figure 20 (a) UV-vis absorption (b) PL emission peaks of pristine $MAPbI_3$ and $MAPbI_3$ with additives (N1-N6).

Further, the XRD analysis was done. The XRD of fresh, pristine $MAPbI_3$ film showed patterns consistent with the cubic structure/phase of $MAPbI_3$ (Figure A2.13, Appendix A2) [241]. However, XRD patterns of $MAPbI_3$+N1 displayed deformation in the peak corresponding to the perovskite phase, and peak intensity was weakened drastically than pristine $MAPbI_3$, implying the loss of crystalline nature of the film. On the contrary, XRD of $MAPbI_3$+N2 exhibited peak splitting at 14.02˚ and 14.2˚, peaks matching the perovskite structure, signifying the phase transition of $MAPbI_3$ [242]. Further, smaller and broader XRD peaks reflecting the perovskite structure were observed in the case of $MAPbI_3$+N3, which was found to be somewhat displaced compared to pristine $MAPbI_3$ [242,243]. Whereas the addition of N4 showed similar behaviour as the addition of N1, illustrating the deformity of the perovskite structure. $MAPbI_3$+N5 and $MAPbI_3$+N6 show similar XRD patterns related to $MAPbI_3$ perovskite (Figure A2.13, Appendix A2) [44,242,244]. Table 17 summarises

UV-vis, PL, and XRD observations performed on fresh $MAPbI_3$ samples containing additives N1-N6.

Table 17 Comparision of UV-vis, PL and XRD observations for the fresh $MAPbI_3$ +additive (N1-N6) films[44]

Additive in $MAPbI_3$	UV-vis peak position of $MAPbI_3$	PL peak position of $MAPbI_3$	XRD peak position of $MAPbI_3$
Pristine	750 nm	767 nm	14.1˚, 28.4˚, 31.9˚
N1	692 nm (peak diminished)	734 nm	peak diminished
N2	745 nm	764 nm	14.02˚,14.2˚, 28.4˚, 31.9˚,
N3	710 nm	723 nm	13.9˚,14.3˚, 28.6˚, 32.0˚
N4	690 nm (peak diminished)	746 nm	peak diminished
N5	730 nm	766 nm	14.02˚,14.2˚, 28.4˚, 31.8˚
N6	736 nm	758 nm	14.02˚,14.2˚, 28.4˚, 31.8˚

Next, all samples were subjected to a photostability test which was performed in a specially designed degradation chamber integrated inside the glovebox with an inert atmosphere. Finally, samples were exposed to the continuous light illumination of intensity 70-80 mW cm^{-2} around 50-60 ℃ for 1400 h [183].

Despite the fact that the perovskite structure had already been damaged by adding N1 to the $MAPbI_3$ precursor, the UV-vis evolution of the $MAPbI_3$+N1 film showed negligible modifications after photoaging for 1400 hours (Figure 21a). The XRD pattern also supported this (Figure 21b). That is why N1 could not be taken as an ideal additive for $MAPbI_3$ stabilisation. While, the UV-vis evolution of $MAPbI_3$+N2 films revealed that the absorbance feature of the perovskite structure was noticeable even after 1400 hours of photoaging, signifying that adding N2 to the $MAPbI_3$ precursor maintains the stability of the $MAPbI_3$ thin film (Figure 21c). This stability could be mainly as a result of a complex

between PbI_2 and N2 [245,246], which will be expressed later in the section of "4.3.2 Proposed mechanism of improving stability with N2". Also, the XRD pattern at 14.02 of the photoaged film verified the perovskite structure (Figure 21d). Nevertheless, the peak intensity was reduced. Further, N3 and N4 exhibited the same behaviour as N1 (Figure 21e-h). In the case of $MAPbI_3$+N5 film, however, the absorbance feature of the perovskite vanished after photoaging (Figure 21i), the only a shoulder observed ~500 nm, representing the disintegration of perovskite to PbI_2. Later, XRD patterns of the photoaged $MAPbI_3$+N5 film displayed peaks at 12.6˚ and 31.1˚, matching PbI_2 and Pb, respectively (Figure 21j) [247]. Similarly, $MAPbI_3$+N6 also showed Pb formation and indicated that N6 addition did not improve $MAPbI_3$ photostability (Figure 21k-l). While pristine $MAPbI_3$ decomposed to PbI_2 and Pb as suspected [25] (Figure 21m-n).

Thus, the thin film photostability test concluded that ϒ-bipyridyl (N2) improved the intrinsic photostability of $MAPbI_3$ film and $MAPbI_3$+N2 film was able to sustain illumination for 1400 h while the pristine film degraded. In contrast, bathophenanthroline (N1) deformed perovskite features of the active layer. Therefore it was not considered a suitable additive in the context of the photovoltaic application. Likewise, 4-hydroxy-1,10-phenanthroline (N3**)** was not considered as well.

N1 (a) (b)

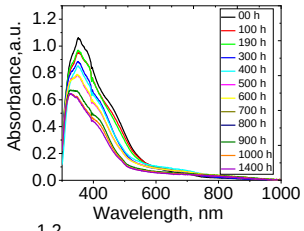

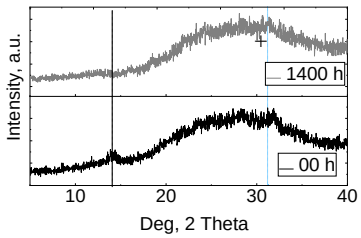

N2 (c) (d)

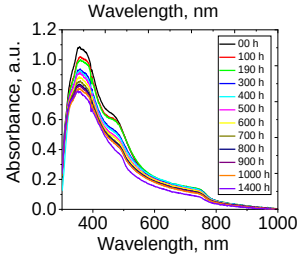

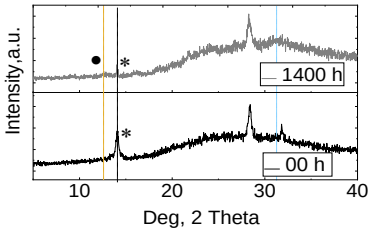

N3 (e) (f)

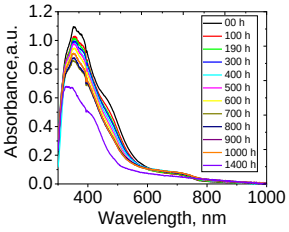

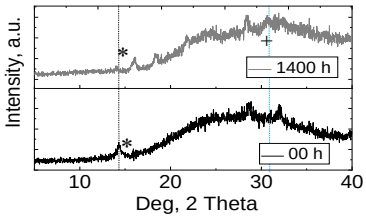

N4 (g) (h)

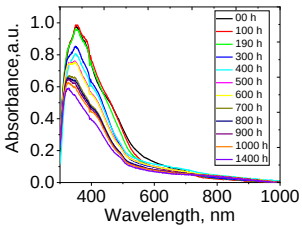

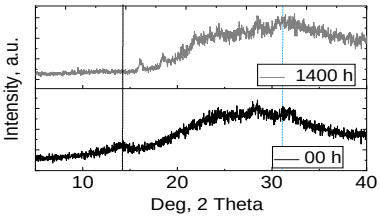

N5 (i) (j)

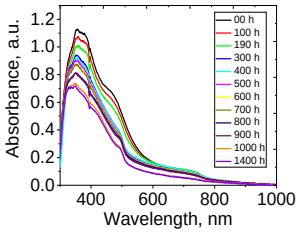

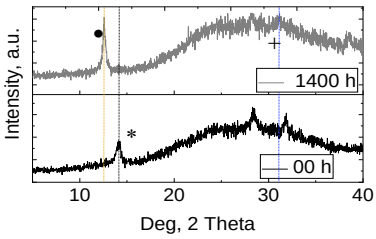

N6 (k) (l)

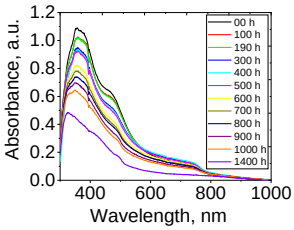

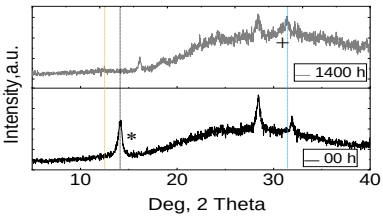

Pristine $MAPbI_3$ (m) (n)

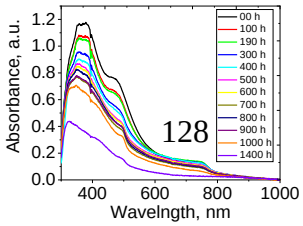

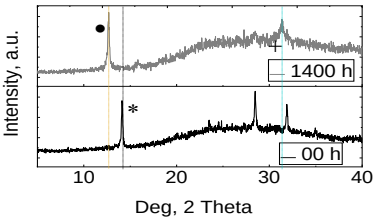

Figure 21 Evolution of UV-vis and XRD patterns of $MAPbI_3$+N1 (a,b), $MAPbI_3$+N2 (c,d), $MAPbI_3$+N3 (e,f), $MAPbI_3$+N4 (g,h), $MAPbI_3$+N5 (I,j), $MAPbI_3$+N6 (k,l) and pristine $MAPbI_3$ (m,n) respectively.* presents perovskite,· presents PbI_2 and +presents Pb.

4.3.2 Proposed mechanism of improved stability of $MAPbI_3$ film with ϒ-bipyridyl (N2)

Since it is known that the Pb^{2+} sites in $MAPbI_3$ act as Lewis acid, electron-deficient nitrogen-based heterocyclic compounds behave as lewis bases and their coordination results in lewis acid-base adduct.[248,249]. Hence, the complex formation between PbI_2 and N2 is expected. Therefore to further, monitor the effect of the additive on the $MAPbI_3$ surface and morphology, AFM studies were performed.

The AFM images of pristine $MAPbI_3$ showed an inhomogeneous surface with more significant clusters (Figure 22a). On the contrary, AFM images of $MAPbI_3$+N2 resulted in a homogeneous dense compact small granular like structure (Figure 22b). Although there are morphological differences in pristine $MAPbI_3$ and $MAPbI_3$+N2 films, yet the RMS roughness is similar. Upon photoaging, the pristine $MAPbI_3$ film shows pinholes, indicating the photodegradation of the perovskite structure (Figure 22c). On the other hand, $MAPbI_3$+N2 shows the growth of needle-like structure (the brightest spots in Figure 22d), indicating the formation of a new complex that might have taken place and resulted in enhanced photostability of thin-film (Figure 22d).

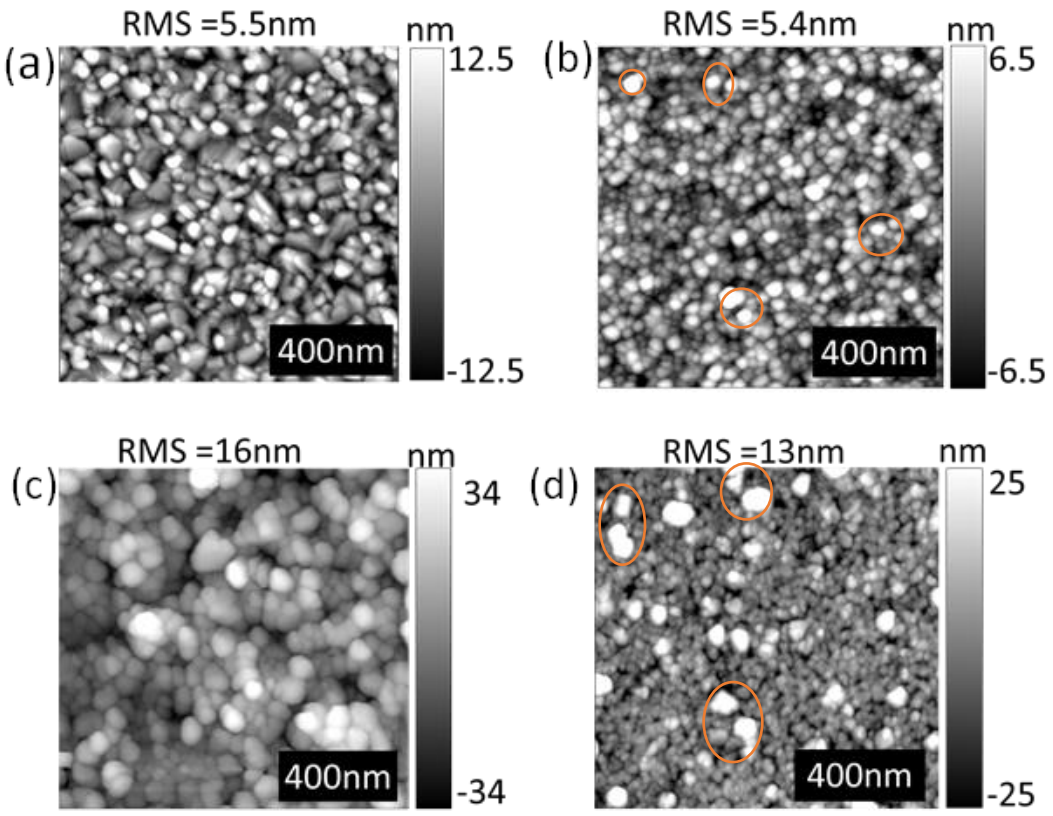

Figure 22 AFM images (a) fresh pristine $MAPbI_3$ film. (b) fresh $MAPbI_3$+N2. (c) photoaged pristine $MAPbI_3$ film (d) photoaged $MAPbI_3$+N2.[44]

Further, PL spectra of pristine and $MAPbI_3$+N2 samples were measured. (Figure A2.14, Appendix A2). The PL peak intensity suggests that fresh, pristine $MAPbI_3$ had a higher PL peak intensity over $MAPbI_3$+N2, implying that N2 might result in more non-radiative losses that could cause a reduction in open-circuit voltage and fill factor [243]. However, upon photoaging, the PL emission peak for pristine $MAPbI_3$ became extinct, whereas the emission peak intensity for $MAPbI_3$+N2 turned out to be higher than the fresh stage. In addition, the PL emission peak of $MAPbI_3$+N2 displayed a further blue shift upon photoaging which could be attributed to complex formation upon N2 addition in $MAPbI_3$

[250]. Finally, FTIR spectroscopy was performed to investigate the complex formation (Figure 23).

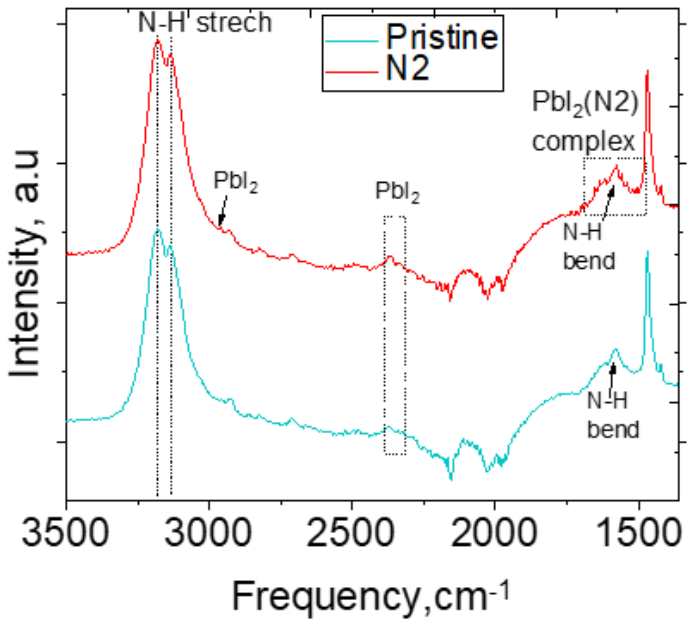

Figure 23 FTIR spectra fresh $MAPbI_3$ and $MAPbI_3$+ N2 film

The FTIR spectra of pristine $MAPbI_3$ exhibited peaks analogous to perovskite structure at 1468 cm^{-1} and 1580 cm^{-1} (N-H bend), 2926 cm^{-1} (C-H bend), and 3136 cm^{-1} and 3175 cm^{-1} (N-H stretch), consistent with the literature.[241] Whereas, for $MAPbI_3$+N2, the N-H bend was found to be shifted at 1466 cm^{-1} and 1573 cm^{-1}. Also, many minor peaks emerged ~ 1573 cm^{-1}, suggesting the formation of a new complex which is attributed to the PbI_2(N2) complex.[250,251]. In addition, a minor peak of PbI_2 appeared ~2965 cm^{-1} in conjunction with C-H stretch ~ 2925 cm^{-1}. The peaks corresponding to the N-H stretch were also noticed to be shifted at 3130 cm^{-1} and 3178 cm^{-1} because of PbI_2(N2) complex formation. The peak corresponding to complex formation was attributed to a minor ring stretch at 1436 cm^{-1}, 1490 cm^{-1} and 1573 cm^{-1} [250]. The peak at 1557 cm^{-1} was ascribed to N2 [250], shown in the

zoomed version of FTIR spectra (Figure A2.15, Appendix 2). Besides, this complex formation explains the reduction and shift of absorbance edge near 500 nm attributed to PbI_2 [246] (Figure A2.16, Appendix 2). This complex formation later results in improved stability of $MAPbI_3$+N2 thin film (Figure A2.17, Appendix 2).

Additionally, in an attempt to correlate material structure properties with improvement in the photostability, the following has been observed:

Table 18 A Summary of all pyridine derivates investigated as additives in $MAPbI_3$

Stability

Additive	Empirical formula	Molecular weight (g/mol)	Melting point (°C)	Comment	Structure
bathophenanthroline (N1)	$C_{24}H_{16}N_2$	332.40	218 - 222	Improves stability but destroys perovskite features	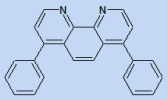
γ-bipyridyl (N2)	$C_{10}H_8N_2$	156.19	111.0	Improves stability and does not destroy perovskite features	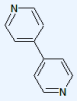
4-hydroxy- 1,10-phenanthroline (N3)	$C_{12}H_8N_2O$	196.20	214-215	Improves stability but destroys perovskite features	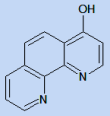
bathocuproine (N4)	$C_{26}H_{20}N_2$	360.460	283	Improves stability but destroys perovskite features	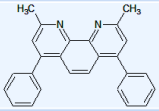
oxyquinoline (N5)	C_9H_7NO	145.16	76	Does not destroy perovskite features but decreases stability	
1,10 phenanthroline (N6)	$C_{12}H_8N_2$	180.21	118.56	Does not destroy perovskite features but decreases stability	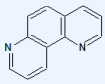

Additives with lower molecular weight (N2, N5 and N6) do not destroy perovskite structure (observed both in UV-Vis results and XRD patterns as shown in Figure 20a and Figure A2.13, Appendix A2). On the other hand, additives with higher molecular weight (N1, N3 and N4) are observed to destroy the perovskite structure. Furthermore, it is also

noticed that $MAPbI_3$ films with additives having a lower molecular weight (N2, N5 and N6) show less shift in absorbance feature in the region of 450 – 550 nm over pristine perovskite. The absorbance feature at 500 nm is known to be associated with PbI_2. The shift in absorbance feature in the 450 - 550 nm region is due to the complex formation with PbI_2. For the additives with higher molecular weight (N1, N3, and N4), the absorbance feature in the region 450-550nm disappears, indicating strong interaction with PbI_2 and additives (N1, N3 and N4), resulting in complex formation with PbI_2, which upon photoaging remains stable. Unfortunately, the complex formation of PbI_2 with higher molecular additives (N1, N3 and N4) results in loss of perovskite absorbance feature near 750 nm (Figure 20a), which suggests that N1, N3 and N4 are not ideal candidates here as it is suspected that these additives will cause loss of optoelectronic properties, which is a must-have feature for solar cell devices. Out of N2, N5 and N6, the complex formation of PbI_2 with N5 and N6 is less stable against illumination than N2. Thus, comparing overall, the complex formation of PbI_2 with N1, N2, N3 and N4 are more stable against illumination over N5 and N6. However, Since the complex formation between PbI_2 and N2 does not destroy the perovskite absorbance feature (Figure 20a), N2 is considered an ideal candidate and investigated further.

4.3.3 Device performance with additive Ɣ-bipyridyl (N2)

Since $MAPbI_3$+N2 showed enhanced intrinsic photochemical stability, the additive was further investigated in solar cell devices in n-i-p configuration (Figure 24a). Concentration of N2 was varied from 0.0% (pristine), 0.5%, 1%, 2.5%, 5% to 7.5%, % by weight. The IV parameters are shown in Figure 24b. Unfortunately, the addition of N2 reduced PCE slightly (15.4%) compared to pristine (16.9%). The best and average device performance with various concentrations of $MAPbI_3$+N2 is presented in Table A1, Appendix 2. The small drop in PCE was due to lower V_{oc} and fill factor, which could be attributed to more

non-radiative losses [240]. However, using excess PbI_2 [185] or facilitation of charge transport by additional layers can be further applied in combination with N2 to achieve higher PCE and is subject to further investigation and optimisation.

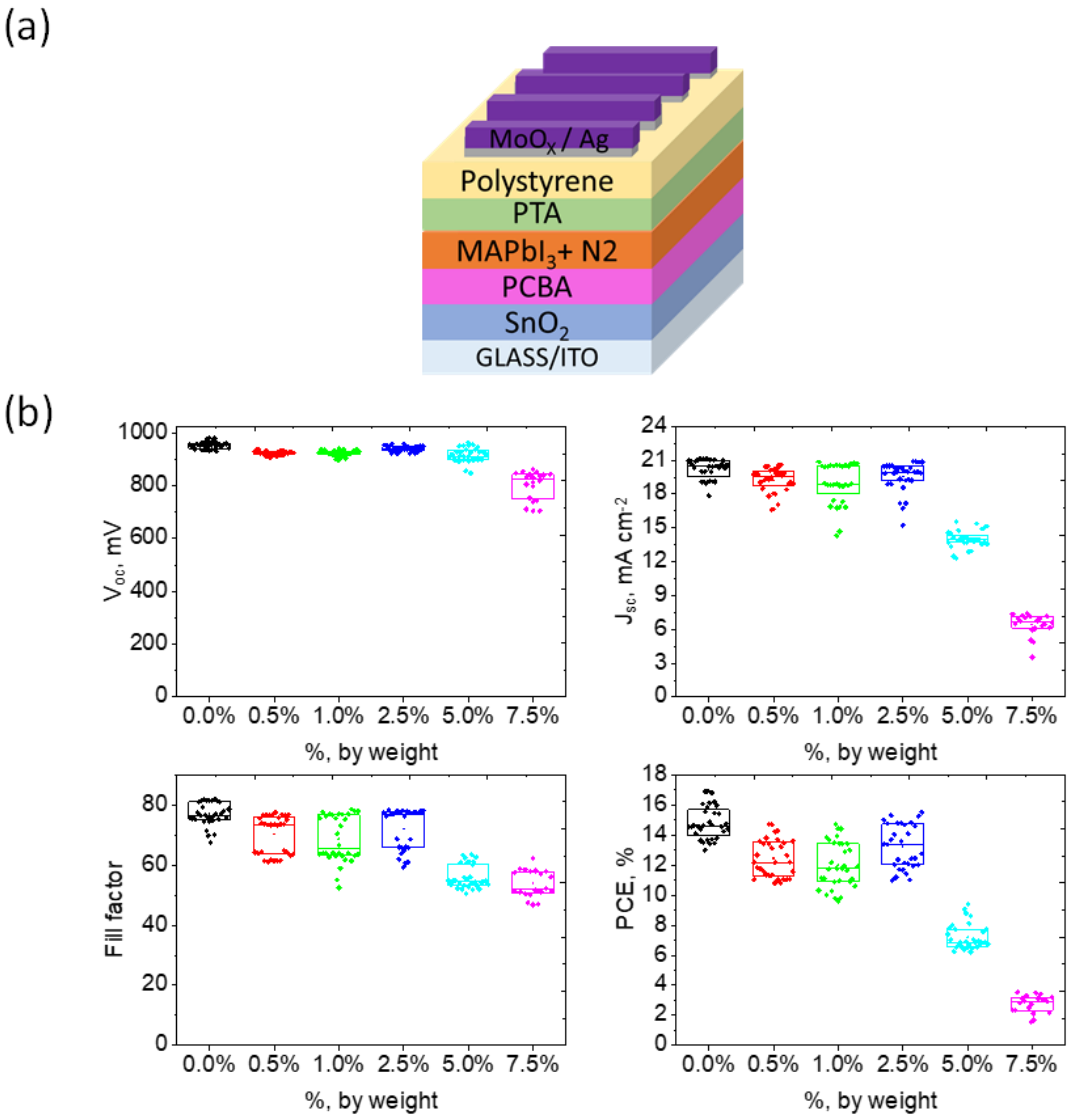

Figure 24 (a) device architecture (b) Impact of the addition of N2 onto photovoltaic parameters.

Further, the hysteresis factor was calculated for the optimum concentration (2.5%) and compared with pristine, presented in Figure 25 and Table A2, Appendix 2. The hysteresis factor (HF) was calculated with the formula reported elsewhere [252] :

$$\text{Hysteresis factor} = \frac{\text{PCE(reverse)-PCE(forward)}}{\text{PCE (reverse)}}$$

Based on J-V and hysteresis parameters, it was observed that the performance of $MAPbI_3$+N2 is comparable to pristine. Hence, $MAPbI_3$+N2 can be utilised in photovoltaic applications.

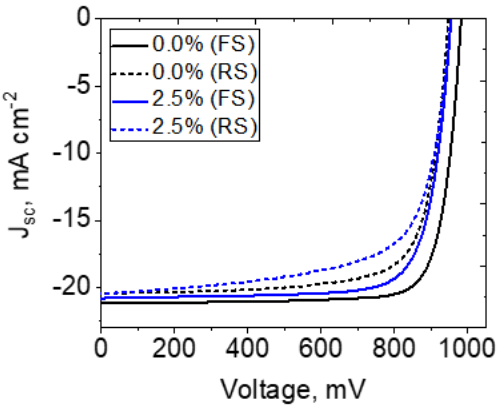

Figure 25 J-V curves of pristine vs 2.5% (best PCE) of N2 in $MAPbI_3$

In a nutshell, the addition of ϒ-bipyridyl (N2) improves the photostability of $MAPbI_3$ thin films and shows a decent comparable performance. However, the device stability test is a further prospect of investigation in this case.

5. Conclusions and Prospects

In the scope of this thesis, selection criteria for choosing additives for the $MAPbI_3$ active layer have been presented, which was absent otherwise. Earlier, reports often lacked to answer- how a particular additive was selected for further investigations? Therefore, it was an absolute necessity to classify the reported additives and develop a selection criterion. Following this, earlier reported additives were classified based on organic and inorganic additives. The organic additives were later subcategorised based on N donor atom, O donor atom and S donor atom mainly with the associated functional group. Inorganic additives were subcategorised based on the group in the periodic table. Following the same notion, twenty-three additives were primarily investigated during this work. Both inorganic salts and organic additives were chosen to explore their influence on the intrinsic photostability of $MAPbI_3$. Organic additives were further chosen based on their functional groups as pyridine derivatives, acids, esters, ethers and others. The initial results obtained from the UV-Vis measurements showed that eight of the additives exhibited improved intrinsic stability of thin films. Out of which, three additives were studied in detail. These three additives are (Lead iodide) PbI_2 with NMP, hydrazinium iodide (N_2H_5I/HAI) and ϒ-bipyridyl. For which, the conclusions are:

- The photostability in the presence of over stoichiometric lead iodide is correlated with the choice of the correct solvent formulation. In this case, the addition of NMP co-solvent improved the photostability of $MAPbI_3$ thin films while excess PbI_2 content is present in the active layer. According to the findings, the NMP cosolvent forms an adduct with Pb atoms, which inhibited destabilisation of the $MAPbI_3$ layer due to excess PbI_2 content, leading to improved stability against illumination in an inert atmosphere. Later by employing NMP cosolvent with 10% excess PbI_2, an improved PCE of 14.4% was obtained. Moreover, by incorporating NMP as a co-

solvent into the precursor and combining it with over stoichiometric PbI_2, photostable solar cell devices with a lifetime of up to 1500 hours were acheived.

- In the case of N_2H_5I additive, the incorporation of N_2H_5I into $MAPbI_3$ precursor improved the crystallinity of film, showed the grain size growth with homogeneous film morphology, resulting in grain boundary passivation. Further, these morphological improvements in the film were ascribed to intermediate formation between N_2H_5I and PbI_2. This intermediate formation slowed down the degradation process and thin-film sustained illumination for up to 1200 h, after which the intermediate phase changes to the cubic phase of $MAPbI_3$. To add on, incorporating an optimum amount of N_2H_5I demonstrated improved power conversion efficiency of 17.03% and operational stability of ~80% (of the initial stage) after 4400 h of continuous illumination in an inert environment.
- Similarly, ϒ-bipyridyl in perovskite precursor resulted in improved stability of thin-film, sustaining illumination for 1400 h under an inert atmosphere that was perceived due to the presence of complex formed between ϒ-bipyridyl and PbI_2. However, incorporation of ϒ-bipyridyl resulted in comparable performance (15.4%) to pristine one.

The highest operational stability in completed solar cell devices was demonstrated by the N_2H_5I additive (4400 h). In comparison, PbI_2 with NMP demonstrated operational stability of solar cells up to 1500 h only. The higher operational stability due to N_2H_5I over NMP+PbI_2 could be because of the intermediate formation between N_2H_5I and PbI_2, which disappears upon photoaging and delays perovskite degradation. Another possible reason could be that the formed adduct between NMP and PbI_2 is weak compared to the adduct/intermediate phase of PbI_2 with N_2H_5I against illumination. However, a further experimental investigation would require comparing adducts with PbI_2 and NMP to intermediate between PbI_2 and N_2H_5I.

When compared to the current state of the art, the highest reported stability of perovskite solar cells is more than 10000 h (~ 1 year) due to 2D/3D aminovaleric acid iodide ($HOOC(CH_2)_4NH_3)_2PbI_4$)/$CH_3NH_3PbI_3$ perovskite junction. (2D/3D perovskite junction results in a mixed cation perovskite layer, which is not pure $MAPbI_3$). The configuration used was FTO/c-TiO_2/mp-TiO_2/ZrO_2(5-AVA)$_x$(MA)$_{1-x}PbI_3$/Carbon. However, compared to a pure $CH_3NH_3PbI_3$ based active layer, the obtained result of 4400 h with N_2H_5I addition stands at the top position to improve intrinsic photostability and the highest number of days of operational solar cells, as shown in Figure A0.18, non-metal additives, Appendix 0. It should be emphasized here that in this thesis, PSCs performance and operational stability tests were done in n-i-p configuration. It is known that n-i-p configuration results in slightly higher efficiency over p-i-n configuration. Moreover, SnO_2 was used as ETL, PCBM /PCBA was used as passivation layers, and PTA or PTAA as HTL. These materials are standard in the perovskite fabrication procedure, with an effect known on the performance and stability of $MAPbI_3$ PSC. Therefore, it can be predicted that if p-i-n configuration is used with standard materials such as PTAA as ETL, the efficiency might be slightly lower. The stability of the perovskite layer associated with additive incorporation would be similar to the thin-film stability tests. (Incase of PTAA as HTL in p-i-n configuration devices will exhibit similar trend of operational stability but incase of PEDOT:PSS device probably will exhibit poor stability due to poor stability of PEDOT: PSS layer itself). It is known fact that a change of charge transport layer might affect stability. It should be noted that charge transport layers also play a vital role in the stability of a complete solar cell device. However, not only does the perovskite active layer suffer poor intrinsic issues, but the charge transport layer also suffers stability problems. Therefore, new charge transport layers (effect of which is unknown on the stability of solar cell) might be further tested to investigate their impact on performance and stability in the presence of an additive, following the similar approach as mentioned in this thesis.

A further expansion of this thesis work would involve theoretically monitoring the influence of additive incorporation on the electronic properties such as band structures, the density of states using density functional theory (DFT). The obtained theoretical results shall further be compared with experimental investigation of electronic properties. Experimental results can be obtained by using either of the techniques, such as angle-resolved photoemission spectroscopy (ARPES), electron energy loss spectroscopy (EELS), Ultraviolet photoelectron spectroscopy (UPS) and Scanning tunnelling spectroscopy (STS). In addition, the effect of additives on the semiconducting nature of perovskite should be explored. Measurements of hole and electron mobilities and diffusion lengths will reveal information about the semiconducting characteristics of the perovskite layer after additive inclusion. Charge transport measurements shall also be investigated those are usually performed using a space charge limited current model (SCLC). Furthermore, changes in the crystal structure of the $MAPbI_3$ perovskite due to additives showing stabilization effect must be studied theoretically and experimentally in detail. This will allow correlating theoretical and experimental studies to establish structure-property relationships, which can be useful to associate additive influence on intrinsic stability.

Apart from the mentioned above, it should be noted that the typical donor atom in these additives showing the stabilising effect is the N atom. The cosolvent NMP in the case of PbI_2 additive, the additives hydrazinium iodide and ϒ-bipyridyl, all of these compounds are amine derivatives. However, NMP does contain the carbonyl group but is considered an amine derivative due to its Nitrogen-containing ring-like structure. Therefore, it is suggested that compounds containing amines can play a crucial role in overcoming the intrinsic photostability issues associated with $MAPbI_3$. Further, researchers should focus on designing new amine containing additives.

A future prospect in the broad area of additive investigation should focus on developing an artificial intelligence-based system/ machine learning/ depository to compare the

morphological and optoelectronic properties with the molecular structure of investigated additives and their influence on photostability in given conditions since there was no proper rule to select the correct/suitable material to achieve stabilization effect until now. Therefore it is the need of the hour to design a tool to perform systematic statistical investigation. This, in turn, will help researchers to select materials to design new additives to stabilize $MAPbI_3$. Although newly designed additives would also require a further experimental investigation in practical terms. The bright side of having an artificial system is that researchers will be able to see all of the information required to develop a more rational design of additives. At the same time, it must be noted that the enumeration approach (i.e. thin film and device stability test) will still be the key to verify additive influence on the stability of the perovskite layer. Information from the artificial intelligence-based system can be used to design new additives, and experimental investigation of newly designed additives should be followed in the sequence as shown in Figure 26. An internationally recognised depository should be created for the research community to follow such steps shown in Figure 26, which would provide at a glance updated information to researchers and scientists for a deep, comprehensive exploration of the physical and chemical phenomena because the artificially intelligent system would be limited to only widely screen for a few defined parameters. Therefore, artificial intelligence systems should be limited to collecting information for material structure properties and their effect on stability, which should be available for human comprehension, ultimately leading to a more rational design of additives.

Another prospect in additives investigation is that additives should also be examined on large-area devices. Currently, the majority of research reports are based on small area devices. Nevertheless, large-area devices will be required for commercial purposes. However, morphology, performance, distribution of surface defects, grain size, and trap states will be changed when the large area is used. Therefore, the fabrication of large-area devices using additives is another prospect that requires high PCE and stability to achieve.

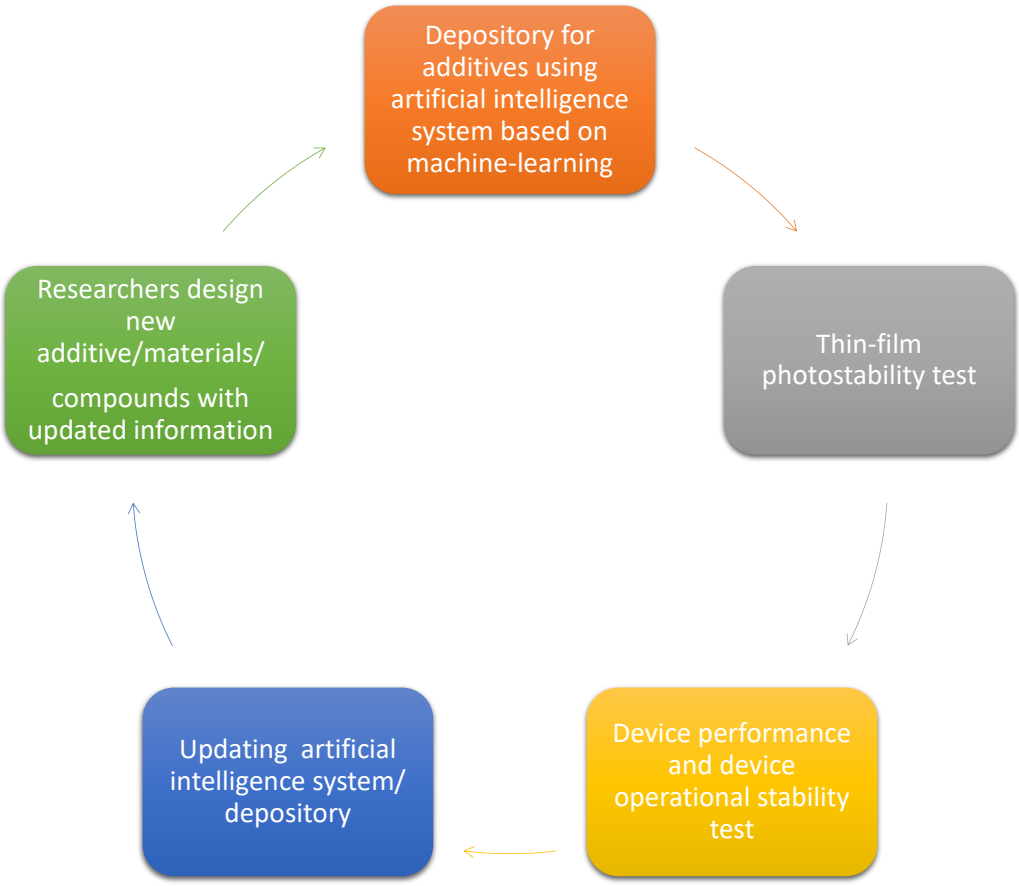

Figure 26 Additive investigation using artificial intelligence system based on machine learning/depository, combined with enumeration approach

6. BIBLIOGRAPHY

1 EIA projects nearly 50% increase in world energy usage by 2050, led by growth in Asia - Today in Energy - U.S. Energy Information Administration (EIA), https://www.eia.gov/todayinenergy/detail.php?id=41433, (accessed 1 November 2020).

2 O. Ellabban, H. Abu-Rub and F. Blaabjerg, *Renew. Sustain. Energy Rev.*, 2014, 39, 748–764.

3 File:Global Energy Potential 2014 08 09.svg - Wikimedia Commons, https://commons.wikimedia.org/wiki/File:Global_Energy_Potential_2014_08_09.svg, (accessed 1 November 2020).

4 G. M. Wilson, M. Al-Jassim, W. K. Metzger, S. W. Glunz, P. Verlinden, G. Xiong, L. M. Mansfield, B. J. Stanbery, K. Zhu, Y. Yan, J. J. Berry, A. J. Ptak, F. Dimroth, B. M. Kayes, A. C. Tamboli, R. Peibst, K. Catchpole, M. O. Reese, C. S. Klinga, P. Denholm, M. Morjaria, M. G. Deceglie, J. M. Freeman, M. A. Mikofski, D. C. Jordan, G. TamizhMani and D. B. Sulas-Kern, *J. Phys. D. Appl. Phys.*, 2020, **53**, 493001.

5 P. Roy, N. Kumar Sinha, S. Tiwari and A. Khare, *Sol. Energy*, 2020, **198**, 665–688.

6 K. S. Ahmad, S. N. Naqvi and S. B. Jaffri, *Rev. Inorg. Chem.*, 2021, **41**, 21–39.

7 H. D. Pham, T. C. Yang, S. M. Jain, G. J. Wilson and P. Sonar, *Adv. Energy Mater.*, 2020, **10**, 1903326.

8 Y. Fan, H. Meng, L. Wang and S. Pang, *Sol. RRL*, 2019, **3**, 1900215.

9 M. A. Green, A. Ho-Baillie and H. J. Snaith, *Nat. Photonics*, 2014, **8**, 506–514.

10 Q. Xu, D. Yang, J. Lv, Y.-Y. Sun and L. Zhang, *Small Methods*, 2018, **2**, 1700316.

11 V. Adinolfi, W. Peng, G. Walters, O. M. Bakr and E. H. Sargent, *Adv. Mater.*, 2018, **30**, 1–13.

12 M. A. Green, *Prog. Photovoltaics Res. Appl.*, 2012, **20**, 472–476.

13 D. W. deQuilettes, M. Laitz, R. Brenes, B. Dou, B. T. Motes, S. D. Stranks, H. J. Snaith, V. Bulović and D. S. Ginger, *Pure Appl. Chem.*, 2020, **92**, 697–706.

14 M. A. Green and A. W. Y. Ho-Baillie, *ACS Energy Lett.*, 2019, **4**, 1639–1644.

15 A. Mishra and P. Bäuerle, *Angew. Chemie - Int. Ed.*, 2012, **51**, 2020–2067.

16 H. J. Snaith, *J. Phys. Chem. Lett.*, 2013, **4**, 3623–3630.

17 PCE of solar cells, https://www.aalto.fi/en/news/patrick-rinke-awarded-academy-of-finland-funding.

18 T. Du, W. Xu, S. Xu, S. R. Ratnasingham, C. T. Lin, J. Kim, J. Briscoe, M. A. McLachlan and J. R. Durrant, *J. Mater. Chem. C*, 2020, **8**, 12648–12655.

19 H. J. Snaith, *Nat. Mater.*, 2018, **17**, 372–376.

20 U. Krishnan, M. Kaur, M. Kumar and A. Kumar, *J. Photonics Energy*, 2019, **9**, 1.

21 J. S. Manser, M. I. Saidaminov, J. A. Christians, O. M. Bakr and P. V. Kamat, *Acc. Chem. Res.*, 2016, **49**, 330–338.

22 N. Aristidou, C. Eames, I. Sanchez-Molina, X. Bu, J. Kosco, M. Saiful Islam and S. A. Haque, *Nat. Commun.*, 2017, **8**, 1–10.

23 B. Li, Y. Li, C. Zheng, D. Gao and W. Huang, *RSC Adv.*, 2016, **6**, 38079–38091.

24 N. Aristidou, I. Sanchez-Molina, T. Chotchuangchutchaval, M. Brown, L. Martinez, T. Rath and S. A. Haque, *Angew. Chemie Int. Ed.*, 2015, **54**, 8208–8212.

25 E. J. Juarez-Perez, L. K. Ono, M. Maeda, Y. Jiang, Z. Hawash and Y. Qi, *J. Mater. Chem. A*, 2018, **6**, 9604–9612.

26 M. Kim, S. Ham, D. Cheng, T. A. Wynn, H. S. Jung and Y. S. Meng, *Adv. Energy Mater.*, 2021, **11**, 2001753.

27 L. Zhang and J. M. Cole, *ACS Appl. Mater. Interfaces*, 2015, **7**, 3427–3455.

28 K. Liao, J. A. Yang, C. Li, T. Li and F. Hao, *ACS Appl. Mater. Interfaces*, 2019, **11**, 39882–39889.

29 B. Dänekamp, N. Droseros, F. Palazon, M. Sessolo, N. Banerji and H. J. Bolink, *ACS Appl. Mater. Interfaces*, 2018, **10**, 36187–36193.

30 Y. Xie, F. Shao, Y. Wang, T. Xu, D. Wang and F. Huang, *ACS Appl. Mater. Interfaces*, 2015, **7**, 12937–12942.

31 Y. Yang, J. Song, Y. L. Zhao, L. Zhu, X. Q. Gu, Y. Q. Gu, M. Che, Y. H. Qiang and J. Song, *J. Alloys Compd.*, 2016, **684**, 84–90.

32 C. Xu, Z. Zhang, Y. Hu, Y. Sheng, P. Jiang, H. Han and J. Zhang, *J. Energy Chem.*, 2018, **27**, 764–768.

33 Y. Wang, S. Liu, Q. Zeng, R. Wang, W. Qin, H. Cao, L. Yang, L. Li, S. Yin and F. Zhang, *Sol. Energy Mater. Sol. Cells*, 2018, **188**, 140–148.

34 M. A. R. Laskar, W. Luo, N. Ghimire, A. H. Chowdhury, B. Bahrami, A. Gurung,

K. M. Reza, R. Pathak, R. S. Bobba, B. S. Lamsal, K. Chen, M. T. Rahman, S. I. Rahman, K. Emshadi, T. Xu, M. Liang, W. H. Zhang and Q. Qiao, *Adv. Funct. Mater.*, 2020, **30**, 1–11.

35 C. Du, S. Wang, X. Miao, W. Sun, Y. Zhu, C. Wang and R. Ma, *Beilstein J. Nanotechnol.*, 2019, **10**, 2374–2382.

36 D. Wang, Z. Liu, Z. Zhou, H. Zhu, Y. Zhou, C. Huang, Z. Wang, H. Xu, Y. Jin, B. Fan, S. Pang and G. Cui, *Chem. Mater.*, 2014, **26**, 7145–7150.

37 H. Yu, F. Wang, F. Xie, W. Li, J. Chen and N. Zhao, *Adv. Funct. Mater.*, 2014, **24**, 7102–7108.

38 Y. Jiang, R. Dong, X. Cai, J. Feng, Z. Liu and S. Liu, *Gaodeng Xuexiao Huaxue Xuebao/Chemical J. Chinese Univ.*, 2019, **40**, 1697–1705.

39 M. Mateen, Z. Arain, X. Liu, A. Iqbal, Y. Ren, X. Zhang, C. Liu, Q. Chen, S. Ma, Y. Ding, M. Cai and S. Dai, *Sci. China Mater.*, 2020, **63**, 2477–2486.

40 J. Yao, H. Wang, P. Wang, R. S. Gurney, A. Intaniwet, P. Ruankham, S. Choopun, D. Liu and T. Wang, *Mater. Chem. Front.*, 2019, **3**, 1357–1364.

41 S. Bae, J. W. Jo, P. Lee and M. J. Ko, *ACS Appl. Mater. Interfaces*, 2019, **11**, 17452–17458.

42 Y. Wang, N. Song, L. Feng and X. Deng, *ACS Appl. Mater. Interfaces*, 2016, **8**, 24703–24711.

43 C.-C. Chen, Z. Hong, G. Li, Q. Chen, H. Zhou and Y. Yang, *J. Photonics Energy*, 2015, **5**, 057405.

44 M. Mangrulkar, S. Y. Luchkin, A. G. Boldyreva, P. A. Troshin and K. J.

Stevenson, *Mendeleev Commun.*, 2021, **31**, 319–322.

45 L. A. Frolova, A. I. Davlethanov, N. N. Dremova, I. Zhidkov, A. F. Akbulatov, E. Z. Kurmaev, S. M. Aldoshin, K. J. Stevenson and P. A. Troshin, *J. Phys. Chem. Lett.*, 2020, **11**, 6772–6778.

46 J. Zhen, W. Zhou, M. Chen, B. Li, L. Jia, M. Wang and S. Yang, *J. Mater. Chem. A*, 2019, **7**, 2754–2763.

47 S. Fu, X. Li, L. Wan, Y. Wu, W. Zhang, Y. Wang, Q. Bao and J. Fang, *Adv. Energy Mater.*, 2019, **9**, 1–10.

48 F. Cheng, X. Jing, R. Chen, J. Cao, J. Yan, Y. Wu, X. Huang, B. Wu and N. Zheng, *Inorg. Chem. Front.*, 2019, **6**, 2458–2463.

49 S. Lee, M. C. Tang, R. Munir, D. Barrit, Y. J. Kim, R. Kang, J. M. Yun, D. M. Smilgies, A. Amassian and D. Y. Kim, *J. Mater. Chem. A*, 2020, **8**, 7695–7703.

50 R. Xia, Z. Fei, N. Drigo, F. D. Bobbink, Z. Huang, R. Jasiūnas, M. Franckevičius, V. Gulbinas, M. Mensi, X. Fang, C. Roldán-Carmona, M. K. Nazeeruddin and P. J. Dyson, *Adv. Funct. Mater.*, 2019, **29**, 1902021.

51 C. Luo, G. Li, L. Chen, J. Dong, M. Yu, C. Xu, Y. Yao, M. Wang, Q. Song and S. Zhang, *Sustain. Energy Fuels*, 2020, **4**, 3971–3978.

52 X. Zheng, T. Jiang, L. Bai, X. Chen, Z. Chen, X. Xu, D. Song, X. Xu, B. Li and Y. Yang, *RSC Adv.*, 2020, **10**, 18400–18406.

53 S. Chen, Q. Pan, J. Li, C. Zhao, X. Guo, Y. Zhao and T. Jiu, *Sci. China Mater.*, 2020, **63**, 2465–2476.

54 J. F. Liao, W. Q. Wu, J. X. Zhong, Y. Jiang, L. Wang and D. Bin Kuang, *J. Mater.*

Chem. A, 2019, **7**, 9025–9033.

55 L. L. Jiang, Z. K. Wang, M. Li, C. C. Zhang, Q. Q. Ye, K. H. Hu, D. Z. Lu, P. F. Fang and L. S. Liao, *Adv. Funct. Mater.*, 2018, **28**, 1–8.

56 L. Hu, T. Liu, L. Sun, S. Xiong, F. Qin, X. Jiang, Y. Jiang and Y. Zhou, *Chem. Commun.*, 2018, **54**, 4704–4707.

57 L. Li, Y. Chen, Z. Liu, Q. Chen, X. Wang and H. Zhou, *Adv. Mater.*, 2016, **28**, 9862–9868.

58 M. Mangrulkar and K. J. Stevenson, *Cryst. 2021, Vol. 11, Page 814*, 2021, **11**, 814.

59 T. Zhang, Z. Cao, Y. Shang, C. Cui, P. Fu, X. Jiang, F. Wang, K. Xu, D. Yin, D. Qu and Z. Ning, *J. Photochem. Photobiol. A Chem.*, 2018, **355**, 42–47.

60 H. Xiong, B. X. Zhang, W. Jia, Q. H. Zhang and H. Q. Xie, *Wuji Cailiao Xuebao/Journal Inorg. Mater.*, 2019, **34**, 96–102.

61 M. Sun, F. Zhang, H. Liu, X. Li, Y. Xiao and S. Wang, *J. Mater. Chem. A*, 2017, **5**, 13448–13456.

62 L. Zhi, Y. Li, X. Cao, Y. Li, X. Cui, L. Ci and J. Wei, *Nanoscale Res. Lett.*, 2017, **12**, 632.

63 G. Zheng, L. Li, L. Wang, X. Gao and H. Zhou, *J. Semicond.*, 2017, **38**, 014001.

64 L. Gao, L. Wang, X. Ding, E. Zhao, S. Yang, Y. Zhao, Y. Li, S. Wang and T. Ma, *J. Mater. Chem. A*, 2018, **6**, 4365–4373.

65 Y. Li, L. Li, A. S. Yerramilli, Y. Chen, D. Fang, Y. Shen and T. L. Alford, *Org.*

Electron., 2019, **73**, 130–136.

66 L. Han, S. Cong, H. Yang, Y. Lou, H. Wang, J. Huang, J. Zhu, Y. Wu, Q. Chen, B. Zhang, L. Zhang and G. Zou, *Sol. RRL*, 2018, **2**, 1–9.

67 J. W. Lee, S. H. Bae, Y. T. Hsieh, N. De Marco, M. Wang, P. Sun and Y. Yang, *Chem*, 2017, **3**, 290–302.

68 S. Liu, S. Li, J. Wu, Q. Wang, Y. Ming, D. Zhang, Y. Sheng, Y. Hu, Y. Rong, A. Mei and H. Han, *J. Phys. Chem. Lett.*, 2019, **10**, 6865–6872.

69 X. Shi, Y. Wu, J. Chen, M. Cai, Y. Yang, X. Liu, Y. Tao, M. Guli, Y. Ding and S. Dai, *J. Mater. Chem. A*, 2020, **8**, 7205–7213.

70 C. Qin, T. Matsushima, T. Fujihara and C. Adachi, *Adv. Mater.*, 2017, **29**, 1–8.

71 W. Yu, S. Yu, J. Zhang, W. Liang, X. Wang, X. Guo and C. Li, *Nano Energy*, 2018, **45**, 229–235.

72 D.-W. Kuo, G.-Z. Liu and R.-H. Lee, *Dye. Pigment.*, 2019, **170**, 107562.

73 H. Li, K. Zhu, K. Zhang, P. Huang, D. Li, L. Yuan, T. Cao, Z. Sun, Z. Li, Q. Chen, B. Song, H. Zhu and Y. Zhou, *Org. Electron.*, 2019, **66**, 47–52.

74 P. Wang, H. Wang, F. Ye, H. Zhang, M. Chen, J. Cai, D. Li, D. Liu and T. Wang, *ACS Appl. Mater. Interfaces*, 2019, **11**, 37833–37841.

75 S. Xiong, J. Song, J. Yang, J. Xu, M. Zhang, R. Ma, D. Li, X. Liu, F. Liu, C. Duan, M. Fahlman and Q. Bao, *Sol. RRL*, 2020, **4**, 1–9.

76 Y. Lan, Y. Wang and Y. Song, *Flex. Print. Electron.*, 2020, **5**, 014001.

77 C. Song, X. Li, Y. Wang, S. Fu, L. Wan, S. Liu, W. Zhang, W. Song and J. Fang,

J. Mater. Chem. A, 2019, **7**, 19881–19888.

78 X. B. Cao, C. L. Li, L. L. Zhi, Y. H. Li, X. Cui, Y. W. Yao, L. J. Ci and J. Q. Wei, *J. Mater. Chem. A*, 2017, **5**, 8416–8422.

79 X. Cao, L. Zhi, Y. Li, X. Cui, L. Ci, K. Ding and J. Wei, *RSC Adv.*, 2017, **7**, 49144–49150.

80 R. Gregorio and D. S. Borges, *Polymer (Guildf).*, 2008, **49**, 4009–4016.

81 F. Hao, C. C. Stoumpos, P. Guo, N. Zhou, T. J. Marks, R. P. H. Chang and M. G. Kanatzidis, *J. Am. Chem. Soc.*, 2015, **137**, 11445–11452.

82 X. Cao, L. Zhi, Y. Li, F. Fang, X. Cui, Y. Yao, L. Ci, K. Ding and J. Wei, *J. Mater. Chem. C*, 2017, **5**, 7458–7464.

83 Y. Ren, X. Ding, J. Zhu, T. Hayat, A. Alsaedi, Z. Li, X. Xu, Y. Ding, S. Yang, M. Kong and S. Dai, *J. Alloys Compd.*, 2018, **758**, 171–176.

84 B. J. Foley, J. Girard, B. A. Sorenson, A. Z. Chen, J. Scott Niezgoda, M. R. Alpert, A. F. Harper, D. M. Smilgies, P. Clancy, W. A. Saidi and J. J. Choi, *J. Mater. Chem. A*, 2017, **5**, 113–123.

85 M. Gutwald, N. Rolston, A. D. Printz, O. Zhao, H. Elmaraghi, Y. Ding, J. Zhang and R. H. Dauskardt, *Sol. Energy Mater. Sol. Cells*, 2020, **209**, 110433.

86 C. T. Lin, F. De Rossi, J. Kim, J. Baker, J. Ngiam, B. Xu, S. Pont, N. Aristidou, S. A. Haque, T. Watson, M. A. McLachlan and J. R. Durrant, *J. Mater. Chem. A*, 2019, **7**, 3006–3011.

87 N. Santhosh, S. R. Sitaaraman, P. Pounraj, R. Govindaraj, M. S. Pandian and P. Ramasamy, *Mater. Lett.*, 2019, **236**, 706–709.

88 N. Li, F. Xu, Z. Qiu, J. Liu, X. Wan, X. Zhu, H. Yu, C. Li, Y. Liu and B. Cao, *J. Power Sources*, 2019, **426**, 188–196.

89 H. Chen, T. Liu, P. Zhou, S. Li, J. Ren, H. He, J. Wang, N. Wang and S. Guo, *Adv. Mater.*, 2020, **32**, 1905661.

90 C. Zhang, Q. Luo, X. Deng, J. Zheng, W. Ou-Yang, X. Chen and S. Huang, *Electrochim. Acta*, 2017, **258**, 1262–1272.

91 L. Su, Y. Xiao, G. Han, L. Lu, H. Li and M. Zhu, *J. Power Sources*, 2019, **426**, 11–15.

92 L. Su, Y. Xiao, L. Lu, G. Han and M. Zhu, *Org. Electron.*, 2020, **77**, 105519.

93 A. Pockett, D. Raptis, S. M. P. Meroni, J. Baker, T. Watson and M. Carnie, *J. Phys. Chem. C*, 2019, **123**, 11414–11421.

94 X. Yao, L. Zheng, X. Zhang, W. Xu, W. Hu and X. Gong, *ACS Appl. Mater. Interfaces*, 2019, **11**, 40163–40171.

95 F. Han, J. Luo, H. A. Malik, B. Zhao, Z. Wan and C. Jia, *J. Power Sources*, 2017, **359**, 577–584.

96 C. Gao, H. Dong, X. Bao, Y. Zhang, A. Saparbaev, L. Yu, S. Wen, R. Yang and L. Dong, *J. Mater. Chem. C*, 2018, **6**, 8234–8241.

97 M. Wang, B. Li, P. Siffalovic, L. C. Chen, G. Cao and J. Tian, *J. Mater. Chem. A*, 2018, **6**, 15386–15394.

98 Y. Wu, F. Xie, H. Chen, X. Yang, H. Su, M. Cai, Z. Zhou, T. Noda and L. Han, *Adv. Mater.*, 2017, **29**, 1–8.

99 Q. Wu, P. Zhou, W. Zhou, X. Wei, T. Chen and S. Yang, *ACS Appl. Mater. Interfaces*, 2016, **8**, 15333–15340.

100 Z. Zhang, W. Fan, X. Wei, L. Zhang, Z. Yang, Z. Wei, T. Shen, H. Si and J. Qi, *J. Alloys Compd.*, 2019, **802**, 694–703.

101 G. Tang, P. You, Q. Tai, R. Wu and F. Yan, *Sol. RRL*, 2018, **2**, 1–9.

102 Y. Wang, Y. Wu, S. Fu, C. Song, L. Wan, W. Zhang, X. Li, W. Yang, W. Song and J. Fang, *J. Mater. Chem. C*, 2019, **7**, 11411–11418.

103 Y. Guan, A. Mei, Y. Rong, M. Duan, X. Hou, Y. Hu and H. Han, *Org. Electron.*, 2018, **62**, 653–659.

104 L. Hu, S. Li, L. Zhang, Y. Liu, C. Zhang, Y. Wu, Q. Sun, Y. Cui, F. Zhu, Y. Hao and Y. Wu, *Carbon N. Y.*, 2020, **167**, 160–168.

105 N. Chen, X. Yi, J. Zhuang, Y. Wei, Y. Zhang, F. Wang, S. Cao, C. Li and J. Wang, *Nano-Micro Lett.*, 2020, **12**, 1–13.

106 H.-L. Hsu, B.-H. Jiang, C.-L. Chung, Y.-Y. Yu, R.-J. Jeng and C.-P. Chen, *Nanotechnology*, 2020, **31**, 274002.

107 J. Yang, S. Xiong, T. Qu, Y. Zhang, X. He, X. Guo, Q. Zhao, S. Braun, J. Chen, J. Xu, Y. Li, X. Liu, C. Duan, J. Tang, M. Fahlman and Q. Bao, *ACS Appl. Mater. Interfaces*, 2019, **11**, 13491–13498.

108 M. Guan, Q. Zhang, F. Wang, H. Liu, J. Zhao, C. Jia and Y. Chen, *Electrochim. Acta*, 2019, **293**, 174–183.

109 B. A. de Carvalho, S. Kavadiya, S. Huang, D. M. Niedzwiedzki and P. Biswas, *IEEE J. Photovoltaics*, 2017, **7**, 532–538.

110 M. J. A. Isa, J. Sulistianto, Rembianov, L. Kevin and N. R. Poespawati, in *2019 11th International Conference on Information Technology and Electrical Engineering (ICITEE)*, IEEE, 2019, vol. 7, pp. 1–5.

111 B. Chaudhary, A. Kulkarni, A. K. Jena, M. Ikegami and T. Miyasaka, *Energy Technol.*, 2020, **8**, 1900990.

112 H. Wang, W. Zeng and R. Xia, *Thin Solid Films*, 2018, **663**, 9–13.

113 S. Kumar, Y. Choi, S. H. Kang, N. K. Oh, J. Lee, J. Seo, M. Jeong, H. W. Kwon, S. Il Seok, C. Yang and H. Park, *ACS Appl. Mater. Interfaces*, 2019, **11**, 38828–38837.

114 M. Feng, S. You, N. Cheng and J. Du, *Electrochim. Acta*, 2019, **293**, 356–363.

115 S. You, S. Bi, J. Huang, Q. Jia, Y. Yuan, Y. Xia, Z. Xiao, Z. Sun, J. Liu, S. Sun and Z. Zhao, *Chem. - A Eur. J.*, 2017, **23**, 18140–18145.

116 E. Ugur, A. D. Sheikh, R. Munir, J. I. Khan, D. Barrit, A. Amassian and F. Laquai, *ACS Energy Lett.*, 2017, **2**, 1960–1968.

117 W. Wu, H. Li, S. Liu, B. Zheng, Y. Xue, X. Liu and C. Gao, *RSC Adv.*, 2016, **6**, 89609–89613.

118 N. Balis, A. A. Zaky, C. Athanasekou, A. M. Silva, E. Sakellis, M. Vasilopoulou, T. Stergiopoulos, A. G. Kontos and P. Falaras, *J. Photochem. Photobiol. A Chem.*, 2020, **386**, 112141.

119 Y.-Y. Yu, C. Tseng, W.-C. Chien, H.-L. Hsu and C.-P. Chen, *J. Phys. Chem. C*, 2019, **123**, 23826–23833.

120 J. Feng, X. Zhu, Z. Yang, X. Zhang, J. Niu, Z. Wang, S. Zuo, S. Priya, S. (Frank)

Liu and D. Yang, *Adv. Mater.*, 2018, **30**, 1801418.

121 C. M. Hsieh, Y. S. Liao, Y. R. Lin, C. P. Chen, C. M. Tsai, E. Wei-Guang Diau and S. C. Chuang, *RSC Adv.*, 2018, **8**, 19610–19615.

122 C. Cui, D. Xie, P. Lin, H. Hu, S. Che, K. Xiao, P. Wang, L. Xu, D. Yang and X. Yu, *Sol. Energy Mater. Sol. Cells*, 2020, **208**, 110435.

123 Y. Gao, Y. Wu, Y. Liu, C. Chen, X. Bai, L. Yang, Z. Shi, W. W. Yu, Q. Dai and Y. Zhang, *ACS Appl. Mater. Interfaces*, 2020, **12**, 3631–3641.

124 W. Ke, C. Xiao, C. Wang, B. Saparov, H. S. Duan, D. Zhao, Z. Xiao, P. Schulz, S. P. Harvey, W. Liao, W. Meng, Y. Yu, A. J. Cimaroli, C. S. Jiang, K. Zhu, M. Al-Jassim, G. Fang, D. B. Mitzi and Y. Yan, *Adv. Mater.*, 2016, **28**, 5214–5221.

125 M. K. Kim, T. Jeon, H. Il Park, J. M. Lee, S. A. Nam and S. O. Kim, *CrystEngComm*, 2016, **18**, 6090–6095.

126 R. Zhang, M. Li, Y. Huan, J. Xi, S. Zhang, X. Cheng, H. Wu, W. Peng, Z. Bai and X. Yan, *Inorg. Chem. Front.*, 2019, **6**, 434–442.

127 H. Zhang, M. Hou, Y. Xia, Q. Wei, Z. Wang, Y. Cheng, Y. Chen and W. Huang, *J. Mater. Chem. A*, 2018, **6**, 9264–9270.

128 Q. Han, Y. Bai, J. Liu, K. Du, T. Li, D. Ji, Y. Zhou, C. Cao, D. Shin, J. Ding, A. D. Franklin, J. T. Glass, J. Hu, M. J. Therien, J. Liu and D. B. Mitzi, *Energy Environ. Sci.*, 2017, **10**, 2365–2371.

129 N. Cheng, W. Li, M. Zhang, H. Wu, S. Sun, Z. Zhao, Z. Xiao, Z. Sun, W. Zi and L. Fang, *Curr. Appl. Phys.*, 2019, **19**, 25–30.

130 J. Zou, W. Liu, W. Deng, G. Lei, S. Zeng, J. Xiong, H. Gu, Z. Hu, X. Wang and J.

Li, *Electrochim. Acta*, 2018, **291**, 297–303.

131 J. P. Correa-Baena, M. Anaya, G. Lozano, W. Tress, K. Domanski, M. Saliba, T. Matsui, T. J. Jacobsson, M. E. Calvo, A. Abate, M. Grätzel, H. Míguez and A. Hagfeldt, *Adv. Mater.*, 2016, **28**, 5031–5037.

132 S. Zhang, Y. Lu, B. Lin, Y. Zhu, K. Zhang, N. Y. Yuan, J. N. Ding and B. Fang, *Sol. Energy Mater. Sol. Cells*, 2017, **170**, 178–186.

133 C. Sun, Y. Guo, B. Fang, J. Yang, B. Qin, H. Duan, Y. Chen, H. Li and H. Liu, *J. Phys. Chem. C*, 2016, **120**, 12980–12988.

134 V. O. Eze, Y. Seike and T. Mori, *ACS Appl. Mater. Interfaces*, 2020, **12**, 46837–46845.

135 K. Ankireddy, A. H. Ghahremani, B. Martin, G. Gupta and T. Druffel, *J. Mater. Chem. A*, 2018, **6**, 9378–9383.

136 Y. Ma, H. Zhang, Y. Zhang, R. Hu, M. Jiang, R. Zhang, H. Lv, J. Tian, L. Chu, J. Zhang, Q. Xue, H. L. Yip, R. Xia, X. Li and W. Huang, *ACS Appl. Mater. Interfaces*, 2019, **11**, 3044–3052.

137 Ç. Kırbıyık, A. Toprak, C. Başlak, M. Kuş and M. Ersöz, *J. Alloys Compd.*, 2020, **832**, 154897.

138 Q. Guo, F. Yuan, B. Zhang, S. Zhou, J. Zhang, Y. Bai, L. Fan, T. Hayat, A. Alsaedi and Z. Tan, *Nanoscale*, 2019, **11**, 115–124.

139 H. L. Hsu, H. T. Hsiao, T. Y. Juang, B. H. Jiang, S. C. Chen, R. J. Jeng and C. P. Chen, *Adv. Energy Mater.*, 2018, **8**, 1–9.

140 Z. Li, F. Wang, C. Liu, F. Gao, L. Shen and W. Guo, *J. Mater. Chem. A*, 2019, **7**,

22359–22365.

141 Y. Wang, J. Zhang, S. Chen, H. Zhang, L. Li and Z. Fu, *J. Mater. Sci.*, 2018, **53**, 9180–9190.

142 X. Fang, J. Ding, N. Yuan, P. Sun, M. Lv, G. Ding and C. Zhu, *Phys. Chem. Chem. Phys.*, 2017, **19**, 6057–6063.

143 R. Brakkee and R. M. Williams, *Appl. Sci.*, 2020, **10**, 3061.

144 C. M. M. Soe, C. C. Stoumpos, B. Harutyunyan, E. F. Manley, L. X. Chen, M. J. Bedzyk, T. J. Marks and M. G. Kanatzidis, *ChemSusChem*, 2016, **9**, 2656–2665.

145 T. Zhang, N. Guo, G. Li, X. Qian and Y. Zhao, *Nano Energy*, 2016, **26**, 50–56.

146 Y. Wen, Y.-G. Tang and G.-Q. Yan, *AIP Adv.*, 2018, **8**, 095226.

147 M. Abdi-Jalebi, M. I. Dar, A. Sadhanala, S. P. Senanayak, M. Franckevičius, N. Arora, Y. Hu, M. K. Nazeeruddin, S. M. Zakeeruddin, M. Grätzel and R. H. Friend, *Adv. Energy Mater.*, 2016, **6**, 1502472.

148 K. M. Boopathi, R. Mohan, T.-Y. Huang, W. Budiawan, M.-Y. Lin, C.-H. Lee, K.-C. Ho and C.-W. Chu, *J. Mater. Chem. A*, 2016, **4**, 1591–1597.

149 I. J. Park, S. Seo, M. A. Park, S. Lee, D. H. Kim, K. Zhu, H. Shin and J. Y. Kim, *ACS Appl. Mater. Interfaces*, 2017, **9**, 41898–41905.

150 S.-H. Chan, M.-C. Wu, K.-M. Lee, W.-C. Chen, T.-H. Lin and W.-F. Su, *J. Mater. Chem. A*, 2017, **5**, 18044–18052.

151 C. Chen, Y. Xu, S. Wu, S. Zhang, Z. Yang, W. Zhang, H. Zhu, Z. Xiong, W. Chen and W. Chen, *J. Mater. Chem. A*, 2018, **6**, 7903–7912.

152 B. Duan, Y. Ren, Y. Xu, W. Chen, Q. Ye, Y. Huang, J. Zhu and S. Dai, *Inorg. Chem. Front.*, 2017, **4**, 473–480.

153 S. Mabrouk, B. Bahrami, A. Gurung, K. M. Reza, N. Adhikari, A. Dubey, R. Pathak, S. Yang and Q. Qiao, *Sustain. Energy Fuels*, 2017, **1**, 2162–2171.

154 H. Chen, Q. Luo, T. Liu, J. Ren, S. Li, M. Tai, H. Lin, H. He, J. Wang and N. Wang, *Small*, 2019, **15**, 1904372.

155 X. Gong, L. Guan, H. Pan, Q. Sun, X. Zhao, H. Li, H. Pan, Y. Shen, Y. Shao, L. Sun, Z. Cui, L. Ding and M. Wang, *Adv. Funct. Mater.*, 2018, **28**, 1804286.

156 M. Emrul Kayesh, K. Matsuishi, T. H. Chowdhury, R. Kaneko, T. Noda and A. Islam, *Electron. Mater. Lett.*, 2018, **14**, 712–717.

157 Z. S. Almutawah, S. C. Watthage, Z. Song, R. H. Ahangharnejhad, K. K. Subedi, N. Shrestha, A. B. Phillips, Y. Yan, R. J. Ellingson and M. J. Heben, *MRS Adv.*, 2018, **3**, 3237–3242.

158 S. C. Watthage, Z. Song, N. Shrestha, A. B. Phillips, G. K. Liyanage, P. J. Roland, R. J. Ellingson and M. J. Heben, *MRS Adv.*, 2017, **2**, 1183–1188.

159 W. Liu, N. Liu, S. Ji, H. Hua, Y. Ma, R. Hu, J. Zhang, L. Chu, X. Li and W. Huang, *Nano-Micro Lett.*, 2020, **12**, 119.

160 C. Roldán-Carmona, P. Gratia, I. Zimmermann, G. Grancini, P. Gao, M. Graetzel and M. K. Nazeeruddin, *Energy Environ. Sci.*, 2015, **8**, 3550–3556.

161 S. Rafizadeh, K. Wienands, P. S. C. Schulze, A. J. Bett, L. C. Andreani, M. Hermle, S. Glunz and J. C. Goldschmidt, *ACS Appl. Mater. Interfaces*, 2019, **11**, 722–729.

162 Y. Chen, A. Yerramilli, Y. Shen, Z. Zhao and T. Alford, *Sol. Energy Mater. Sol. Cells*, 2018, **174**, 478–484.

163 A. S. Yerramilli, Y. Chen, D. Sanni, J. Asare, N. D. Theodore and T. L. Alford, *Org. Electron.*, 2018, **59**, 107–112.

164 J. Barbé, M. Newman, S. Lilliu, V. Kumar, H. K. H. Lee, C. Charbonneau, C. Rodenburg, D. Lidzey and W. C. Tsoi, *J. Mater. Chem. A*, 2018, **6**, 23010–23018.

165 Z. Li, C. Zhang, Z. Shao, Y. Fan, R. Liu, L. Wang and S. Pang, *J. Mater. Chem. A*, 2018, **6**, 9397–9401.

166 T. Meier, T. P. Gujar, A. Schönleber, S. Olthof, K. Meerholz, S. Van Smaalen, F. Panzer, M. Thelakkat and A. Köhler, *J. Mater. Chem. C*, 2018, **6**, 7512–7519.

167 T. P. Gujar, T. Unger, A. Schönleber, M. Fried, F. Panzer, S. van Smaalen, A. Köhler and M. Thelakkat, *Phys. Chem. Chem. Phys.*, 2018, **20**, 605–614.

168 F. Liu, Q. Dong, M. K. Wong, A. B. Djurišić, A. Ng, Z. Ren, Q. Shen, C. Surya, W. K. Chan, J. Wang, A. M. C. Ng, C. Liao, H. Li, K. Shih, C. Wei, H. Su and J. Dai, *Adv. Energy Mater.*, 2016, **6**, 1502206.

169 M. Mangrulkar, S. Y. Luchkin, A. F. Akbulatov, I. Zhidkov, E. Z. Kurmaev, P. A. Troshin and K. J. Stevenson, *Synth. Met.*, 2021, **278**, 116823.

170 Z. Zhang, X. Yue, D. Wei, M. Li, P. Fu, B. Xie, D. Song and Y. Li, *RSC Adv.*, 2015, **5**, 104606–104611.

171 F. Jiang, Y. Rong, H. Liu, T. Liu, L. Mao, W. Meng, F. Qin, Y. Jiang, B. Luo, S. Xiong, J. Tong, Y. Liu, Z. Li, H. Han and Y. Zhou, *Adv. Funct. Mater.*, 2016, **26**, 8119–8127.

172 T. T. Ngo, S. Masi, P. F. Mendez, M. Kazes, D. Oron and I. M. Seró, *Nanoscale Adv.*, 2019, **1**, 4109–4118.

173 S. Wang, W. Dong, X. Fang, Q. Zhang, S. Zhou, Z. Deng, R. Tao, J. Shao, R. Xia, C. Song, L. Hu and J. Zhu, *Nanoscale*, 2016, **8**, 6600–6608.

174 S. R. Pathipati and M. N. Shah, *Sol. Energy*, 2018, **162**, 8–13.

175 C. Zuo and L. Ding, *Nanoscale*, 2014, **6**, 9935.

176 M. Jahandar, N. Khan, M. Jahankhan, C. E. Song, H. K. Lee, S. K. Lee, W. S. Shin, J.-C. Lee, S. H. Im and S.-J. Moon, *J. Ind. Eng. Chem.*, 2019, **80**, 265–272.

177 W. Zhang, S. Pathak, N. Sakai, T. Stergiopoulos, P. K. Nayak, N. K. Noel, A. A. Haghighirad, V. M. Burlakov, D. W. DeQuilettes, A. Sadhanala, W. Li, L. Wang, D. S. Ginger, R. H. Friend and H. J. Snaith, *Nat. Commun.*, 2015, **6**, 10030.

178 Z. Xiao, D. Wang, Q. Dong, Q. Wang, W. Wei, J. Dai, X. Zeng and J. Huang, *Energy Environ. Sci.*, 2016, **9**, 867–872.

179 W. Xu, G. Lei, C. Tao, J. Zhang, X. Liu, X. Xu, W. Lai, F. Gao and W. Huang, *Adv. Funct. Mater.*, 2018, **28**, 1802320.

180 M. Mangrulkar, A. G. Boldyreva, S. A. Lipovskikh, P. A. Troshin and K. J. Stevenson, *J. Mater. Res.*, 2021, **36**, 1846–1854.

181 X. Zhang, S. Yuan, H. Lu, H. Zhang, P. Wang, X. Cui, Y. Zhang, Q. Liu, J. Wang, Y. Zhan, Z. Sun and W. Huang, *ACS Appl. Mater. Interfaces*, 2017, **9**, 36810–36816.

182 T. Abzieher, F. Mathies, M. Hetterich, A. Welle, D. Gerthsen, U. Lemmer, U. W. Paetzold and M. Powalla, *Phys. Status Solidi Appl. Mater. Sci.*, 2017, **214**, 1–9.

183 M. V. Khenkin, E. A. Katz, A. Abate, G. Bardizza, J. J. Berry, C. Brabec, F. Brunetti, V. Bulović, Q. Burlingame, A. Di Carlo, R. Cheacharoen, Y.-B. Cheng, A. Colsmann, S. Cros, K. Domanski, M. Dusza, C. J. Fell, S. R. Forrest, Y. Galagan, D. Di Girolamo, M. Grätzel, A. Hagfeldt, E. von Hauff, H. Hoppe, J. Kettle, H. Köbler, M. S. Leite, S. (Frank) Liu, Y.-L. Loo, J. M. Luther, C.-Q. Ma, M. Madsen, M. Manceau, M. Matheron, M. McGehee, R. Meitzner, M. K. Nazeeruddin, A. F. Nogueira, Ç. Odabaşı, A. Osherov, N.-G. Park, M. O. Reese, F. De Rossi, M. Saliba, U. S. Schubert, H. J. Snaith, S. D. Stranks, W. Tress, P. A. Troshin, V. Turkovic, S. Veenstra, I. Visoly-Fisher, A. Walsh, T. Watson, H. Xie, R. Yıldırım, S. M. Zakeeruddin, K. Zhu and M. Lira-Cantu, *Nat. Energy 2020 51*, 2020, **5**, 35–49.

184 Y. Chen, A. Yerramilli, Y. Shen, Z. Zhao and T. Alford, *Sol. Energy Mater. Sol. Cells*, 2018, **174**, 478–484.

185 C. Roldán-Carmona, P. Gratia, I. Zimmermann, G. Grancini, P. Gao, M. Graetzel and M. K. Nazeeruddin, *Energy Environ. Sci.*, 2015, **8**, 3550–3556.

186 B. Shi, X. Yao, F. Hou, S. Guo, Y. Li, C. Wei, Y. Ding, Y. Li, Y. Zhao and X. Zhang, *J. Phys. Chem. C*, 2018, **122**, 21269–21276.

187 S. Rafizadeh, K. Wienands, P. S. C. Schulze, A. J. Bett, L. C. Andreani, M. Hermle, S. Glunz and J. C. Goldschmidt, *ACS Appl. Mater. Interfaces*, 2019, **11**, 722–729.

188 A. S. Yerramilli, Y. Chen, D. Sanni, J. Asare, N. D. Theodore and T. L. Alford, *Org. Electron. physics, Mater. Appl.*, 2018, **59**, 107–112.

189 T. P. Gujar, T. Unger, A. Schönleber, M. Fried, F. Panzer, S. Van Smaalen, A. Köhler and M. Thelakkat, *Phys. Chem. Chem. Phys.*, 2017, **20**, 605–614.

190 G. Tumen-Ulzii, C. Qin, D. Klotz, M. R. Leyden, P. Wang, M. Auffray, T. Fujihara, T. Matsushima, J.-W. Lee, S. Lee, Y. Yang and C. Adachi, *Adv. Mater.*, 2020, **32**, e1905035.

191 J. Chen, Y. Xiong, Y. Rong, A. Mei, Y. Sheng, P. Jiang, Y. Hu, X. Li and H. Han, *Nano Energy*, 2016, **27**, 130–137.

192 X. Cao, L. Zhi, Y. Li, F. Fang, X. Cui, Y. Yao, L. Ci, K. Ding and J. Wei, *ACS Appl. Mater. Interfaces*, 2017, **9**, 32868–32875.

193 J. C. Hamill, J. Schwartz and Y. L. Loo, *ACS Energy Lett.*, 2018, **3**, 92–97.

194 Y.-H. Seo, E.-C. Kim, S.-P. Cho, S.-S. Kim and S.-I. Na, *Appl. Mater. Today*, 2017, **9**, 598–604.

195 Y. Li, L. Zhi, G. Ge, Z. Zhao, X. Cao, F. Chen, X. Cui, F. Lin, L. Ci, J. Sun, D. Zhuang and J. Wei, *Cryst. Growth Des.*, 2019, **19**, 959–965.

196 S. Lin, W. Li, H. Sun, W. Xu, W. Guo, M. Xia and K. Yang, *MATEC Web Conf.*, 2015, **22**, 05002.

197 T. Wu, J. Wu, Y. Tu, X. He, Z. Lan, M. Huang and J. Lin, *J. Power Sources*, 2017, **365**, 1–6.

198 Y. Jo, K. S. Oh, M. Kim, K.-H. Kim, H. Lee, C.-W. Lee and D. S. Kim, *Adv. Mater. Interfaces*, 2016, **3**, 1500768.

199 G. H. Kim, J. Jeong, Y. J. Yoon, H. Jang, S. Kim, J. Seo and J. Y. Kim, *Org. Electron. physics, Mater. Appl.*, 2019, **65**, 300–304.

200 Y. Rong, Z. Tang, Y. Zhao, X. Zhong, S. Venkatesan, H. Graham, M. Patton, Y. Jing, A. M. Guloy and Y. Yao, *Nanoscale*, 2015, **7**, 10595–10599.

201 Y. Peng, Y. Cheng, C. Wang, C. Zhang, H. Xia, K. Huang, S. Tong, X. Hao and J. Yang, *Org. Electron. physics, Mater. Appl.*, 2018, **58**, 153–158.

202 L. Zhi, Y. Li, X. Cao, Y. Li, X. Cui, L. Ci and J. Wei, *J. Energy Chem.*, 2019, **30**, 78–83.

203 X. Fang, Y. Wu, Y. Lu, Y. Sun, S. Zhang, J. Zhang, W. Zhang, N. Yuan and J. Ding, *J. Mater. Chem. C*, 2017, **5**, 842–847.

204 L. Xie, H. Hwang, M. Kim and K. Kim, *Phys. Chem. Chem. Phys.*, 2017, **19**, 1143–1150.

205 M.-Z. Zhu, C. Li, B. Li, J. Zhang, Y. Sun, W. Guo, Z. Zhou, S. Pang and Y. Yan, *Mater. Horizons*, 2020, **7**, 2208–2236.

206 F. Cheng, X. Jing, R. Chen, J. Cao, J. Yan, Y. Wu, X. Huang, B. Wu and N. Zheng, *Inorg. Chem. Front.*, 2019, **6**, 2458–2463.

207 X. B. Cao, C. L. Li, L. L. Zhi, Y. H. Li, X. Cui, Y. W. Yao, L. J. Ci and J. Q. Wei, *J. Mater. Chem. A*, 2017, **5**, 8416–8422.

208 N. Li, C. Shi, M. Lu, L. Li, G. Xiao and Y. Wang, *Superlattices Microstruct.*, 2016, **100**, 179–184.

209 A. S. Yerramilli, Y. Chen and T. L. Alford, *MRS Commun.*, 2019, **9**, 189–193.

210 Z. Kwang, C.-W. Chang, T.-Y. Hsieh, T.-C. Wei and S.-Y. Lu, *Electrochim. Acta*, 2018, **266**, 118–129.

211 A. F. Akbulatov, L. A. Frolova, D. V. Anokhin, K. L. Gerasimov, N. N. Dremova and P. A. Troshin, *J. Mater. Chem. A*, 2016, **4**, 18378–18382.

212 F. Arkan and M. Izadyar, *Sol. Energy*, 2019, **194**, 51–60.

213 F. Li, C. Zhang, J. H. Huang, H. Fan, H. Wang, P. Wang, C. Zhan, C. M. Liu, X. Li, L. M. Yang, Y. Song and K. J. Jiang, *Angew. Chemie - Int. Ed.*, 2019, **58**, 6688–6692.

214 S. Tsarev, A. G. Boldyreva, S. Y. Luchkin, M. Elshobaki, M. I. Afanasov, K. J. Stevenson and P. A. Troshin, *J. Mater. Chem. A*, 2018, **6**, 21389–21395.

215 D. Wu, P. Jia, W. Bi, Y. Tang, J. Zhang, B. Song, L. Qin, Z. Lou, Y. Hu, F. Teng and Y. Hou, *Org. Electron.*, 2020, **82**, 105728.

216 M. E. Kayesh, T. H. Chowdhury, K. Matsuishi, R. Kaneko, S. Kazaoui, J. J. Lee, T. Noda and A. Islam, *ACS Energy Lett.*, 2018, **3**, 1584–1589.

217 T. Yoon, G. H. Kim, C. W. Myung, S. Kajal, J. Jeong, J. W. Kim, J. Y. Kim and K. S. Kim, *ACS Appl. Energy Mater.*, 2018, **1**, 5865–5871.

218 L.-C. Chen, K.-L. Lee, W.-T. Wu, C.-F. Hsu, Z.-L. Tseng, X. H. Sun and Y.-T. Kao, *Nanoscale Res. Lett.*, 2018, **13**, 140.

219 H. Xiong, G. DeLuca, Y. Rui, Y. Li, E. Reichmanis, Q. Zhang and H. Wang, *Sol. Energy Mater. Sol. Cells*, 2017, **166**, 167–175.

220 M. Shirayama, M. Kato, T. Miyadera, T. Sugita, T. Fujiseki, S. Hara, H. Kadowaki, D. Murata, M. Chikamatsu and H. Fujiwara, *J. Appl. Phys.*, 2016, **119**, 115501.

221 A. Mishra, Z. Ahmad, F. Touati, R. A. Shakoor and M. K. Nazeeruddin, *RSC Adv.*, 2019, **9**, 11589–11594.

222 P. Chhillar, B. P. Dhamaniya, V. Dutta and S. K. Pathak, *ACS Omega*, 2019, **4**,

11880–11887.

223 E. Smecca, Y. Numata, I. Deretzis, G. Pellegrino, S. Boninelli, T. Miyasaka, A. La Magna and A. Alberti, *Phys. Chem. Chem. Phys.*, 2016, **18**, 13413–13422.

224 P. Fassl, V. Lami, A. Bausch, Z. Wang, M. T. Klug, H. J. Snaith and Y. Vaynzof, *Energy Environ. Sci.*, 2018, **11**, 3380–3391.

225 F. T. L. Muniz, M. A. R. Miranda, C. Morilla Dos Santos and J. M. Sasaki, *Acta Crystallogr. Sect. A Found. Adv.*, 2016, **72**, 385–390.

226 A. Al Mamun, T. T. Ava, H. J. Jeong, M. S. Jeong and G. Namkoong, *Phys. Chem. Chem. Phys.*, 2017, **19**, 9143–9148.

227 Z. Y. Wu, B.-L. Jian and H.-C. Hsu, *Opt. Mater. Express*, 2019, **9**, 1882.

228 E. V. Campbell, B. Dick, A. L. Rheingold, C. Zhang, X. Liu, Z. V. Vardeny and J. S. Miller, *Chem. - A Eur. J.*, 2018, **24**, 222–229.

229 H. Huang, X. Chen and K. Huang, *Open Chem. J.*, 2019, **6**, 52–65.

230 L. Oesinghaus, J. Schlipf, N. Giesbrecht, L. Song, Y. Hu, T. Bein, P. Docampo and P. Müller-Buschbaum, *Adv. Mater. Interfaces*, 2016, **3**, 1600403.

231 T. Du, J. Kim, J. Ngiam, S. Xu, P. R. F. Barnes, J. R. Durrant and M. A. McLachlan, *Adv. Funct. Mater.*, 2018, **28**, 1801808.

232 S. Tsarev, T. S. Dubinina, S. Y. Luchkin, I. S. Zhidkov, E. Z. Kurmaev, K. J. Stevenson and P. A. Troshin, *J. Phys. Chem. C*, 2020, **124**, 1872–1877.

233 H. Zhang, J. Shi, L. Zhu, Y. Luo, D. Li, H. Wu and Q. Meng, *Nano Energy*, 2018, **43**, 383–392.

234 M. Li, X. Yan, Z. Kang, Y. Huan, Y. Li, R. Zhang and Y. Zhang, *ACS Appl. Mater. Interfaces*, 2018, **10**, 18787–18795.

235 J. H. Heo, M. H. Jang, M. H. Lee, H. J. Han, M. G. Kang, M. L. Lee and S. H. Im, *J. Mater. Chem. A*, 2016, **4**, 16324–16329.

236 L. K. Ono, S. Liu and Y. Qi, *Angew. Chemie - Int. Ed.*, 2020, **59**, 6676–6698.

237 M. C. Hsiao, P. C. Chien, L. S. Jhuang and F. C. Chen, *Phys. Chem. Chem. Phys.*, 2019, **21**, 7867–7873.

238 G. Accorsi, A. Listorti, K. Yoosaf and N. Armaroli, *Chem. Soc. Rev.*, 2009, **38**, 1690–1700.

239 E. I. Marchenko, S. A. Fateev, A. A. Petrov, E. A. Goodilin and A. B. Tarasov, *Mendeleev Commun.*, 2020, **30**, 279–281.

240 P. P. Cheng, Y. W. Zhang, J. M. Liang, W. Y. Tan, X. Chen, Y. Liu and Y. Min, *Sol. Energy*, 2019, **190**, 264–271.

241 X. Yu, H. Yan and Q. Peng, *J. Phys. Chem. A*, 2017, **121**, 6755–6765.

242 T. Oku, in *Solar Cells - New Approaches and Reviews*, InTech, 2015, pp. 77–100.

243 J. Chen, S. G. Kim, X. Ren, H. S. Jung and N. G. Park, *J. Mater. Chem. A*, 2019, **7**, 4977–4987.

244 Y. Yue, N. T. Salim, Y. Wu, X. Yang, A. Islam, W. Chen, J. Liu, E. Bi, F. Xie, M. Cai and L. Han, *Adv. Mater.*, 2016, **28**, 10738–10743.

245 S. M. Jain, Z. Qiu, L. Häggman, M. Mirmohades, M. B. Johansson, T. Edvinsson and G. Boschloo, *Energy Environ. Sci.*, 2016, **9**, 3770–3782.

246 H. Zhang, J. Cheng, D. Li, F. Lin, J. Mao, C. Liang, A. K. Y. Jen, M. Grätzel and W. C. H. Choy, *Adv. Mater.*, 2017, **29**, 1604695.

247 M. Wang, C. Shi, J. Zhang, N. Wu and C. Ying, *J. Solid State Chem.*, 2015, **231**, 20–24.

248 A. Morsali and X. M. Chen, *J. Coord. Chem.*, 2004, **57**, 1233–1241.

249 H. Miyamae, H. Toriyama, T. Abe, G. Hihara and M. Nagata, *Acta Crystallogr. Sect. C Cryst. Struct. Commun.*, 1984, **40**, 1559–1562.

250 N. Preda, L. Mihut, M. Baibarac, I. Baltog, M. Husanu, C. Bucur and T. Velula, *Rom. Reports Phys.*, 2009, **54**, 667–675.

251 I. Wharf, T. Gramstad, R. Makhija and M. Onyszchuk, *Can. J. Chem.*, 1976, **54**, 3430–3438.

252 S. N. Habisreutinger, N. K. Noel and H. J. Snaith, *ACS Energy Lett.*, 2018, **3**, 2472–2476.

Appendix 0: Literature Review Analysis

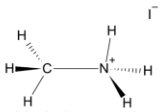

Methylammonium iodide (MAI)

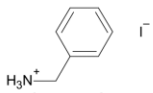

Benzylammonium iodide (BAI)

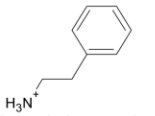

Phenethylammonium iodide (PEAI)

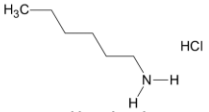

Hexylamine Hydrochloride(1-HH)

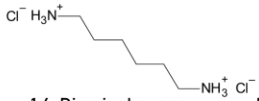

1,6-Diaminohexane Dihydrochloride (1,6-DD)

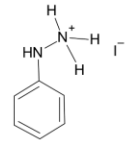

Phenylhydrazinium iodide (PHAI)

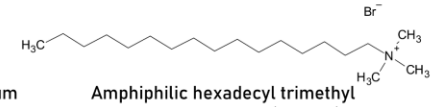

Amphiphilic hexadecyl trimethyl ammonium bromide(CTMAB)

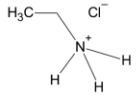

Ethylammonium chloride (EACl)

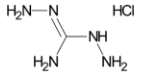

1,3-diaminoguanidine monohydrochloride (DAGCl)

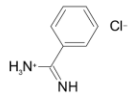

Benzamidine Hydrochloride (BMCl)

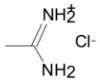

Acetamidine hydrochloride (AcHc)

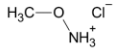

Methoxyammonium Chloride (MeOCl)

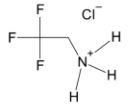

2, 2, 2-trifluoroethylamine hydrochloride (TFEACl)

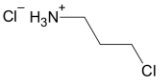

3-chloropropylamine hydrochloride(3-CPACl)

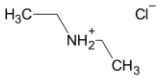

Diethylamine hydrochloride (DEACl)

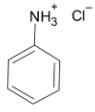

Benzenamine hydrochloride (BACl)

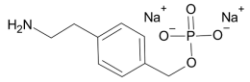

4-Ethylamine phenylphosphate disodium salt (EAPP)

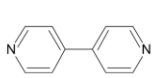

4,4'-bipyridine

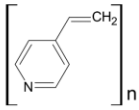

poly 4-vinylpyridine (PVP)

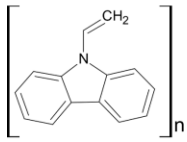

Polyvinylcarbazole (PVC)

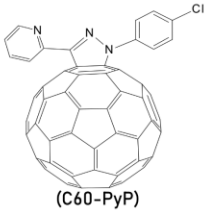

(C60-PyP)

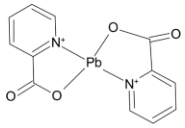

Pyridine-2-carboxylic lead salt ($PbPyA_2$)

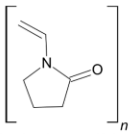

Polyvinylpyrrolidone (PVP)

NMP

NEP

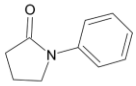

CHP

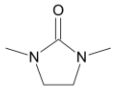

DMI

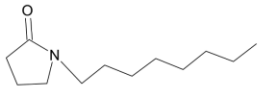

NOP

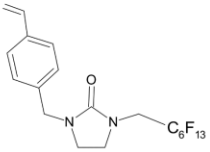

1-(4-ethenylbenzyl)-3(3,3,4,4,5,5,6,6,7,7,8,8,8-tridecafluorooctylimidazolium iodide (ETI)

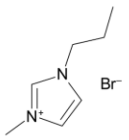

1-methyl-3-propylimidazolium bromide (MPIB)

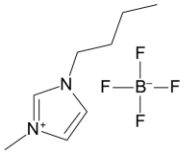

1-butyl-3-tetrafluoroborate (BMIMBF4)

Figure A0. 1 Chemical structures of amine additives for $MAPbI_3$ PSC.[58]

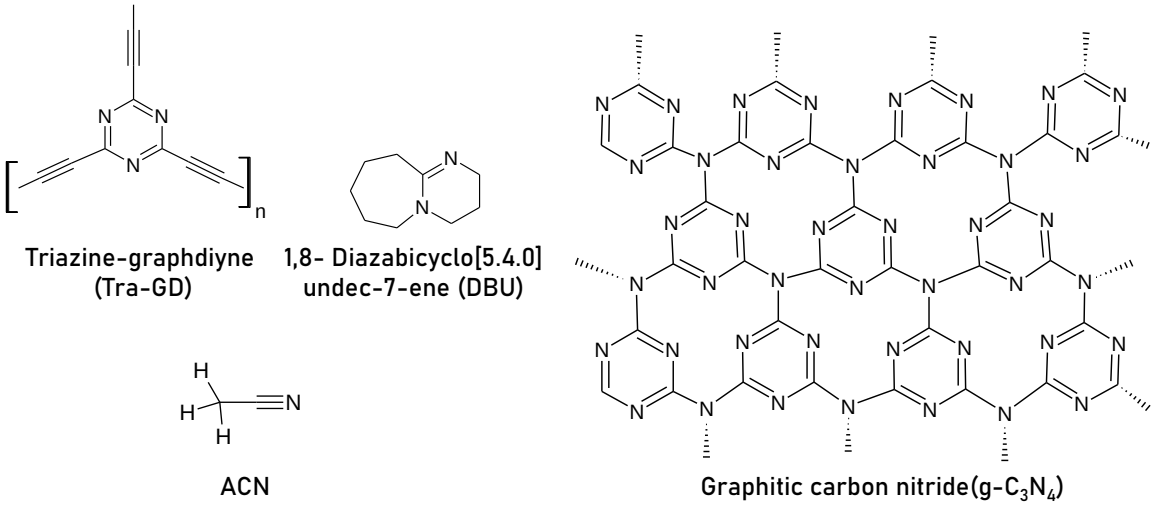

Figure A0. 2 Chemical structures of nitrile additives in $MAPbI_3$ PSC.[58]

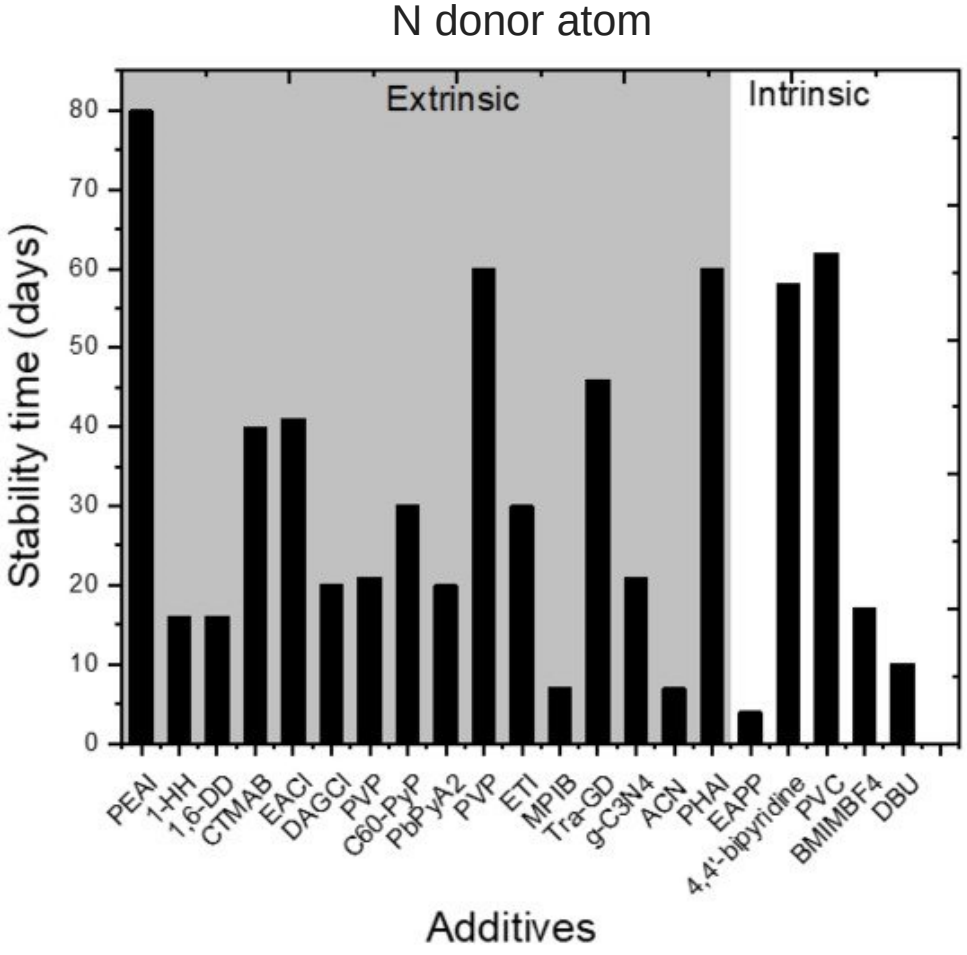

Figure A0. 3 Influence of additives with N donor atoms (amines and nitriles) on the photostability of $MAPbI_3$ photoactive layer. Here extrinsic represents ambient test conditions while intrinsic represent inert test conditions.[58]

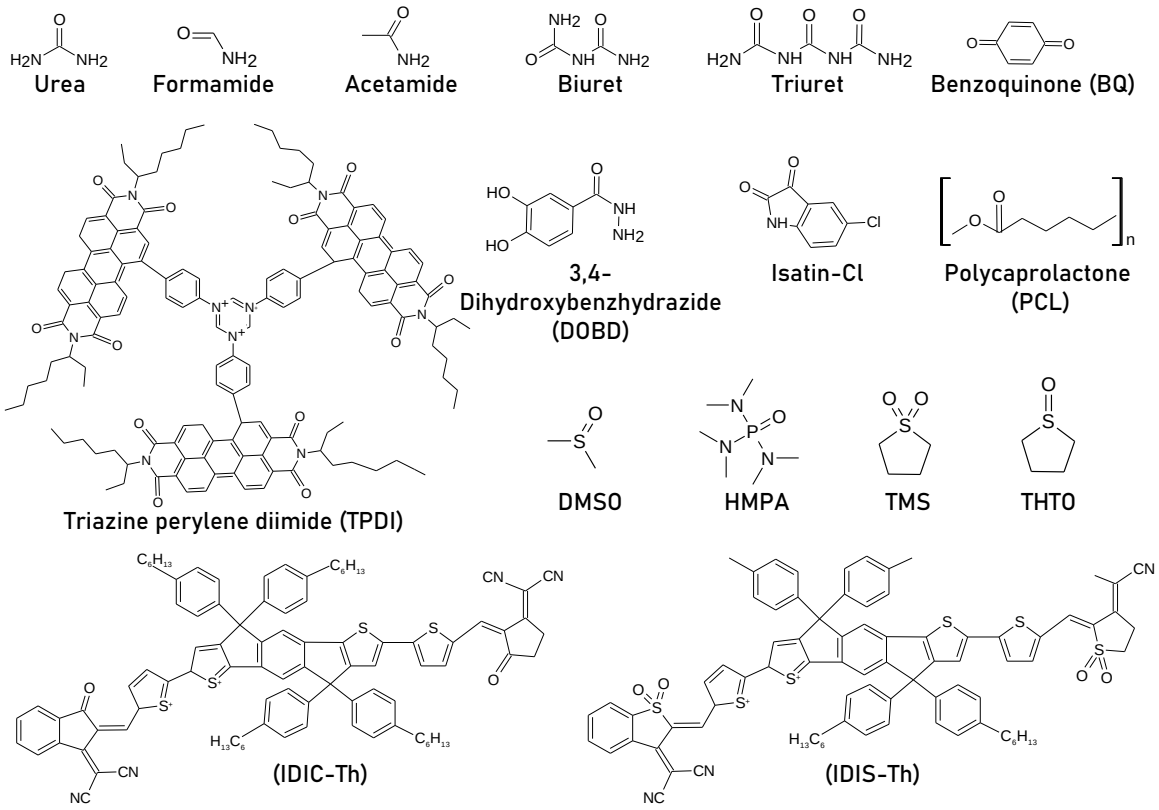

Figure A0. 4 Chemical structures of amide/carbonyl/sulphonyl based additives for $MAPbI_3$ PSC.[58]

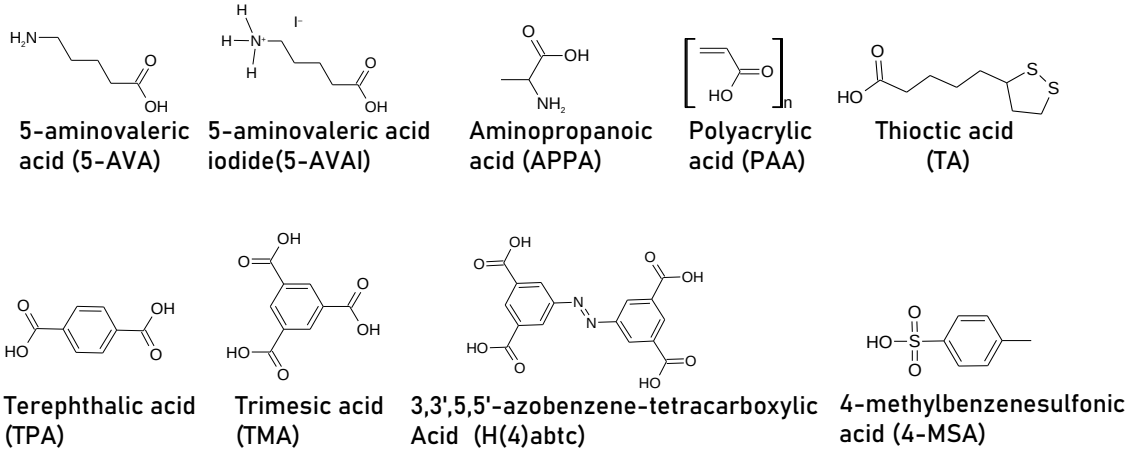

Figure A0. 5 Chemical structures of acid-containing additives for $MAPbI_3$ PSC.[58]

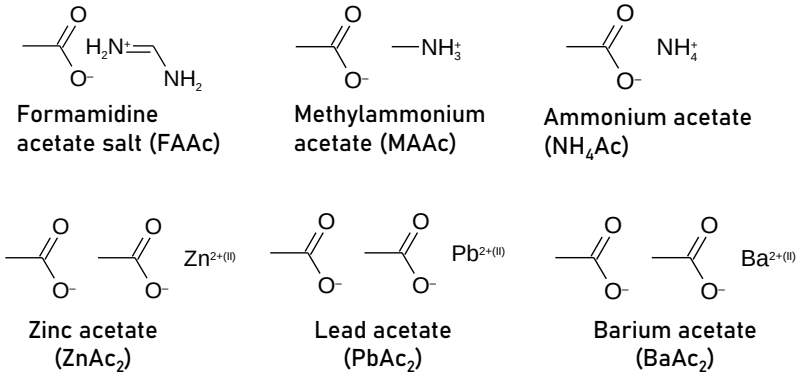

Figure A0. 6 Chemical structures of acetate-containing additives for $MAPbI_3$ PSC.[58]

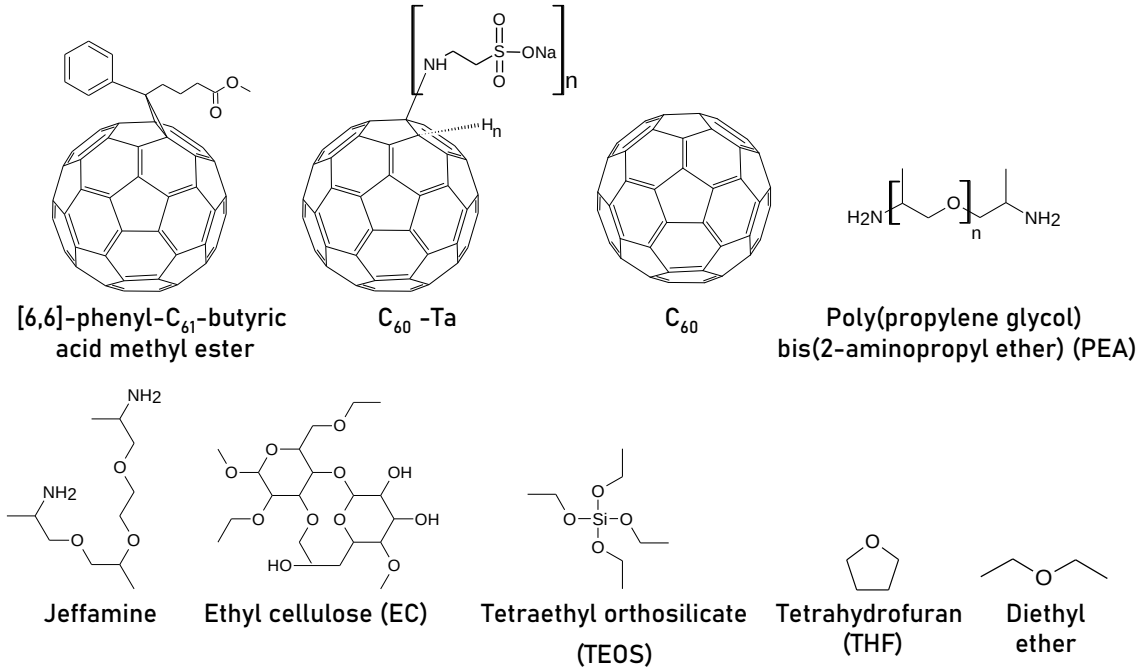

Figure A0. 7 Chemical structures of esters and ethers containing additives for $MAPbI_3$ PSC.[58]

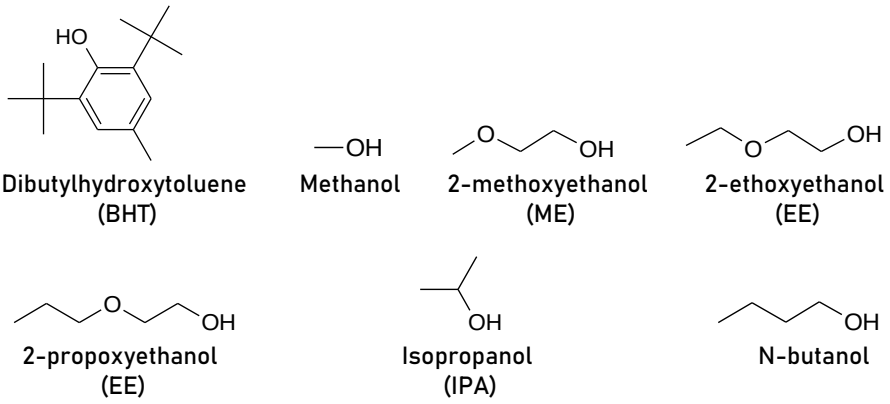

Figure A0. 8 Chemical structures of alcohol additives for $MAPbI_3$ PSC.[58]

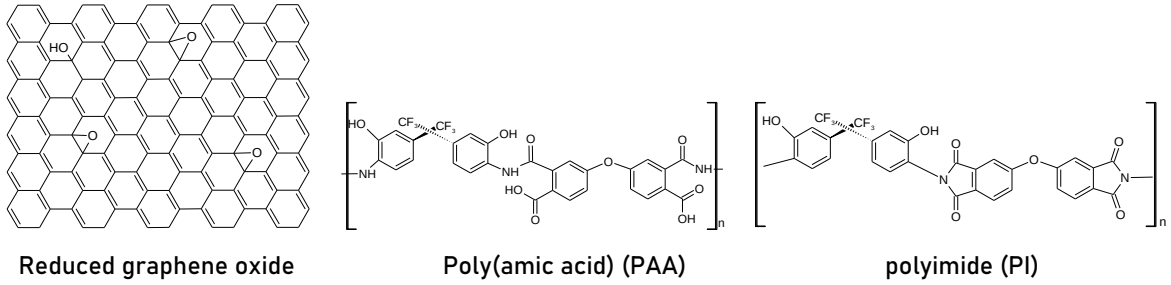

Figure A0. 9 Chemical structures of oxygen-based multifunctional group containing additives.[58]

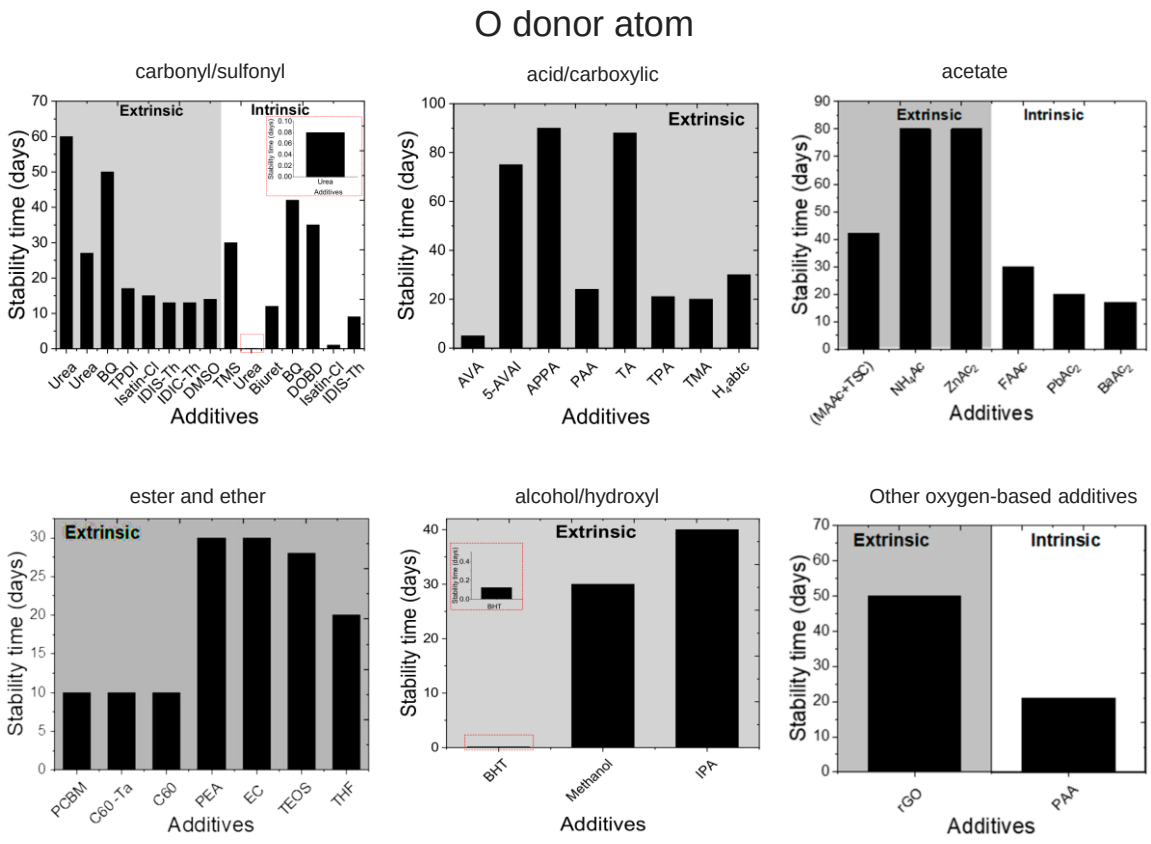

Figure A0. 10 Influence of additives with O donor atom on the photostability of $MAPbI_3$ photoactive layer. Here extrinsic represents ambient test conditions while intrinsic represent inert test conditions. The additives were subcategorised based on relevant functional groups as carbonyl/sulfonyl, acids, acetates, ester and ether and alcohol and other multifunctional groups.[58]

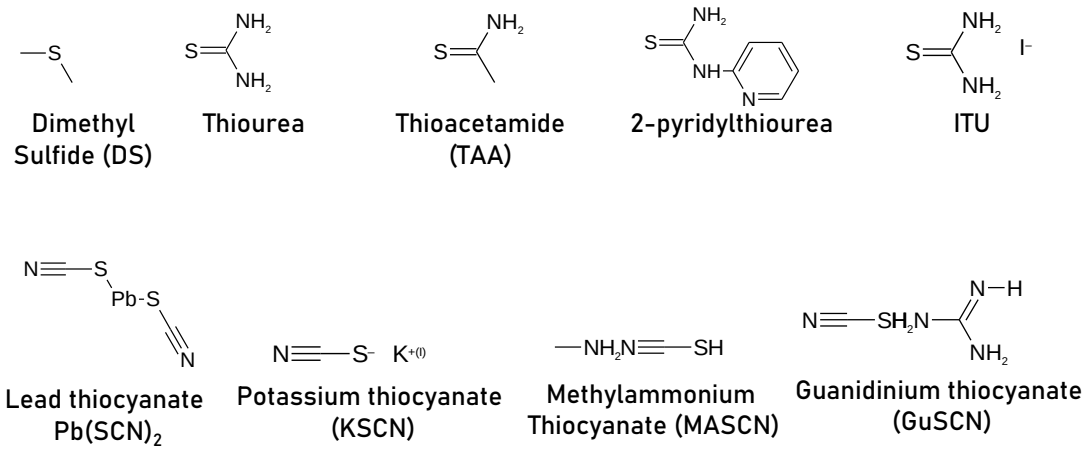

Figure A0. 11 Chemical structures of organosulphur additives for $MAPbI_3$ PSC.[58]

S donor atom

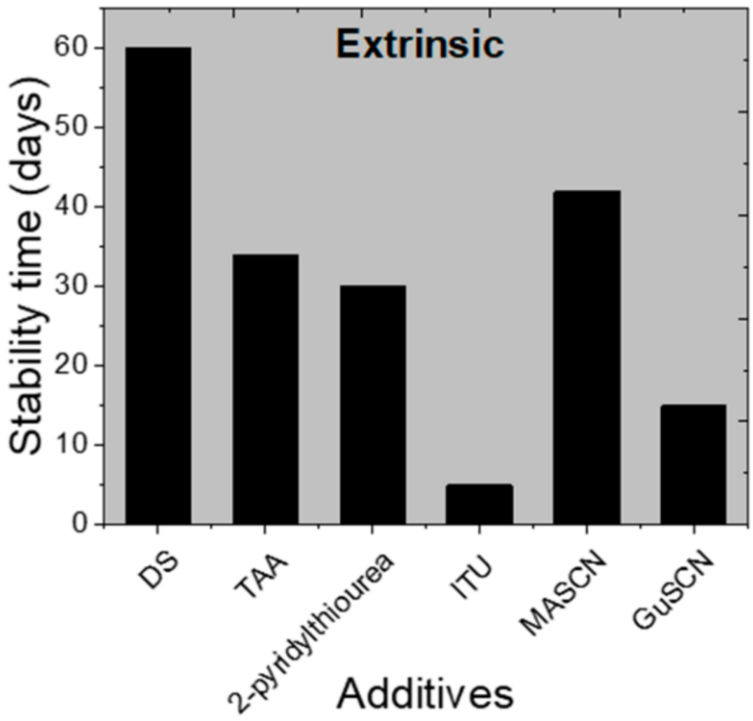

Figure A0. 12 Influence of additives with S donor atom onto the photostability of $MAPbI_3$ active layer.[58]

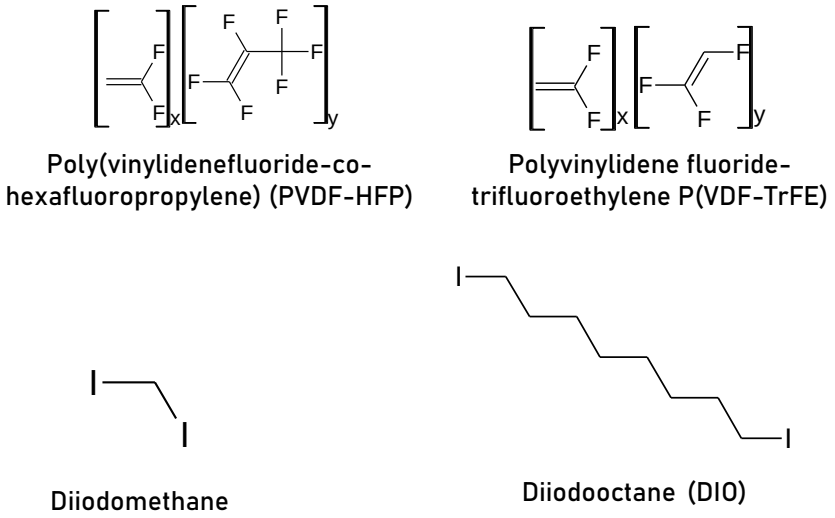

Figure A0. 13 Chemical structures of alkane based additives for $MAPbI_3$ PSC.[58]

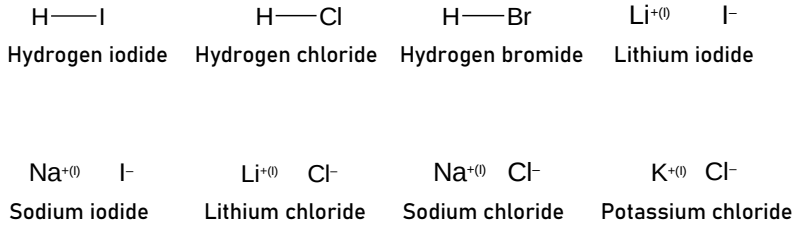

Figure A0. 14 Chemical structures of alkali metal additives for $MAPbI_3$ PSC.[58]

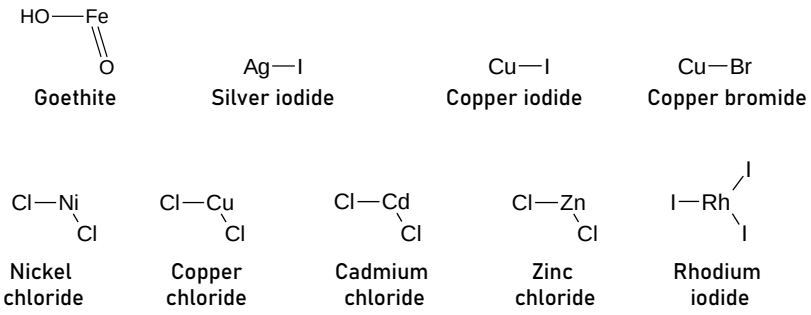

Figure A0. 15 Chemical structures of transition metal additives for $MAPbI_3$ PSC.[58]

Figure A0. 16 Chemical structures of other metal additives in $MAPbI_3$ PSC.[58]

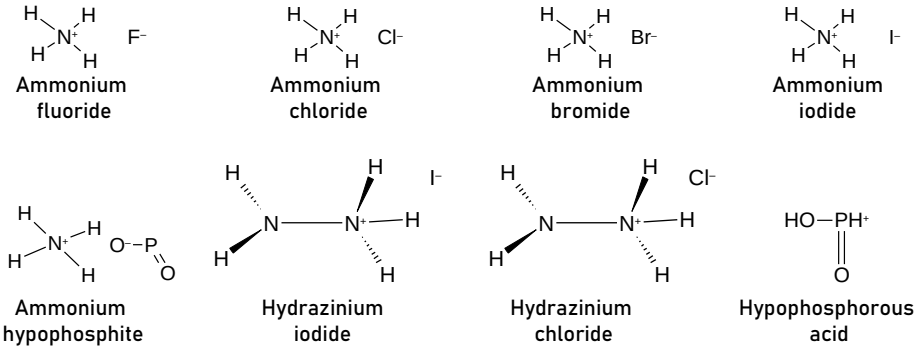

Figure A0. 17 Chemical structure of non-metal halide additives for $MAPbI_3$ PSC.[58]

.

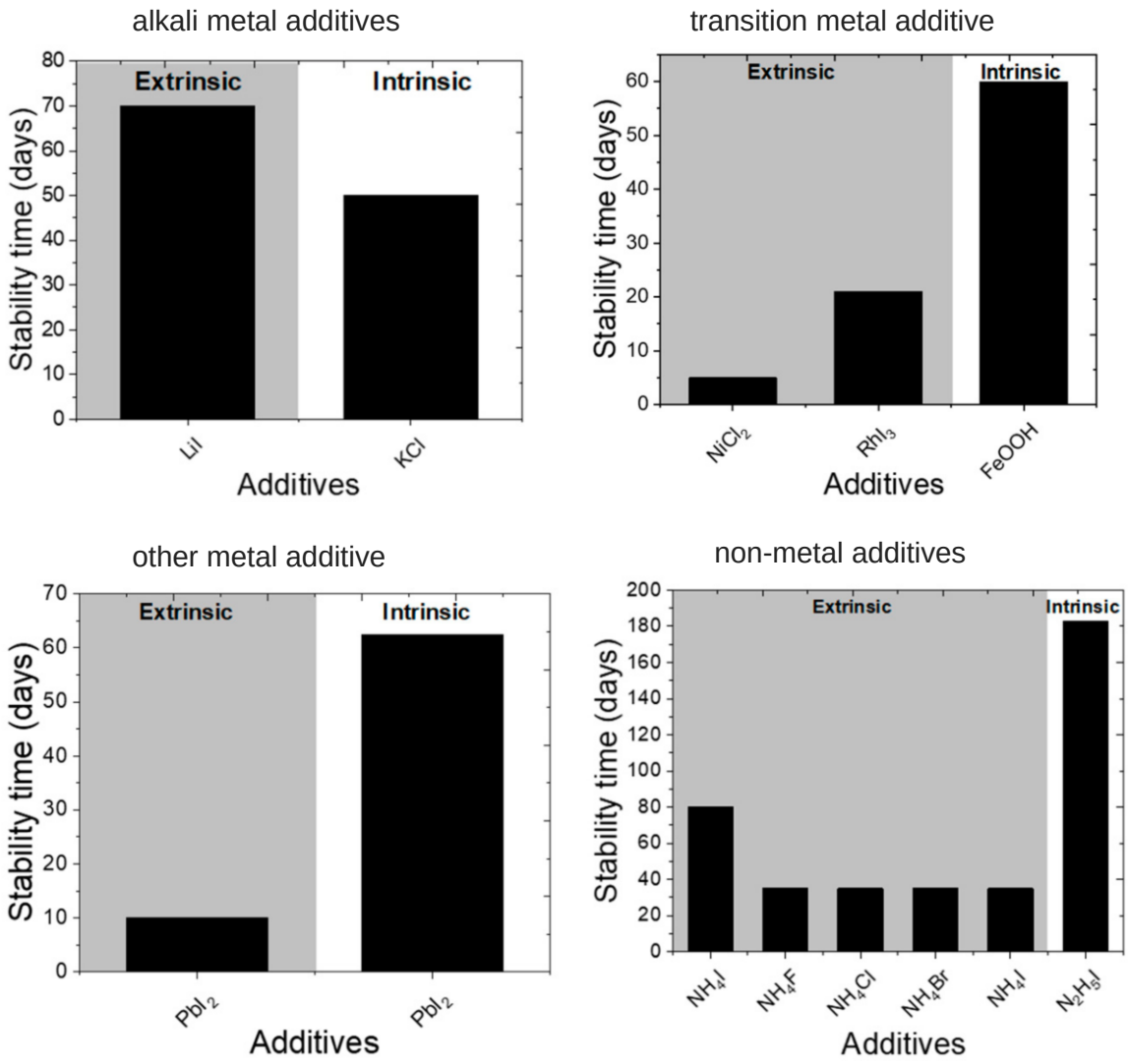

Figure A0. 18 Comparison of the influence of inorganic additives belonging to alkali metal salts, transition metal halides, other metal additives and non-metal additives onto photostability of $MAPbI_3$ photoactive layer for PSC.[58]

Appendix 1: UV-Vis Evolution of Investigated Additives

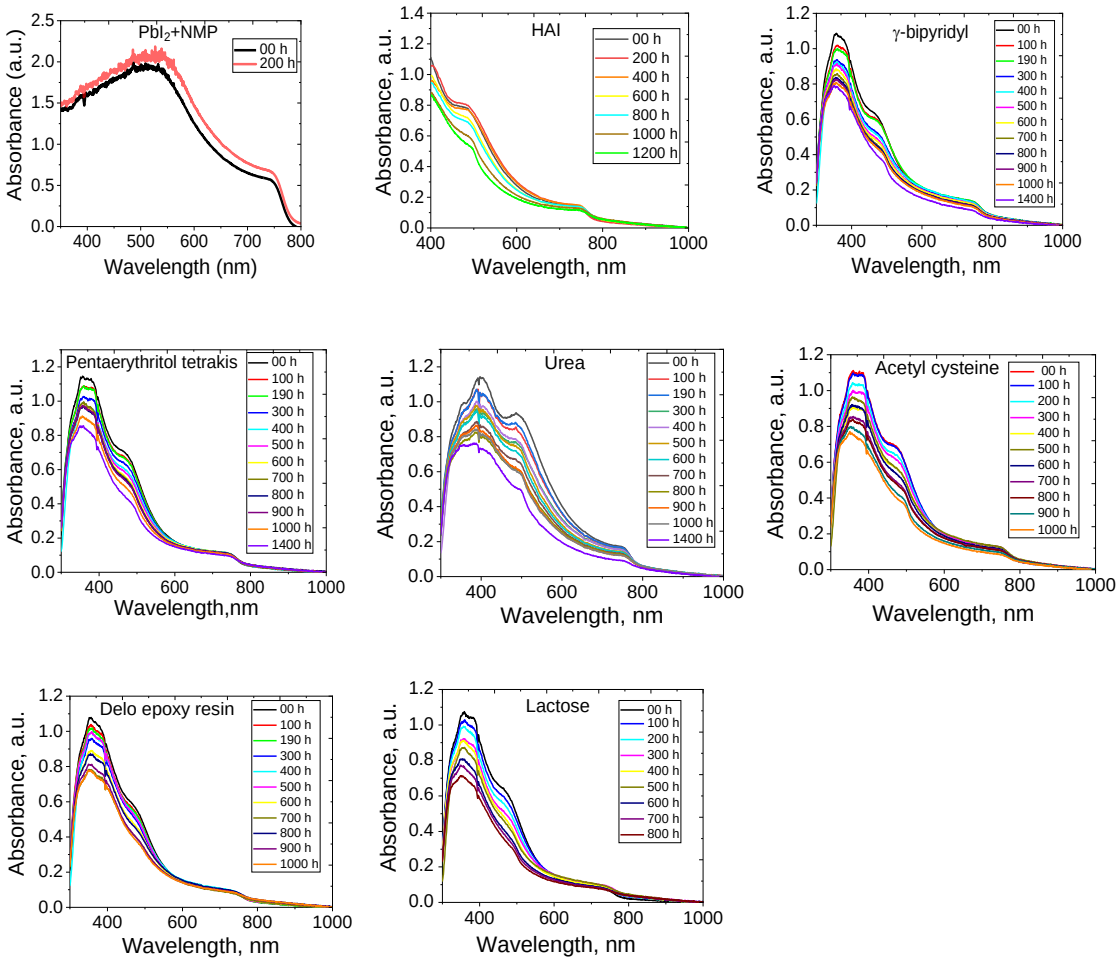

Figure A1. 1 UV-Vis evolution of additives showing stabilization effect in $MAPbI_3$ films against illumination in the inert environment

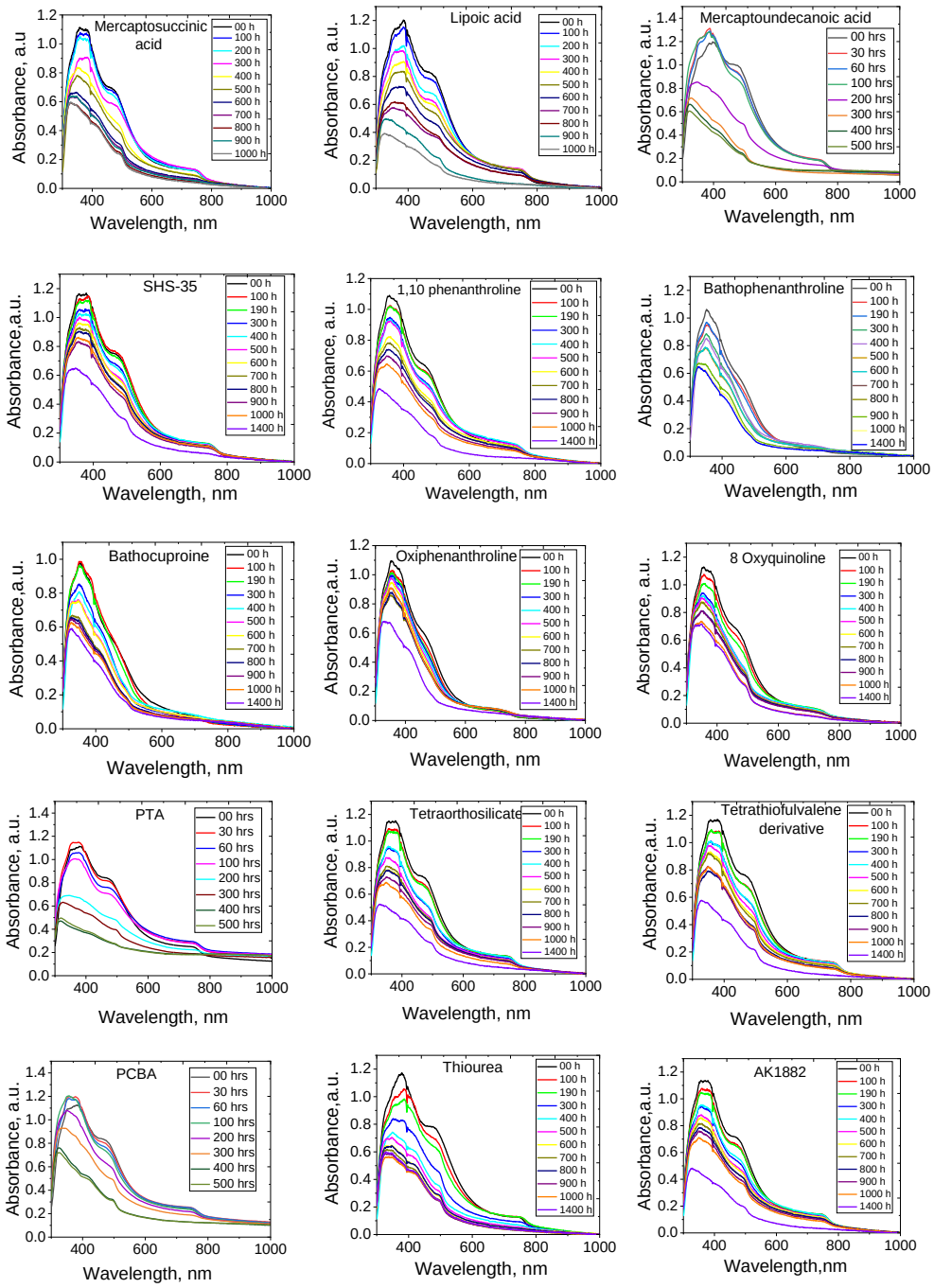

Figure A1. 2 UV-Vis evolution of investigated additives that did not improve intrinsic photostability of $MAPbI_3$ thin films

Appendix 2: Supplementary Material

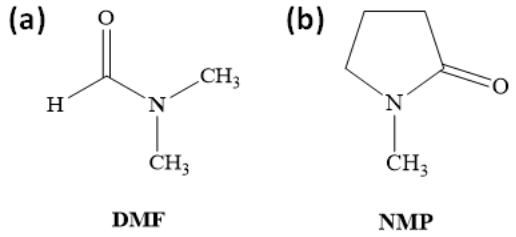

Figure A2. 1 Comparision of Chemical structure of solvents (a) DMF (b) NMP

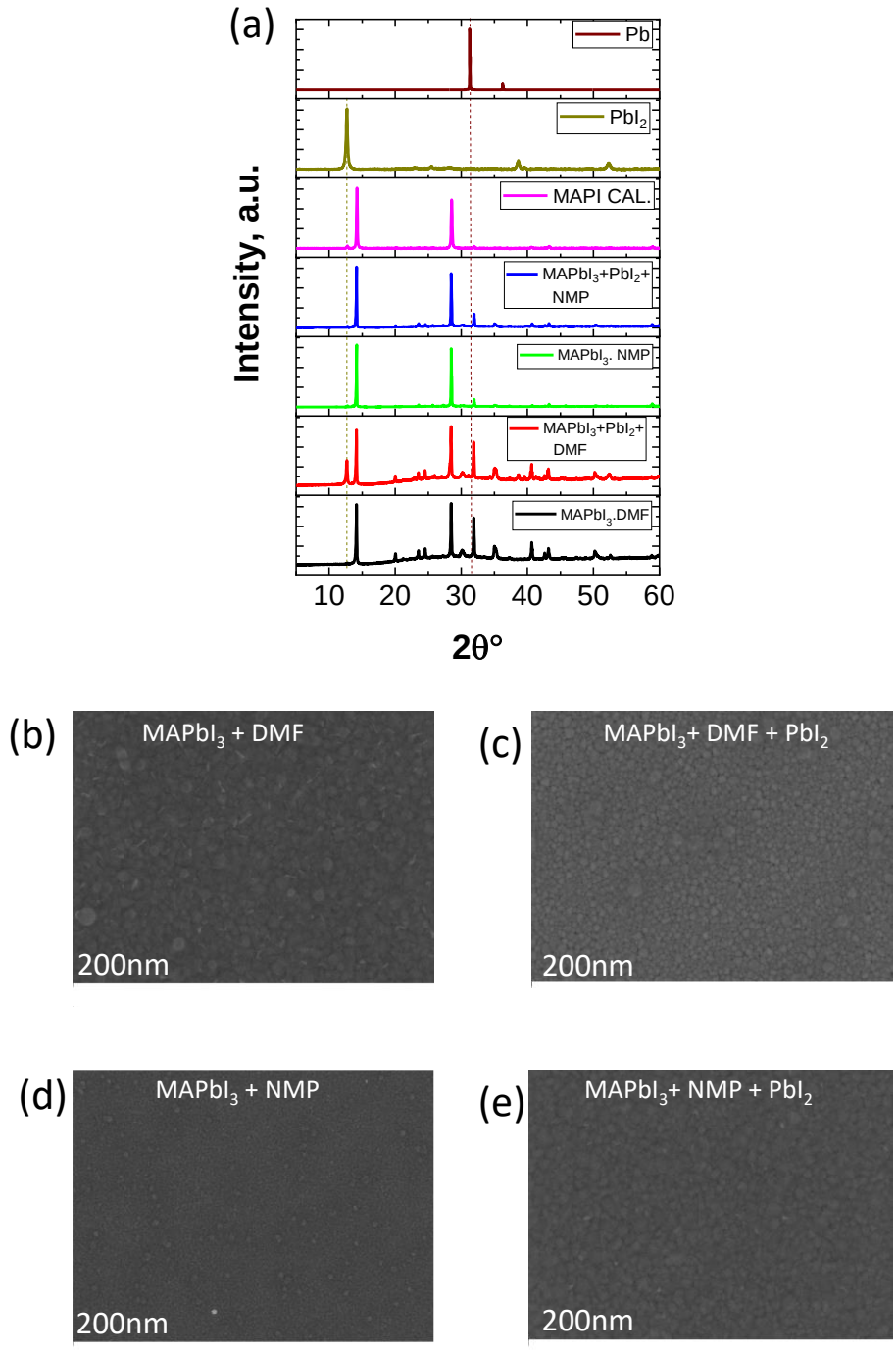

Figure A2. 2 (a) XRD patterns of fresh films. (b-e) SEM images of fresh films.

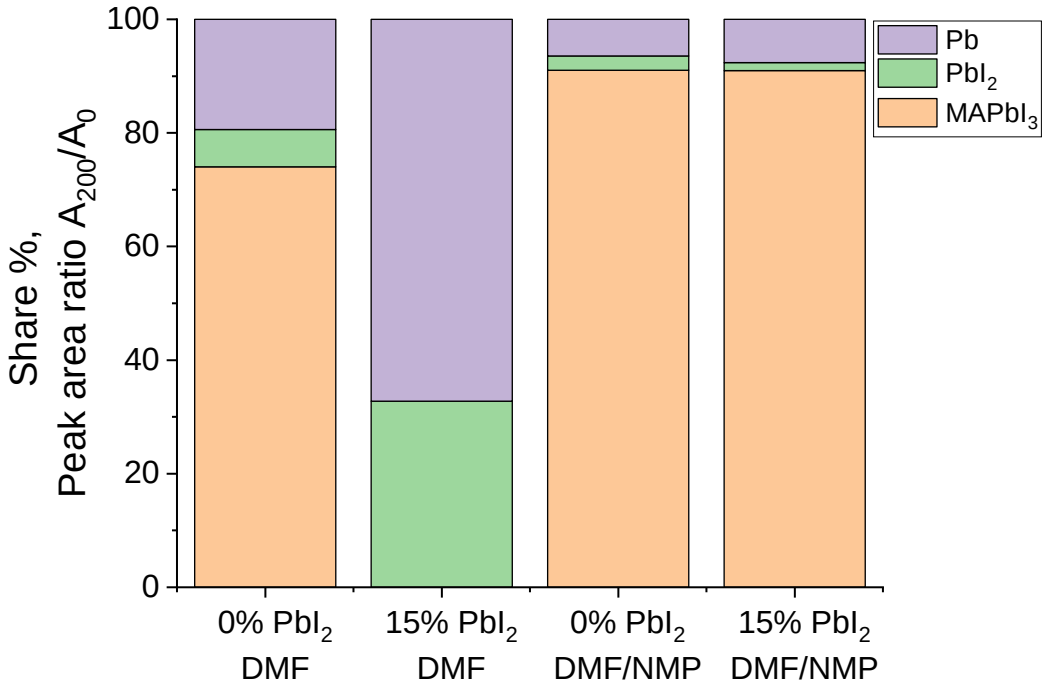

Figure A2. 3 Qualitative analysis of XRD patterns of photoaged $MAPbI_3$ films

Movie 1_DMF pristine.avi (Command Line)

Movie 2_ Excess PbI2 DMF.avi (Command Line)

Movie 3_NMP-DMF pristine.avi (Command Line)

Movie 4_Excess PbI2 NMP-DMF.avi (Command Line)

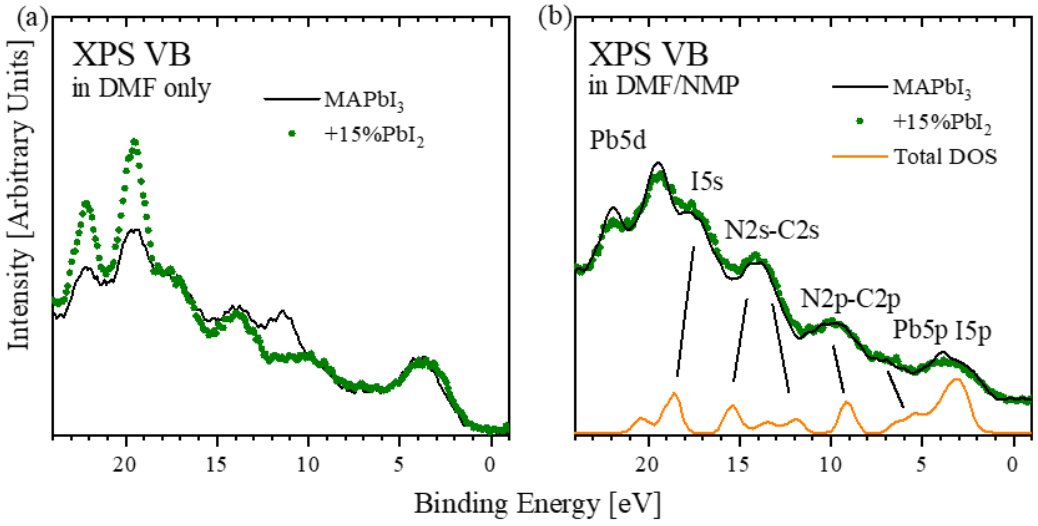

Figure A2. 4 XPS valence band spectra of $MAPbI_3$ thin film with excess of PbI2 (a) from pure DMF (b) from mixture of DMF/NMP.

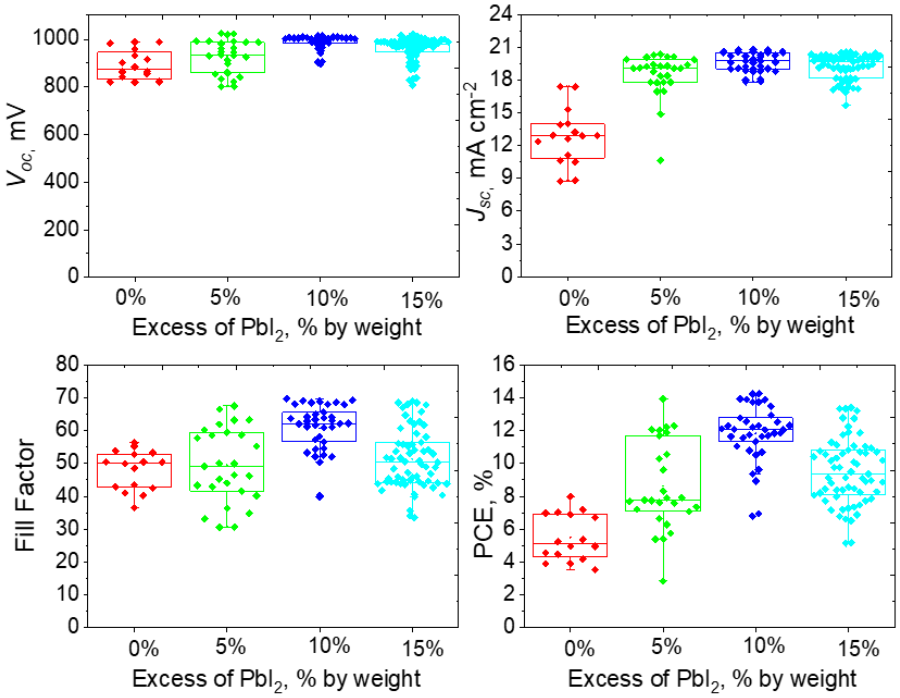

Figure A2. 5 Device performance with overstoichiometric PbI_2 prepared from DMF/NMP cosolvent.

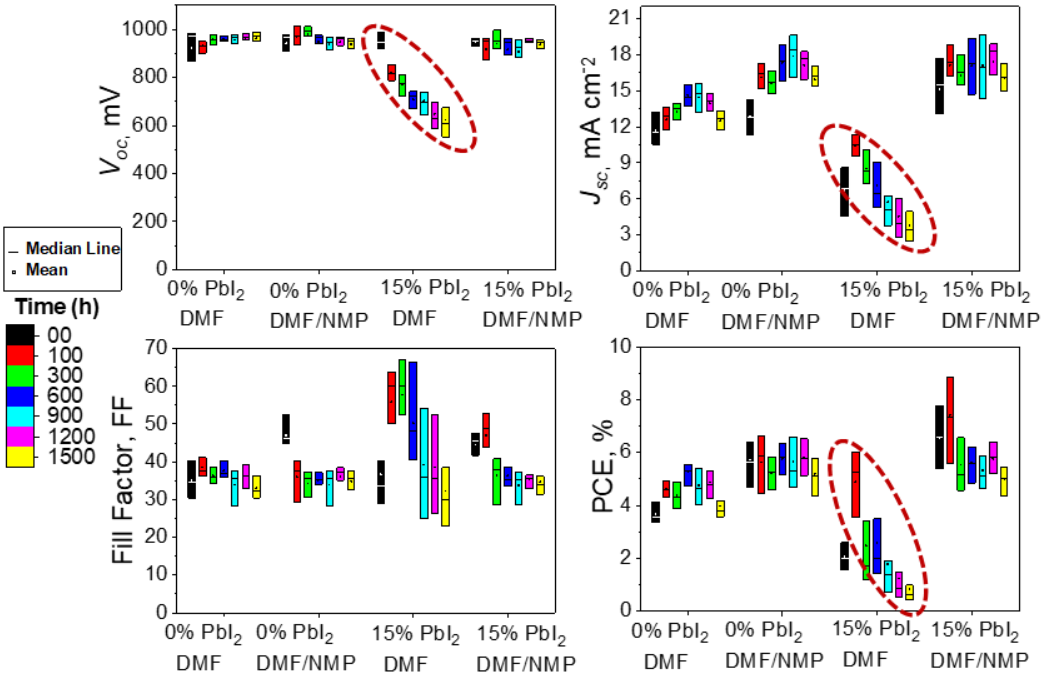

Figure A2. 6 Operational stability of solar cells under continuous illumination. Stability of solar cells made of $MAPbI_3$ with 0% and 15% excess PbI_2, coated from pure DMF and DMF /NMP mixture.

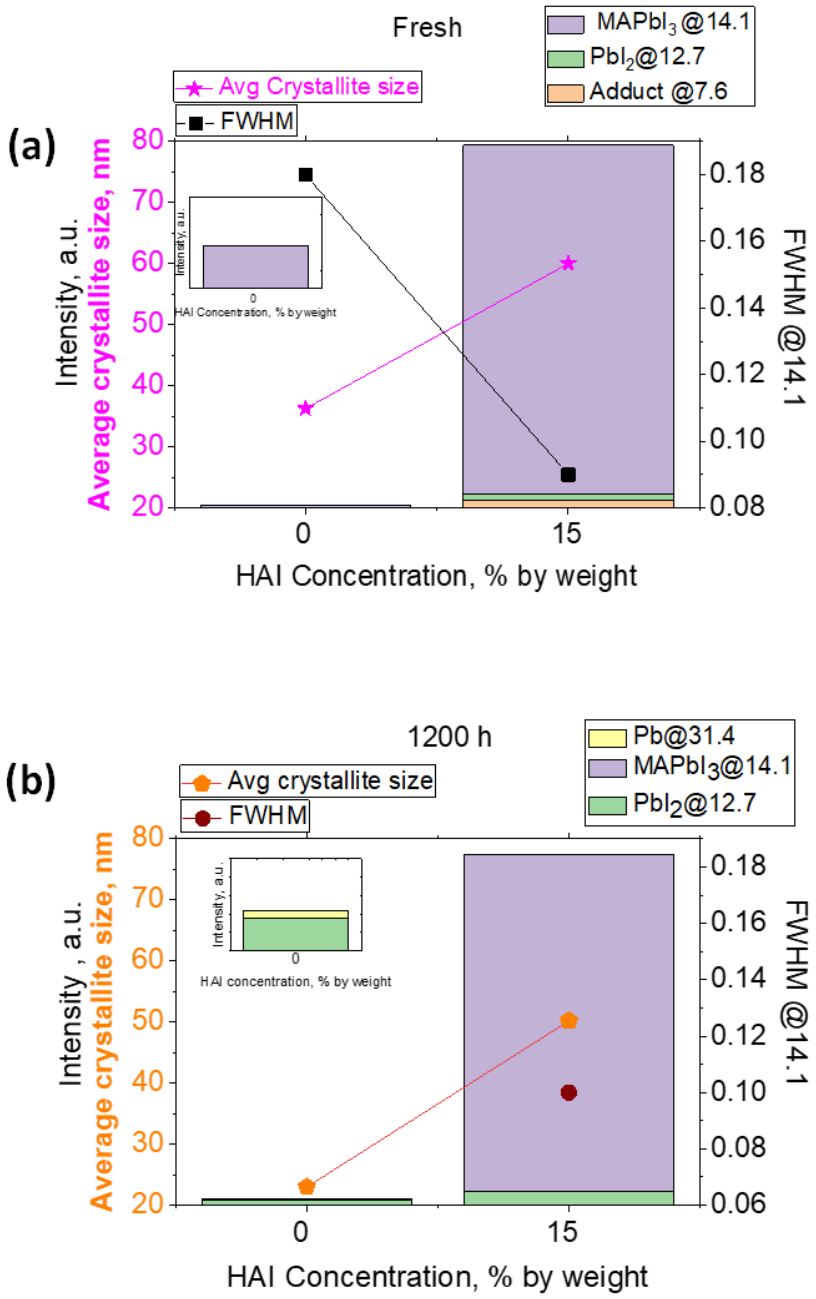

Figure A2. 7 Diffraction intensity of XRD pattern vs FWHM Vs average crystallite size in thin films with 0% & 15% HAI concentration. (a) for fresh films. (b) for photoaged films.[180]

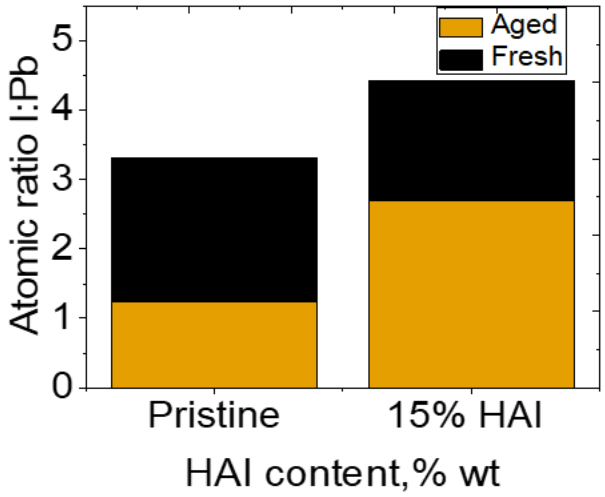

Figure A2. 8 Atomic ratio of I: Pb for the film with and without hydrazinium iodide, before and after photoaging. [180]

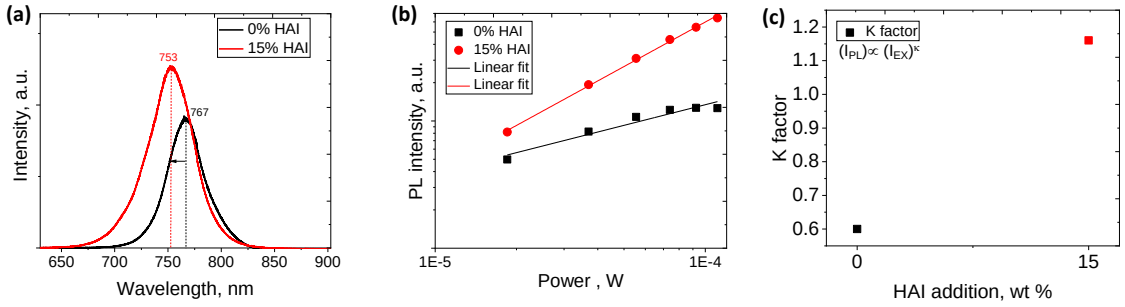

Figure A2. 9 (a) PL spectra of the $MAPbI_3$ films without (0% HAI)/pristine and 15% HAI. (b) Power dependent PL excitation spectra of $MAPbI_3$ films with 0% HAI and 15 % HAI addition. (c) K factor of $MAPbI_3$ films without and with HAI. [180]

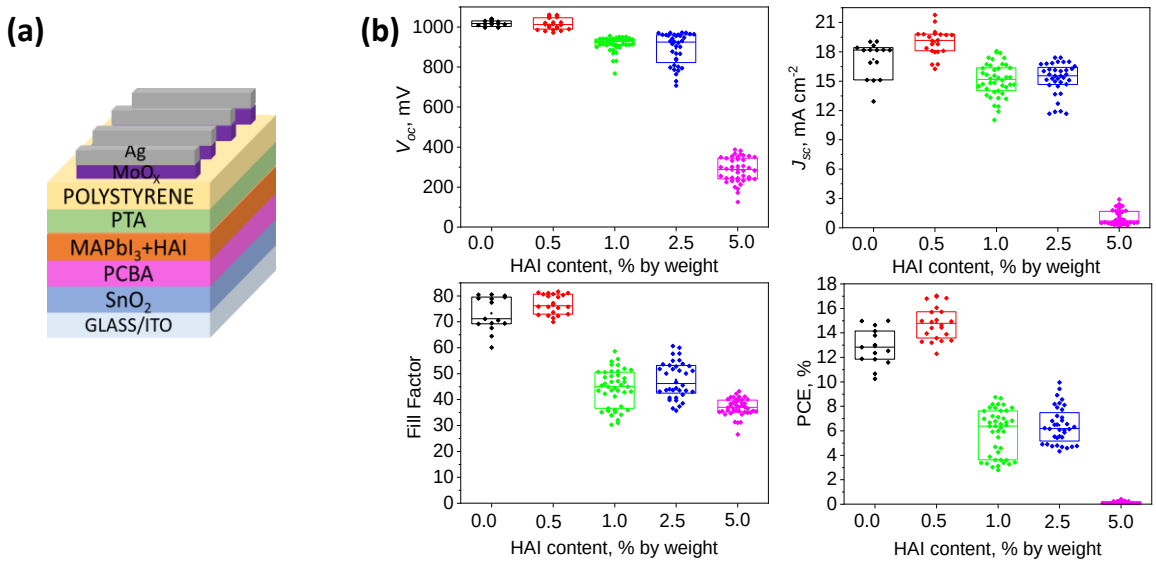

Figure A2. 10 (a) Device architecture of investigated solar cells. (b)Device performance of $MAPbI_3$ solar cells with respect to HAI concentration. [180]

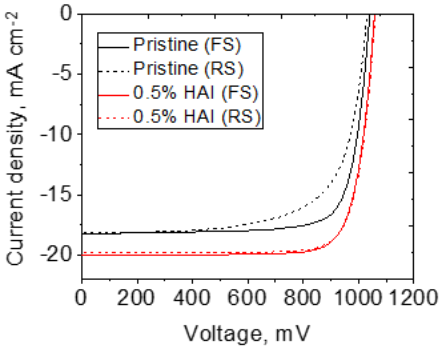

Figure A2. 11 J-V curve of best solar cells with and 0.5% HAI content [180]**.**

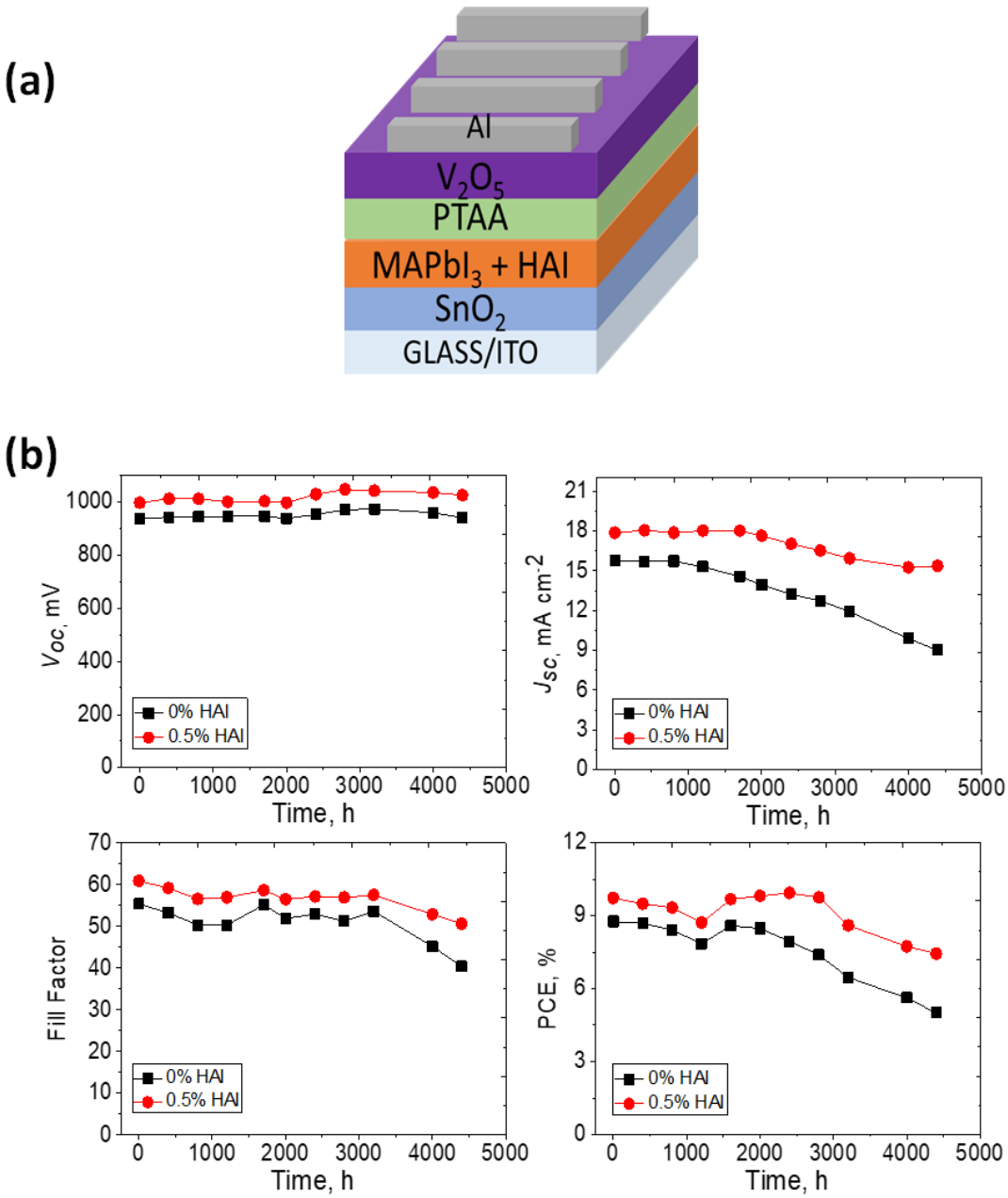

Figure A2. 12 : (a) Device architecture to check HAI impact on operational-stability of solar cell devices. (b) Device performance during operational stability test of MAPbI3 solar cells with optimum HAI Addition [180].

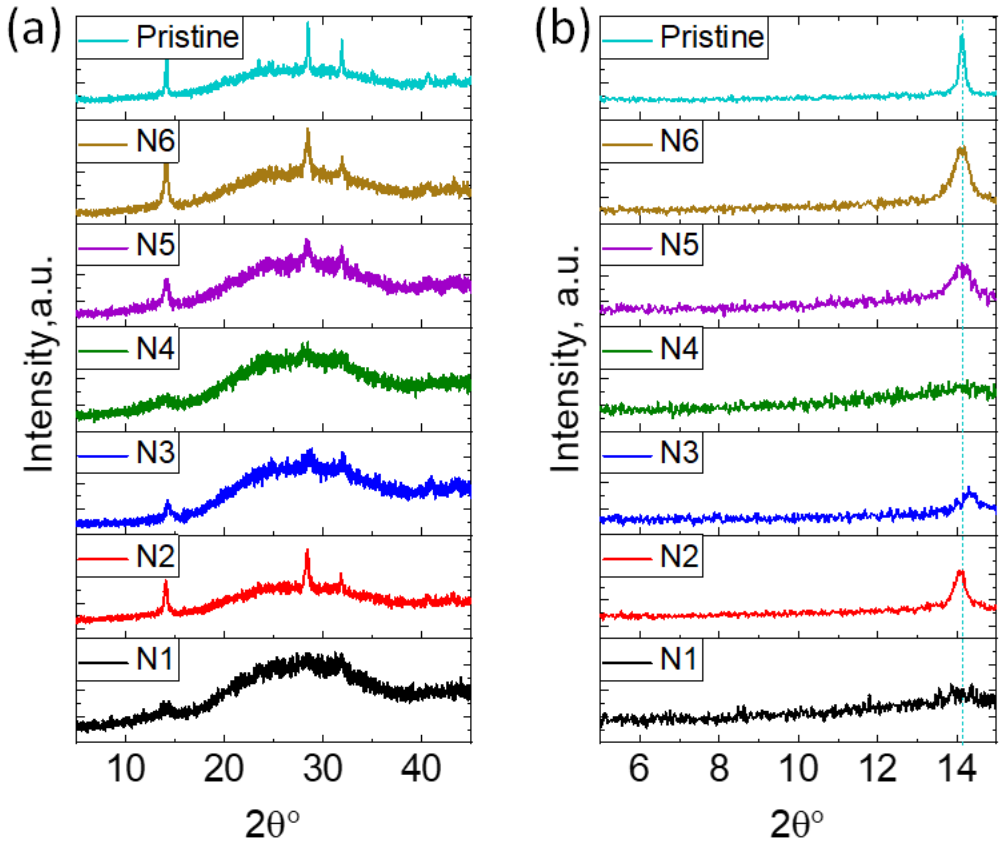

Figure A2. 13 (a) XRD patterns of $MAPbI_3$ films with additives (N1-N6). (b) Zoomed XRD patterns from 5˚ to 15˚

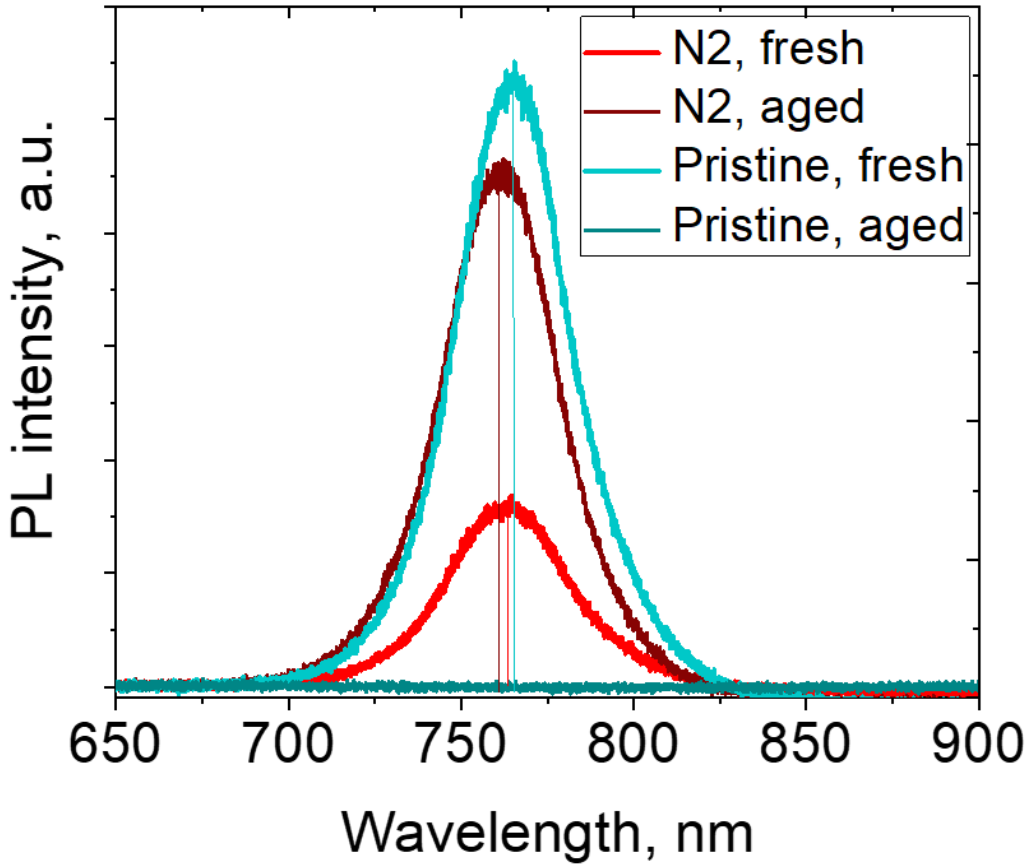

Figure A2. 14 PL emission spectra of fresh and photoaged film with and without N2 additive in $MAPbI_3$

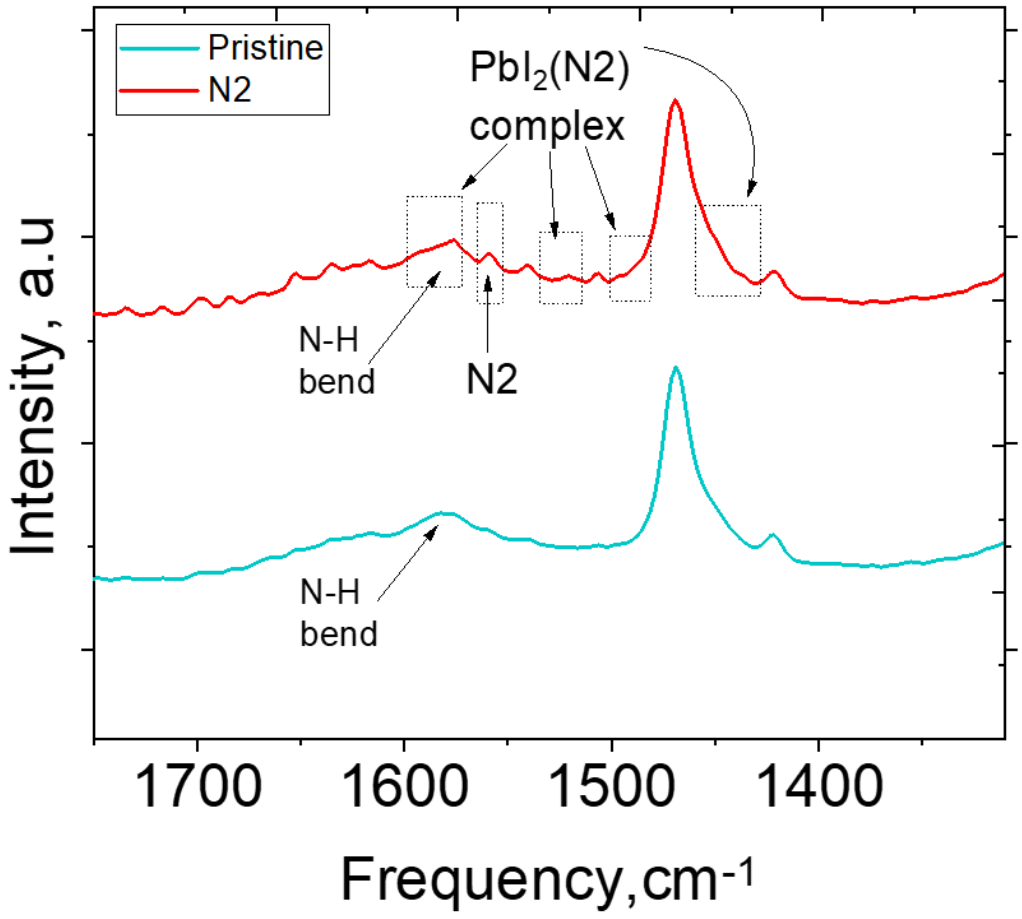

Figure A2. 15 Zoomed FTIR spectra showing complex formation upon N2 addition in fresh film.

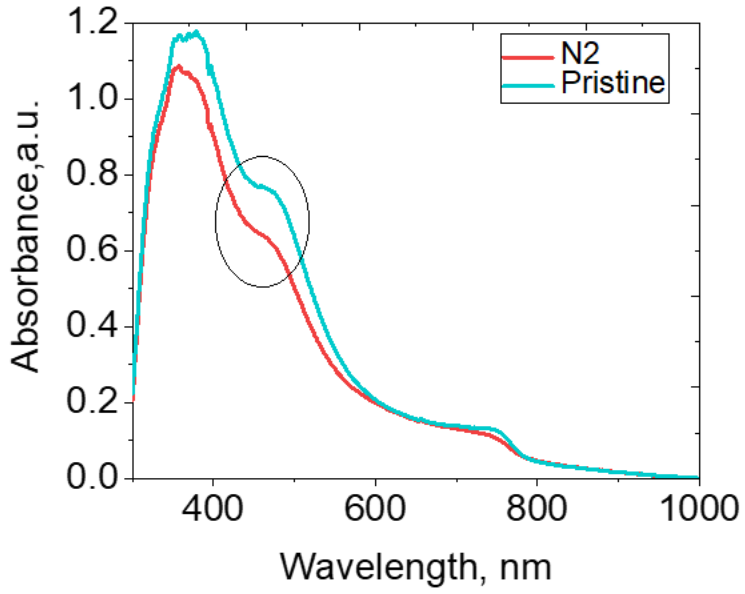

Figure A2. 16 Reduction and shift in absorbance edge near 500 nm upon addition of N2 in $MAPbI_3$

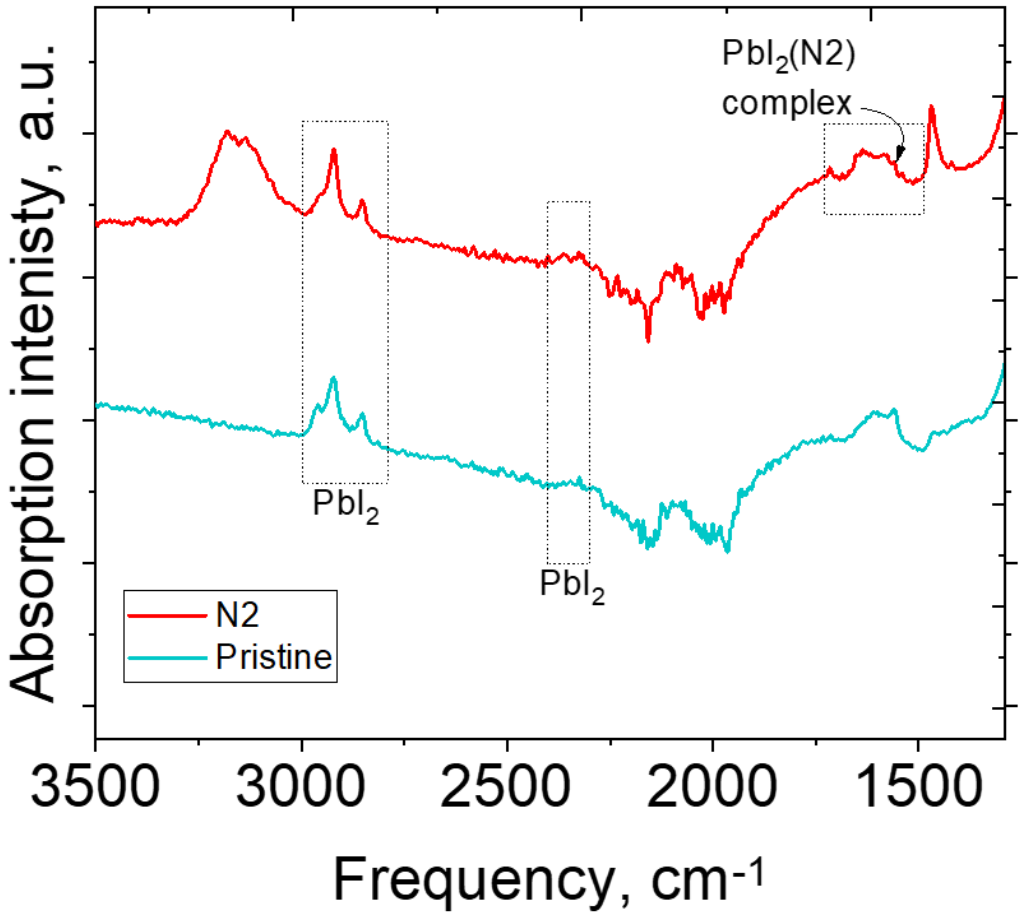

Figure A2. 17 FTIR spectra of photoaged film of pristine $MAPbI_3$ and $MAPbI_3$+N2

Table A 1 IV parameters of $MAPbI_3$+N2, (with respect to concentration)

Concentration		V_{oc}, mV	J_{sc}, mA cm^{-2}	Fill factor	PCE, %
0%	**Best**	**981.84**	**21.13**	**81.52**	**16.91**
	Avg	953.40±13.73	20.20±0.84	76.87±3.78	14.8±1.09
0.5%	**Best**	934.08	20.56	76.62	14.72
	Avg	923.32±7.57	19.23±1.10	70.17±6.32	12.45±1.24
1%	**Best**	936.70	20.53	76.53	14.72
	Avg	923.89±10.71	18.98±1.79	68.64±7.70	12.00±1.53
2.5%	**Best**	**954.34**	**20.83**	**77.94**	**15.49**
	Avg	940.85±10.63	19.54±1.34	71.98±6.79	13.22±1.45
5%	**Best**	962.52	15.4	63.40	9.39
	Avg	916.04±26.49	14±0.75	56.02±3.85	7.20±0.85
7.5%	**Best**	862.17	7.16	57.52	3.55
	Avg	802.14±54.38	6.42±0.96	53.71±4.55	2.78±0.57

Table A 2 J-V characteristics and hysteresis factor of best solar cells made of pristine vs 2.5% $MAPbI_3$+N2

concentration	V_{oc}, mV	J_{sc}, mA cm^{-2}	Fill factor	PCE, %	Hysteresis factor (HF)
0.0% (FS)	981.84	21.13	81.52	16.91	**0.1574**
0.0% (RS)	946.81	20.43	75.78	14.61	
2.5% (FS)	954.34	20.83	77.94	15.49	**0.1568**
2.5% (RS)	953.36	20.46	68.60	13.39	